Plasma Physics Reports, Vol. 29, No. 4, 2003, pp. 279–289. Translated from Fizika Plazmy, Vol. 29, No. 4, 2003, pp. 307–317.

MAGNETIC CONFINEMENT SYSTEMS

Relaxation of Plasma Rotation in Toroidal Magnetic Confinement Systems

L. M. Kovrizhnykh

Institute of General Physics, Russian Academy of Sciences, ul. Vavilova 38, Moscow, 117942 Russia

Received September 26, 2002

Abstract—A study is made of the relaxation of plasma rotation in nonaxisymmetric toroidal magnetic confinement systems, such as stellarators and rippled tokamaks. In this way, a solution to the drift kinetic equation is obtained that explicitly takes into account the time dependence of the distribution function, and expressions for the diffusive particle fluxes and longitudinal viscosity are derived that make it possible to write a closed set of equations describing the time evolution of the ambipolar electric field E and the longitudinal (with respect to the magnetic field) plasma velocity U_0. Solutions found to the set of evolutionary equations imply that the relaxation of these two parameters to their steady-state values occurs in the form of damped oscillations whose frequency is about $2v_T/R$ (where v_T is the ion thermal velocity and R is the major plasma radius) and whose damping rate depends on the ion–ion collision frequency and on the magnetic field parameters. In particular, it is shown that, for tokamaks with a slightly rippled longitudinal magnetic field, the frequency of oscillations in the range $q > 2$ (where q is the safety factor) is, as a rule, much higher than the damping rate. For stellarators, this turns out to be true only of the central plasma region, where the helical ripple amplitude ε of the magnetic field is much smaller than the toroidal ripple amplitude $\delta = r/R$. *© 2003 MAIK "Nauka/Interperiodica".*

1. INTRODUCTION

The problem of how the rotation of a plasma in toroidal magnetic confinement systems influences its confinement properties has been widely discussed in the literature and is still attracting attention of both experimenters and theoreticians. It is well known that poloidal and toroidal plasma rotation is associated with the ambipolar electric field E and the magnetic field–aligned motion of a plasma as a whole with the velocity U. Together with the density and temperature gradients and the magnetic field strength, the ambipolar field and the velocity of this motion determine the particle and heat fluxes across the magnetic field. Also, the electric field may have a stabilizing effect on plasma fluctuations, thereby reducing the losses associated with them.

A self-consistent set of equations describing the time evolution of the plasma parameters and their steady-state (or, in the absence of external sources, quasi-steady-state) values, including the ambipolar electric field and longitudinal plasma velocity, were derived in my paper [1], in which it was shown, in particular, that the longitudinal viscosity is expressed through the partial diffusive fluxes associated with the magnetic field nonuniformity by two independent angular variables (e.g., by the toroidal and poloidal azimuthal angles). In my subsequent paper [2], these fluxes were evaluated explicitly for a rippled tokamak and a toroidal stellarator (with one helical field harmonic) and an attempt was made to follow the time evolution of the ambipolar electric field and longitudinal plasma velocity and to determine their quasi-steady-state values. It was found that, if the characteristic relaxation time of the longitudinal velocity is sufficiently long and exceeds the ion mean free time $\tau_i = \nu_i^{-1}$ (where ν_i is the effective ion–ion collision frequency), then the characteristic time scale on which the electric field changes is much shorter than the inverse ion–ion collision frequency. However, in [2], the diffusive flux and longitudinal viscosity were calculated in the usual way, by solving the kinetic equation that was obtained for a *steady-state* case, i.e., by neglecting the time derivative of the distribution function. This approach is clearly justified when all of the quantities in the equation (in particular, the field E and velocity U) change only slightly during time τ_i. Consequently, although the equations derived in [2] provide correct values of the quasi-steady-state electric field and correct time evolution of the longitudinal velocity on long time scales ($t \gg \tau_i$), they fail to describe the evolution of these parameters during the initial stage $t < \tau_i$. In order to obtain equations capable of correctly describing the initial evolutionary stage in which the electric field and longitudinal velocity change rapidly with time (in comparison with the ion–ion collision frequency), it is necessary to use the expressions derived for the diffusive flux and longitudinal viscosity by solving a *time-depen-*

1063-780X/03/2904-0279$24.00 © 2003 MAIK "Nauka/Interperiodica"

dent kinetic equation, i.e., the equation that contains the time derivative of the distribution function.[1]

The objectives of the present paper are to solve the time-dependent kinetic equation; to use the solution obtained to deduce the diffusive fluxes and longitudinal viscosity; and, finally, to solve the set of equations that was derived in [1] for the ambipolar electric field and longitudinal plasma velocity.

It is found that in rippled tokamaks, as well as in stellarators, the electric field relaxes by damped oscillations. Moreover, for a rippled tokamak, the damping rate is, as a rule, much lower than the oscillation frequency. As regards stellarators, this is true only for the central region of the plasma column, whereas, at the plasma edge, where the helical ripple amplitude ε of the magnetic field is larger than or comparable to the toroidal ripple amplitude $\delta = r/R$, the oscillation frequency is on the order of the damping rate or lower; i.e., the relaxation process is nearly aperiodic.

The paper is organized as follows. In Section 2, the basic equations are written out and the formulation of the problem is discussed. In Section 3, the time-dependent kinetic equation is solved and the partial diffusive fluxes are calculated. In Section 4, the resulting set of equations for the electric field and longitudinal velocity is presented and investigated analytically (by deriving and examining a dispersion relation). Finally, Section 5 describes the results of solving these equations numerically.

2. BASIC EQUATIONS AND THE FORMULATION OF THE PROBLEM

As was already mentioned, a self-consistent set of equations describing the time evolution of the ambipolar electric field and longitudinal plasma velocity was derived in [1]. We consider an arbitrary curvilinear coordinate system (x_1, x_2, x_3), where x_1 is a magnetic surface label (e.g., a toroidal or poloidal flux) such that the equation $x_1(\mathbf{r}) = \text{const}$ defines a magnetic surface and the independent angular variables x_2 and x_3 are arbitrary combinations of the toroidal (φ) and poloidal (ϑ) azimuthal angles such that the magnetic field is periodic in x_2 and x_3. In this coordinate system, the self-consistent set of equations has the form [1, 2]

$$\begin{aligned}\overline{\varepsilon_\perp \sqrt{g}\nabla x_1 \cdot \frac{\partial \mathbf{E}}{\partial t}} &= -4\pi \sum e S_{nc},\\ \overline{\frac{m\sqrt{g}}{B}\frac{\partial NU}{\partial t}} &= \sum \frac{e}{c}\overline{\sqrt{g}\left(\frac{B^{(2)}}{B_{(3)}}S_2 - \frac{B^{(3)}}{B_{(2)}}S_3\right)}.\end{aligned} \tag{1}$$

Here, $\varepsilon_\perp = 1 + 4\pi mc^2 NB^{-2} \simeq 4\pi mc^2 NB^{-2}$ is the transverse dielectric constant, which will be assumed to be much larger than unity; m is the mass of an ion; c is the speed of light; N is the particle density; e is the charge of an electron or an ion; $B(x_1, x_2, x_3)$ is the magnetic field strength; $g = \|g_{ik}\|$ is the determinant of the metric tensor ($\sqrt{g} = (\nabla x_1 \cdot [\nabla x_2 \times \nabla x_3])^{-1}$); $B^{(k)}$ and $B_{(k)}$ ($k = 1, 2, 3$) are the contravariant and covariant components of the vector $\mathbf{B}$; the overbar denotes averaging over the angular variables x_2 and x_3; and the symbol Σ stands for the summation over electrons and ions. However, to simplify further calculations, we restrict ourselves to considering the case in which the main contribution to the diffusive fluxes (and, accordingly, to the longitudinal viscosity) comes from the ion component and, hence, the summation sign can be omitted. The neoclassical diffusive flux S_{nc} is equal to the sum of the averaged partial fluxes,

$$S_{nc} = \overline{S_2} + \overline{S_3}, \tag{2}$$

each of which is associated with the magnetic field nonuniformity in one of the angular variables:

$$\begin{aligned}S_2 &= \frac{B_{(3)}}{\omega_B}\int d\mathbf{v} F u \frac{\partial}{\partial x_2}\frac{u}{B},\\ S_3 &= -\frac{B_{(2)}}{\omega_B}\int d\mathbf{v} F u \frac{\partial}{\partial x_3}\frac{u}{B}.\end{aligned} \tag{3}$$

Here, we use conventional notation: $u = \sigma(2\mathscr{E} - 2e\Phi/m - 2\mu B)^{1/2}$, $\sigma = \text{sgn}(\mathbf{B}\cdot\mathbf{v})/B$, $\mathscr{E}$ and μ are the energy and magnetic moment of a particle per unit mass, $\omega_B = eB/mc$, the ambipolar potential $\Phi(x_1, t)$ is assumed to be constant at a magnetic surface and to depend explicitly on time, $d\mathbf{v}$ is the volume element in velocity space, and $F(x_1, x_2, x_3, \mathscr{E}, \mu, t)$ is the distribution function.

Our purpose is to evaluate the fluxes S_2 and S_3 and to solve Eqs. (1) in the case when the characteristic time scale on which the ambipolar potential varies is shorter than the ion mean free time $\tau_i = \nu_i^{-1}$. To do this, we as usual neglect the weak time dependence of the density and temperature. In this way, we need to solve the kinetic equation, which has the following form in terms of the variables t, x_k, $\mathscr{E}$, and μ:

$$\begin{aligned}&\frac{\partial F}{\partial t} + \frac{e}{m}\frac{\partial \Phi}{\partial t}\frac{\partial F}{\partial \mathscr{E}} + \frac{B^{(2)}}{B}u\frac{\partial F}{\partial x_2} + \frac{B^{(3)}}{B}u\frac{\partial F}{\partial x_3}\\ &= -\frac{uB_3}{\omega_B\sqrt{g}}\frac{\partial F_0}{\partial x_1}\frac{\partial}{\partial x_2}\frac{u}{B} + \frac{uB_2}{\omega_B\sqrt{g}}\frac{\partial F_0}{\partial x_1}\frac{\partial}{\partial x_3}\frac{u}{B} + \text{St}.\end{aligned} \tag{4}$$

Here, the distribution function $F_0(x_1, \mathscr{E}, t)$ in the zeroth approximation is assumed to be Maxwellian,

$$F_0 = F_M = N(2\pi v_T^2)^{-3/2}\exp\left(-\frac{\mathscr{E} - e\Phi/m}{v_T^2}\right); \tag{5}$$

$v_T = (T/m)^{1/2}$ is the ion thermal velocity; and St is the ion–ion collision integral.

[1] Note that the general equations obtained in [1] are valid for arbitrary time scales because they were derived without making any assumptions about the form of the distribution function.

In what follows, we will be interested primarily in the initial evolutionary stage during which the characteristic frequency (the damping rate) of the ambipolar field and, accordingly, of the distribution function is much higher than the ion–ion collision frequency, i.e., when $\partial F/\partial t \gg \mathrm{St}$. For time scales on which this inequality is satisfied, collisions can be neglected. For time scales long enough for the electric field to relax to nearly the quasi-steady-state value and depend on time only through the longitudinal velocity (this indicates that the opposite inequality $\partial F/\partial t \ll \mathrm{St}$ is satisfied), the expressions for the fluxes S_2 and S_3 and the equations for E and U can be derived by solving the time-independent kinetic equation, as was done in [2].

In the intermediate case in which the time derivative is on the order of the collision integral, the kinetic equation with the collision integral written in differential form cannot be solved analytically. However, an analytic solution can be obtained by using the following simplest model expression for the collision integral:

$$\mathrm{St} = -\nu_i\left\{F - F_M - \frac{uU}{v_T^2}F_M\right\}. \tag{6}$$

Here, $U = U_0 B/B_0$ is the velocity of the plasma moving as a single entity along the magnetic field, $B_0 = \bar{B}$, and $U_0(x_1)$ is independent of the angular variables x_2 and x_3 (i.e., $\nabla \cdot (U\mathbf{B}/B) = 0$).

Taking into account the aforesaid and without pretending to give a rigorous quantitative description of the electric field evolution on time scales on which $\partial F/\partial t \approx \mathrm{St}$, we will describe collisions by collision integral (6). It should be noted, however, that, for the range of collision frequencies corresponding to the plateau regime, model representation (6) provides correct expressions for the particle flux and longitudinal viscosity and, consequently, makes it possible to correctly describe the evolution of $E(t)$ and $U_0(t)$ on arbitrary time scales t (see also Section 4).

We restrict our further discussion to two simplest cases: a rippled tokamak in which the cross sections of the magnetic surfaces are concentric circles and a toroidal current-free stellarator with one helical field harmonic and a large aspect ratio. Such tokamak and stellarator configurations can be described in conventional quasitoroidal coordinates (r, ϑ, φ), where r is the running minor radius and ϑ and φ are the poloidal and toroidal azimuthal angles. Neglecting small corrections on the order of the product of δ and ε, we can represent the magnetic field in the form

$$\mathbf{B} = \mathbf{B}_T + \mathbf{B}_{\mathrm{St}},\ \ \mathbf{B}_T = \frac{R_0}{R}B_0(\Theta_J\mathbf{e}_\vartheta + \mathbf{e}_\varphi),\ \ \mathbf{B}_{\mathrm{St}} = \nabla\Phi_M,$$

$$\begin{gathered}\Phi_M = -\frac{R_0}{M}B_0\varepsilon(\rho)\sin(M\varphi - n\vartheta),\\ R = R_0(1 + \delta\cos\vartheta),\\ \delta = \frac{r}{R_0},\quad \rho = \frac{Mr}{R_0},\quad \varepsilon(\rho) = \varepsilon_0 I_n(\rho),\end{gathered} \tag{7}$$

where R_0 is the major radius of the torus, $I_n(\rho)$ is the nth-order modified Bessel function, and n and M are integers ($M \gg n$).

Following [2], we choose the variables x_j to be

$$\begin{gathered}x_1 = r\left[\frac{\rho}{2} - \frac{\partial\varepsilon}{\partial\rho}\cos(M\varphi - n\vartheta)\right],\\ x_2 = \vartheta,\quad x_3 = M\varphi - n\vartheta.\end{gathered} \tag{8}$$

We can easily see that, within the adopted accuracy (to first order in ε and δ), the scalar product $\mathbf{B}\cdot\nabla x_1$ equals zero; i.e., the magnetic surfaces are described by the equation $x_1 = \mathrm{const}$. In these coordinates, the contravariant and covariant components of the magnetic field are

$$\begin{gathered}B^{(1)} = 0,\quad B^{(2)} = \frac{B_\vartheta}{r},\quad B^{(3)} = \frac{M}{R}B_\varphi - \frac{n}{r}B_\vartheta = \frac{B_0}{r}\frac{\partial x_1}{\partial r},\\ B_{(1)} = B_r\left(\frac{\partial x_1}{\partial r}\right)^{-1},\\ B_{(2)} = \frac{nR}{M}B_\varphi + rB_\vartheta = \frac{R_0B_0}{M}(n + \delta M\Theta_J),\\ B_{(3)} = \frac{R}{M}B_\varphi - \frac{B_r}{M}\frac{\partial x_1}{\partial\varphi}\left(\frac{\partial x_1}{\partial r}\right)^{-1} = \frac{R}{M}B_\varphi \simeq \frac{R_0B_0}{M},\\ \sqrt{g} = rR_0\left(M\frac{\partial x_1}{\partial r}\right)^{-1} \simeq \frac{R_0^2}{M^2},\\ \frac{\partial x_1}{\partial r} = \rho - \frac{\partial}{\partial\rho}\rho\frac{\partial\varepsilon}{\partial\rho}\cos x_3 \simeq \delta M,\\ B = B_0[1 - b_2(x_1x_2) - b_3(x_1x_3)],\\ b_2 = \delta\cos x_2,\quad b_3 = \varepsilon\cos x_3.\end{gathered} \tag{9}$$

For a rippled tokamak, we must set $n = 0$, and for a current-free stellarator, we must set $\Theta_J = 0$. In the latter case, it is necessary to keep in mind the relationships

$$\begin{gathered}\overline{\left(\frac{B^{(2)}}{B^{(3)}}\right)} = \overline{\left(\frac{dx_2}{dx_3}\right)} = \frac{t}{M - nt}\\ = \frac{1}{q_sM - n} \simeq \frac{1}{q_sM} = \frac{\Theta_s}{\delta M},\end{gathered} \tag{10}$$

where $t = (q_s)^{-1} = \delta^{-1}\Theta_s$ is the average rotational transform in a stellarator and q_s is the safety factor.

With allowance for relationships (9) and (10), Eqs. (1) can be rewritten as

$$N\frac{\partial V_E}{\partial t} = \omega_B\frac{M}{rR_0}(\bar{S}_2 + \bar{S}_3),$$

$$N\frac{\partial U}{\partial t} = \omega_B\frac{M^2}{R_0^2}\left(\frac{\bar{S}_2}{qM-n} - \frac{\bar{S}_3}{n+\delta M\Theta_J}\right) \qquad (11)$$

$$= \Theta N\frac{\partial V_E}{\partial t} - \omega_B\frac{M^2}{R_0^2}\frac{\bar{S}_3}{n+\delta M\Theta_J}.$$

Here, $V_E = -cE/B$ is the drift velocity in an electric field; $E = -|\nabla x_1|\partial\Phi/\partial x_1 \simeq -\partial\Phi/\partial r$ is the ambipolar electric field component normal to the magnetic surface; and $q = \delta/\Theta$, with $\Theta = \Theta_J$ for a tokamak and $\Theta = \Theta_s = \delta t$ for a stellarator.[2]

Before proceeding with a solution to the kinetic equation, we should say a few words about the formulation of the problem.

Let the plasma be in a steady state up to the time $t = 0$, which is assumed to be the initial time in our problem. In the steady state, the ambipolar electric field and longitudinal velocity are equal to their steady-state values, which are determined, in accordance with Eqs. (11), from the condition $\bar{S}_2 = \bar{S}_3 = 0$. Let the field and the velocity experience a sudden change in their values at $t = 0$ for some reason. We will be interested in the law according to which the field and the velocity, $E(t)$ and $U(t)$, relax to their steady-state values. That is why, in what follows, by V_E and U, we mean their deviations from the steady-state values, rather then their absolute values. Accordingly, in the expression for $\partial F_0/\partial x_1$ in kinetic equation (4), we must retain only the term proportional to E and discard the terms proportional to the derivatives of the density and temperature.

3. SOLUTION OF THE KINETIC EQUATION AND CALCULATION OF THE PARTIAL FLUXES

Keeping in mind the remarks made at the end of the previous section, we proceed to a solution of kinetic equation (4). Recall that the derivative $\partial F/\partial t$ is assumed to be sufficiently large for locally and toroidally trapped particles with low longitudinal velocities to give an insignificant contribution to the diffusive fluxes, as is the case in a steady state in the plateau regime. We expand the function $U(x_2, x_3)$ in a power series in the small parameters $b_2 = \delta\cos x_2$ and $b_3 = \varepsilon\cos x_3$,

$$\frac{B_0}{B}u = u_0 + \frac{\mu B_0 + u_0^2}{u_0}(b_2 + b_3),$$
$$u_0 = \delta\left[2\mathscr{E} - \frac{e}{m}\Phi - \mu B_0\right]^{1/2}, \qquad (12)$$

and switch from the variables $\mathscr{E}$ and μ to the conventional dimensionless variables $z = u_0/v_T$ and $w = \mu B/v_T^2$. We also set

$$F = (1 + \bar{\Psi} + \tilde{\Psi})F_M, \quad \bar{\Psi}, \tilde{\Psi} \ll 1, \qquad (13)$$

where $\bar{\Psi}$ is the part of the distribution function that is independent of the angular variables x_2 and x_3 and is odd in z (this part is unimportant for our purposes because it does not contribute to the fluxes S_2 and S_3). As a result, we arrive at the following equation for the varying (in x_2 and x_3) part $\tilde{\Psi}(x_2, x_3)$ of the distribution function:

$$\frac{\partial\tilde{\Psi}}{\partial t} + \frac{M}{R_0}\frac{B^{(2)}}{B^{(3)}}zv_T\frac{\partial\tilde{\Psi}}{\partial x_2} + \frac{M}{R_0}zv_T\frac{\partial\tilde{\Psi}}{\partial x_3} + \nu_i\tilde{\Psi}$$
$$= \frac{w+z^2}{\delta R_0}\left[(n+\delta M\Theta_J)\frac{\partial b_3}{\partial x_3} - \frac{\partial b_2}{\partial x_2}\right]V_E(t) \qquad (14)$$
$$+ \nu_i\frac{w-z^2}{zv_T}(b_2 + b_3)U(t).$$

Since the right-hand side of inhomogeneous equation (14) is a sum of two terms, one of which depends only on x_2, and the other, only on x_3, it is natural to seek a solution in the form of the sum

$$\tilde{\Psi}(x_2, x_3) = \Psi_2(x_2) + \Psi_3(x_3), \qquad (15)$$

where the functions Ψ_2 and Ψ_3 are independent of x_3 and x_2, respectively. We substitute representation (15) into Eq. (14) and introduce the dimensionless time $\tau = t\Theta v_T/r$ (where $\Theta = \Theta_J$ for a tokamak and $\Theta = \Theta_s = \delta t$ for a stellarator) to obtain the following equations for the functions Ψ_2 and Ψ_3:

$$\frac{\partial\Psi_2}{\partial\tau} + z\frac{\partial\Psi_2}{\partial x_2} + \nu_t\Psi_2$$
$$= -\frac{w+z^2}{\Theta v_T}\frac{\partial b_2}{\partial x_2}V_E(\tau) + \nu_t\frac{w-z^2}{zv_T}b_2U(t),$$
$$\frac{\partial\Psi_3}{\partial\tau} + qMz\frac{\partial\Psi_3}{\partial x_3} + \nu_t\Psi_3 \qquad (16)$$
$$= \frac{w+z^2}{\Theta v_T}\frac{\partial b_3}{\partial x_3}(n+\delta M\Theta_J)V_E(\tau) + \nu_t\frac{w-z^2}{zv_T}b_3U(t).$$

[2] In [2], formula (95) is misprinted: the term $\Theta_0 NdV_E/dt$ should be replaced with the term $\Theta NdV_E/dt$, where $\Theta = \Theta_J$ for a tokamak and $\Theta = \Theta_s$ for a stellarator.

Here, the dimensionless collision frequency is defined as

$$\nu_t = \frac{r\nu_i}{\Theta v_T}. \quad (17)$$

Note that, in the case of a current-free stellarator, the equation for Ψ_2 was derived by averaging over the variable x_3 and by taking into account relationships (10) and the relationship

$$\sqrt{g} = B_0R_0/MB^{(3)},$$

which follows from formulas (9). Using the relationships

$$b_2 = \delta\cos x_2 = \mathrm{Re}\,\delta e^{ix_2}, \quad b_3 = \varepsilon\cos x_3 = \mathrm{Re}\,\varepsilon e^{ix_3}, \quad (18)$$

we can easily solve Eq. (16). Thus, for example, we obtain

$$\Psi_2(\tau, z, w) = \mathrm{Re}\int_0^\tau ds\left[-iq\frac{w+z^2}{v_T}V_E(s) + \delta\nu_t\frac{w-z^2}{zv_T}U(s)\right]e^{-(\nu_t+iz)(\tau-s)}. \quad (19)$$

The sought-for solution Ψ_3 has an analogous form and can be found from solution (19) by replacing the quantity q with $-(n+\delta M\Theta_J)\varepsilon\Theta^{-1}$, δ with ε, and z in the exponential function with qMz. Substituting the solutions Ψ_2 and Ψ_3 into formulas (3) for the fluxes, averaging over the angular variables x_2 and x_3, and integrating over the velocities w and z yields

$$\bar{S}_2 = -\frac{rv_TN}{M\omega_B} \times\int_0^\tau ds[qV_E(\tau-s)J(s) + \delta\nu_tU(\tau-s)I(s)]e^{-\nu_ts},$$

$$\bar{S}_3 = -\frac{\varepsilon^2v_TRN}{M\omega_B}(n+\delta M\Theta_J) \times\int_0^\tau ds\left[\frac{(n+\delta M\Theta_J)}{\Theta}V_E(\tau-s)J(qMs) - \nu_tU(\tau-s)I(qMs)\right]e^{-\nu_ts}, \quad (20)$$

where

$$J(s) = \left(1 - \frac{\partial^2}{\partial s^2} + \frac{1}{2}\frac{\partial^4}{\partial s^4}\right)e^{-s^2/2} = \frac{1}{2}(7 - 8s^2 + s^4)e^{-s^2/2},$$
$$I(s) = \int_0^s e^{-t^2/2}dt - \frac{1}{2}\frac{\partial^3}{\partial s^3}e^{-s^2/2} = \frac{1}{2}(s^2-3) + \int_0^s e^{-t^2/2}dt. \quad (21)$$

When integrating over the velocities, we used the relationships

$$\int_{-\infty}^{\infty} dz\cdot e^{-z^2/2}\cos sz = \sqrt{2\pi}e^{-s^2/2},$$
$$\int_{-\infty}^{\infty} dz\cdot e^{-z^2/2}\frac{\sin sz}{z} = \sqrt{2\pi}\int_0^s e^{-t^2/2}dt,$$
$$\int_{-\infty}^{\infty} dz\cdot z^{2n}e^{-z^2/2}\cos sz = \sqrt{2\pi}(-1)^n\frac{d^{2n}}{ds^{2n}}e^{-s^2/2}, \quad (22)$$
$$\int_{-\infty}^{\infty} dz\cdot z^{2n-1}e^{-z^2/2}\sin sz = \sqrt{2\pi}(-1)^n\frac{d^{2n-1}}{ds^{2n-1}}e^{-s^2/2},$$
$$n = 1, 2, 3, \ldots.$$

As was mentioned earlier, we are primarily interested in the temporal behavior of the functions $V_E(\tau)$ and $U(\tau)$ on relatively short time scales $t < \nu_i^{-1}$ ($\tau < \nu_t^{-1}$). However, the equations obtained, being slightly modified, make it possible to describe the evolution of the ambipolar field and longitudinal velocity even on long time scales such that $t\nu_i \gg 1$ ($\tau\nu_t \gg 1$). This modification consists in taking account (although not quite accurate) of the influence of the locally and toroidally trapped particles, which was neglected in deriving expressions (20) for the fluxes $\bar{S}_2$ and $\bar{S}_3$. In fact, expansion (12), which was used in the derivation of these expressions, is valid only for sufficiently large values of the velocity z, much larger than the characteristic velocity z_0, which is on the order of $\sqrt{\delta}$ for toroidally trapped particles and $\sqrt{\varepsilon}$ for locally trapped particles. Consequently, when the time variations of the distribution function are slow enough for the collisions to play a dominant role and the time dependence of the distribution function can be neglected, Eqs. (16) for Ψ_2 and Ψ_3 and, accordingly, solutions (19) and (20) fail to hold under the following conditions:

$$\nu_t < \delta^{3/2} \quad \text{for} \quad \Psi_2,$$
$$\nu_t < \varepsilon^{3/2}qM \quad \text{for} \quad \Psi_3. \quad (23)$$

It is well known (see, e.g., [3–5]) that correct solutions satisfying these conditions can only be obtained by taking into account the effect of the toroidally and locally trapped particles. However, although it is impossible to find a rigorous solution to the time-dependent kinetic equation under conditions (23), an approximate solution that qualitatively accounts for the trapped particles is easy to construct. To do this, it is sufficient to calculate fluxes (20) by integrating over the

entire range of velocities z except for the low-velocity range $-z_0^3 < z < z_0^3$ such that $|z| < \delta^{3/2}$ for $\bar{S}_2$ and $|z| < \varepsilon^{3/2}$ for $\bar{S}_3$.[3] Hence, we take into account trapped particles and, instead of formulas (20), arrive at the following expressions for the fluxes $\bar{S}_2$ and $\bar{S}_3$:

$$\bar{S}_2 = -\frac{r\nu_T N}{M\omega_B}$$

$$\times \int_0^\tau ds[qV_E(\tau - s)J_t(s) + \delta\nu_t U(\tau - s)I_t(s)]e^{-\nu_t s},$$

$$\bar{S}_3 = -\frac{\varepsilon^2 \nu_T RN}{M\omega_B}(n + \delta M\Theta_J) \tag{24}$$

$$\times \int_0^\tau ds\left[\frac{(n + \delta M\Theta_J)}{\Theta}V_E(\tau - s)J_s(qMs)\right.$$

$$\left. + \nu_t U(\tau - s)I_s(qMs)\right]e^{-\nu_t s},$$

where

$$J_t(s) = \left[1 - \frac{\partial^2}{\partial s^2} + \frac{1}{2}\frac{\partial^4}{\partial s^4}\right]\left[e^{-s^2/2} - \sqrt{\frac{2}{\pi}}\frac{\sin(s\delta^{3/2})}{s}\right],$$

$$I_t(s) = \left[1 - \frac{1}{2}\frac{\partial^4}{\partial s^4}\right]\left[\int_0^s dt e^{-t^2/2} - \sqrt{\frac{2}{\pi}}\int_0^{s\delta^{3/2}} dt\frac{\sin t}{t}\right], \tag{25}$$

$$J_s(s) = \left[1 - \frac{\partial^2}{\partial s^2} + \frac{1}{2}\frac{\partial^4}{\partial s^4}\right]\left[e^{-s^2/2} - \sqrt{\frac{2}{\pi}}\frac{\sin(s\varepsilon^{3/2})}{s}\right],$$

$$I_s(s) = \left[1 - \frac{1}{2}\frac{\partial^4}{\partial s^4}\right]\left[\int_0^s dt e^{-t^2/2} - \sqrt{\frac{2}{\pi}}\int_0^{s\varepsilon^{3/2}} dt\frac{\sin t}{t}\right]. \tag{26}$$

It is easy to see that, for $s \sim 1$, formulas (26) coincide with formulas (21) to within small quantities on the order of $\delta^{3/2}$ and $\varepsilon^{3/2}$, and it is only for large values of $s > \delta^{-3/2}$ and $\varepsilon^{-3/2}$ that they differ greatly from formulas (21). In other words, trapped particles make a significant contribution to fluxes (24) only under conditions (23) and only on sufficiently long time scales $\tau > \delta^{-3/2}$, $(qM\varepsilon^{3/2})^{-1}$. In the initial stage, $\tau < \delta^{-3/2}$, $(qM\varepsilon^{3/2})^{-1}$, trapped particles do not contribute to the fluxes and have no effect on the relaxation processes regardless of the values of the collision frequency ν_t.

[3] Note that the expressions obtained for the steady-state (at $\partial F/\partial t = 0$) fluxes by using this procedure coincide with the corresponding exact expressions to within coefficients on the order of unity.

4. SET OF EQUATIONS FOR $V_E(\tau)$ AND $U(\tau)$ AND ITS SOLUTION

Substituting expressions (24) for the fluxes $\bar{S}_2$ and $\bar{S}_3$ into Eqs. (11) yields the following integrodifferential equations for $V_E(\tau)$ and $U(\tau)$, or, equivalently, the evolutionary equations for the ambipolar electric field and longitudinal plasma velocity:

$$\frac{dV_E}{d\tau} = -q\int_0^\tau ds e^{-\nu_t s}$$

$$\times \{[J_t(s) + \varepsilon^2\delta^{-2}(n + \delta M\Theta_J)^2 J_s(qMs)]qV_E(\tau - s)$$

$$+ \delta\nu_t[I_t(s) - \varepsilon^2\delta^{-2}(n + \delta M\Theta_J)I_s(qMs)]U(\tau - s)\},$$

$$\frac{dU}{d\tau} = -\delta\int_0^\tau ds e^{-\nu_t s} \tag{27}$$

$$\times \{[J_t(s) - \varepsilon^2\delta^{-2}qM(n + \delta M\Theta_J)J_s(qMs)]qV_E(\tau - s)$$

$$+ \delta\nu_t[I_t(s) + \varepsilon^2\delta^{-2}qMI_s(qMs)]U(\tau - s)\}.$$

To avoid misunderstanding, we again emphasize that the drift velocity in an electric field $V_E(\tau)$ and the longitudinal plasma velocity $U(\tau)$ do not mean their absolute values but rather their deviations from the steady-state values and the fluxes $\bar{S}_2$ and $\bar{S}_3$ are corrections to the steady-state fluxes caused by these deviations.

Although it is impossible to solve Eqs. (27) analytically, they can readily be solved numerically. Before proceeding to a description of the numerical results, we try to find an asymptotic solution to Eqs. (27) by analyzing the dispersion relation. To do this, we set

$$V_E(\tau) = V_0 e^{\Gamma\tau}, \quad U(\tau) = U_0 e^{\Gamma\tau}, \tag{28}$$

insert these representations into Eqs. (27), and take the limit of large τ values. Then, we perform simple manipulations to obtain the following dispersion relation for Γ:

$$\Gamma\left[\Gamma + q^2 G_t(\Gamma_1) + \varepsilon^2(n + \delta M\Theta_J)^2\frac{q}{\delta^2 M}G_s\left(\frac{\Gamma_1}{qM}\right)\right.$$

$$\left. + \delta^2\nu_t Q_t(\Gamma_1) + \varepsilon^2\nu_t Q_s\left(\frac{\Gamma_1}{qM}\right)\right]$$

$$= -q^2\varepsilon^2\nu_t\left[1 + \frac{n + \delta M\Theta_J}{qM}\right] \tag{29}$$

$$\times\left[G_t(\Gamma_1)Q_s\left(\frac{\Gamma_1}{qM}\right) + (n + \delta M\Theta_J)Q_t(\Gamma_1)G_s\left(\frac{\Gamma_1}{qM}\right)\right],$$

where

$$\Gamma_1 = \Gamma + \nu_t, \quad G_{t,s}(z) = \int_0^\infty ds J_{t,s}(s) e^{-zs},$$
$$Q_{t,s}(z) = \int_0^\infty ds I_{t,s}(s) e^{-zs}. \tag{30}$$

Substituting expressions (25) and (26) for $J_{t,s}(s)$ and $I_{t,s}(s)$ into formulas (30), we find

$$G_{t,s}(z) = \frac{1}{2}z(3-z^2) + \left(1 - z^2 + \frac{1}{2}z^4\right)P(z)$$
$$- \sqrt{\frac{2}{\pi}}\arctan\left(\frac{\Delta_{t,s}}{z}\right),$$
$$Q_{t,s}(z) = \frac{1}{2}(z^2-1) + \frac{1}{2}z^{-1}(2-z^4)P(z) \tag{31}$$
$$- z^{-1}\sqrt{\frac{2}{\pi}}\arctan\left(\frac{\Delta_{t,s}}{z}\right),$$

where

$$P(z) = \left[\sqrt{\frac{\pi}{2}} - \int_0^z dt e^{-t^2/2}\right]e^{z^2/2},$$
$$\Delta_t = \delta^{3/2}, \quad \Delta_s = \varepsilon^{3/2}. \tag{32}$$

We solve Eq. (29) in two limiting cases, $\Gamma \ll 1$ and $\Gamma \gg 1$; moreover, in the second case, we set $\Gamma \ll qM$, which is valid for $M \gg n$, as will be clear later. In this way, we need to know how the functions $G_{t,s}(z)$ and $Q_{t,s}(z)$ behave at small and large values of z. The corresponding expressions can readily be derived from formulas (31) and (32).

For $z \ll 1$, we have

$$G_{t,s}(z) \simeq \sqrt{\frac{2}{\pi}}\arctan\left(\frac{z}{\Delta_{t,s}}\right) + O(z),$$
$$Q_{t,s}(z) = z^{-1}G_{t,s}(z). \tag{33}$$

For $|z| \gg 1$ such that $\mathrm{Im}z \gg \mathrm{Re}z$, we have

$$G_t(z) = G_s(z) \simeq \frac{7}{2z} + \frac{z^4}{2}\sqrt{\frac{\pi}{2}}e^{z^2/2} + O(z^{-3}),$$
$$Q_t(z) = Q_s(z) = -\frac{1}{2z^2} - \frac{z^3}{2}\sqrt{\frac{\pi}{2}}e^{z^2/2} + O(z^{-4}). \tag{34}$$

The inequality $qM \gg n$ and the relationship $Q_s(\Gamma_1/qM) = G_s(\Gamma_1/qM)qM/\Gamma_1$, which holds for $\Gamma_1 \ll qM$, allow dispersion relation (29) to be somewhat simplified:

$$[\Gamma + q^2 G_t(\Gamma_1)][\Gamma + \varepsilon^2 qM\nu_t\Gamma_1^{-1}G_s(\Gamma_1/qM)]$$
$$= -\Gamma\left[\delta^2\nu_t Q_t(\Gamma_1) + \varepsilon^2 qM\left(\frac{n+\delta M\Theta_J}{\delta M}\right)^2 G_s\left(\frac{\Gamma_1}{qM}\right)\right]. \tag{35}$$

For $|\Gamma_1| \gg 1$, we can further simplify Eq. (35) by using the inequality $q^2G_t(\Gamma_1) \gg \delta^2\nu_t Q_t(\Gamma_1)$, which is valid by virtue of relationship (34), and also the inequality $\nu_t\Gamma_1^{-1} \ll (n+\delta M\Theta_J)^2(\delta M)^{-2}$:

$$\Gamma + q^2 G_t(\Gamma_1) + \varepsilon^2 qM\left(\frac{n+\delta M\Theta_J}{\delta M}\right)^2 G_s\left(\frac{\Gamma_1}{qM}\right) = 0. \tag{36}$$

We set $\Gamma = i\Omega + \gamma$, where $\Omega \gg 1$ and $\gamma \ll \Omega^{-1}$, and take into account the following consequences of relationships (33) and (34):

$$G_s\left(\frac{\Gamma_1}{qM}\right) \simeq \sqrt{\frac{\pi}{2}}, \quad G_t(\Gamma_1) \simeq G_t(i\Omega) + (\gamma+\nu_t)G_t'(i\Omega),$$
$$G_t(i\Omega) = \frac{7}{2}(i\Omega)^{-1} + \frac{\Omega^4}{2}e^{-\Omega^2/2}, \tag{37}$$

where the prime denotes the derivative with respect to the argument. As a result, we arrive at the following expressions for the dimensionless frequency Ω and the dimensionless damping rate γ:

$$\Omega^2 \simeq \frac{7}{2}q^2,$$
$$\gamma = -\frac{1}{2}\left[\nu_t + \sqrt{\frac{\pi}{2}}\varepsilon^2 qM\left(\frac{n+\delta M\Theta_J}{\delta M}\right)^2 + \frac{1}{7}\sqrt{\frac{\pi}{2}}\Omega^6 e^{-\Omega^2/2}\right]. \tag{38}$$

This solution describes high-frequency weakly damped oscillations whose (dimensionless) frequency is proportional to the safety factor q and whose damping rate is the sum of three terms, of which the first accounts for collisional damping, the second is associated with the longitudinal viscosity and is much larger for a stellarator ($\Theta_J = 0$, $n \neq 0$) than for a rippled tokamak ($n = 0$, $\Theta_J \neq 0$), and the third is in a sense an analogue of the Landau damping rate of a "wave" with the dimensional frequency $\omega = \Omega\Theta v_T/r = \sqrt{3.5}\,v_T/R$ and the wavenumber $k = \Theta r^{-1}$.

Now, we consider the low-frequency branches of slow relaxation processes with $\Gamma \ll 1$, described by dispersion relation (35). Estimates show that, in this case,

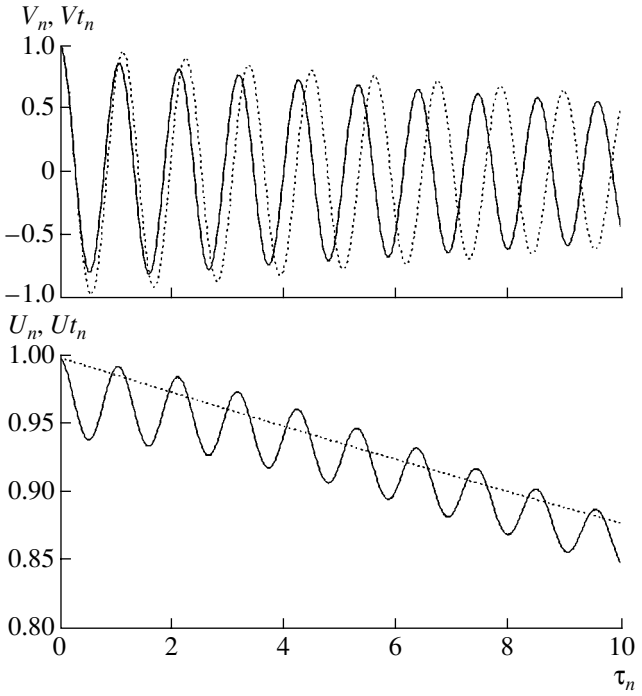

Fig. 1. Functions V_n and U_n (solid curves) and functions Vt_n and Ut_n (dotted curves) calculated for $\delta = 0.1$, $\varepsilon = 0.03$, $n = 0$, $M = 14$, $q = 3$, $V_0 = 1$, $U_0 = 1$, $T = 10$, $N = 800$, $\Omega = 5.613$, $\gamma_1 = 0.05$, and $\gamma_3 = 0.013$.

the right-hand side of this equation can be neglected. As a result, the equation itself splits into two equations,

$$\Gamma + q^2 G_t(\Gamma_1) = 0, \quad \Gamma_1 = \Gamma + \nu_t, \qquad \Gamma + \varepsilon^2 qM\nu_t \Gamma_1^{-1} G_s(\Gamma_1/qM) = 0. \tag{39}$$

The solution to the first equation is

$$\Gamma = -\nu_t\left[1 - \sqrt{\frac{\pi}{2}}\delta^{3/2}q^{-2}\right] \simeq -\nu_t, \tag{40}$$

and the second equation has the solution

$$\Gamma = -\varepsilon^2 qM\sqrt{\frac{2}{\pi}}\arctan\frac{\nu_t}{qM\varepsilon^{3/2}} \ll \nu_t. \tag{41}$$

Hence, for $\tau \gg 1$, the general solution to Eqs. (27) can be represented as

$$V_E(\tau) = V_1 e^{(i\Omega + \gamma_1)\tau} + V_2 e^{\gamma_2\tau} + V_3 e^{\gamma_3\tau}. \tag{42}$$

Here, Ω and γ_1 are given by formulas (38); γ_2 and γ_3 are determined by formulas (40) and (41), respectively; and the coefficients $V_{1,2,3}$ and $U_{1,2,3}$ are specified by the initial conditions.

In principle, it is possible to find the coefficients $V_{1,2,3}$ and $U_{1,2,3}$ by imposing the initial conditions on the highest derivatives in Eqs. (27). However, we do not do so for the following two reasons. First, this way is not quite correct because formula (42) represents an asymptotic solution rather than an exact one. And second, Eqs. (27) are easy to solve numerically on modern personal computers. The results of the corresponding computations are presented in the next section.

5. RESULTS OF A NUMERICAL SOLUTION OF THE EQUATIONS FOR $V_E(\tau)$ AND $U(\tau)$

Here, results are presented from a numerical solution of Eqs. (27) for some specific parameter values of a tokamak with a rippled toroidal magnetic field and an $n = 2$ toroidal stellarator. We begin by explaining what is shown in the figures given below. The solid curves show V_n and U_n as functions of τ_n. The notation V_n and U_n is used to denote the functions $V_E(\tau_n)$ and $U(\tau_n)$ obtained by numerically integrating Eqs. (27) with $\tau_n = Tn/N$ ($n = 0, 1, 2, \ldots, N$), where T is the time scale over which the equations were integrated and T/N is the time integration step. The dotted curves represent the functions

$$Vt_n = V_E(0)e^{-\gamma_1\tau_n}\cos\Omega\tau_n, \quad Ut_n = U(0)e^{-\gamma_3\tau_n},$$

where Ω and γ_1 are given by formulas (38) and γ_3 is determined by formula (41). By comparing V_n and U_n with Vt_n and Ut_n, we can judge to what degree the asymptotic solution coincides with the exact one. Since Eqs. (27) are linear, the functions $V_E(0)$ and $U(0)$ behave independently of their absolute initial values $V_E(\tau)$ and $U(\tau)$; the only important factor is the ratio of $V_E(0)$ to $U(0)$. Consequently, one of these initial values can always be set equal to unity. The parameter values used in computations are given in the figure captions. The first five figures refer to a tokamak, and the last two figures were obtained for a stellarator. All computations were carried out for $\nu_t = 0.1$.

From Fig. 1, we can see that, for sufficiently large values of the safety factor ($q = 3$), the function $V_E(\tau)$ performs weakly damped oscillations around its steady-state value (which is equal to zero in the case in question), the damping rate being determined primarily by collisions. The frequency of the oscillations and their damping rate are seen to be close to those obtained from the dispersion relation. The longitudinal plasma velocity $U(\tau)$ is a superposition of an exponential function decreasing at a rate close to γ_3 and oscillations with a comparatively small (about 3%) amplitude.

For smaller values of the safety factor ($q = 1.5$, Fig. 2), the damping rate of oscillations of the electric field is considerably faster, which agrees with formula (38). A more substantial deviation of V_n from Vt_n is associated with the fact that the theoretical value of the damping rate γ_1 was obtained under the conditions $\Omega \gg 1$ and $\gamma \ll \Omega^{-1}$, which fail to hold for $q = 1.5$. However, as in the previous case, the mean velocity behaves in accordance with dispersion relation (39). For even

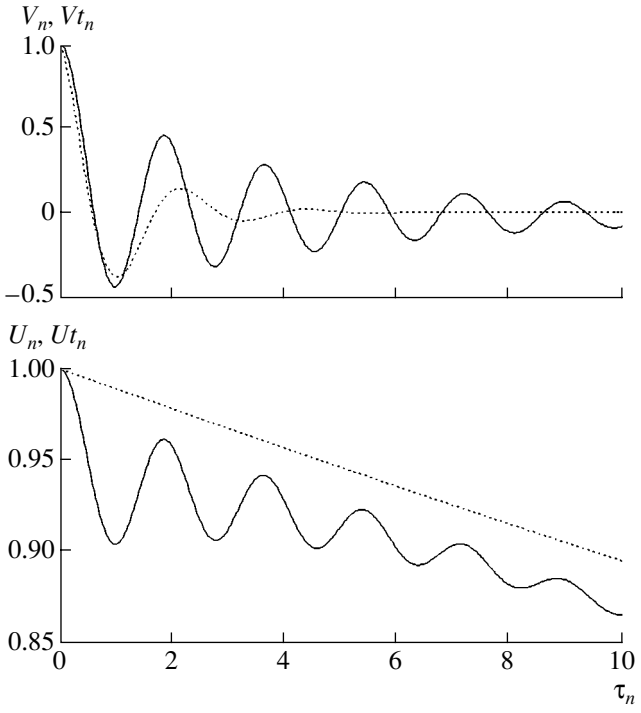

Fig. 2. Same as in Fig. 1, but for $\delta = 0.1$, $\varepsilon = 0.03$, $n = 0$, $M = 14$, $q = 1.5$, $V_0 = 1$, $U_0 = 1$, $T = 10$, $N = 400$, $\Omega = 2.807$, $\gamma_1 = 0.902$, and $\gamma_3 = 0.011$.

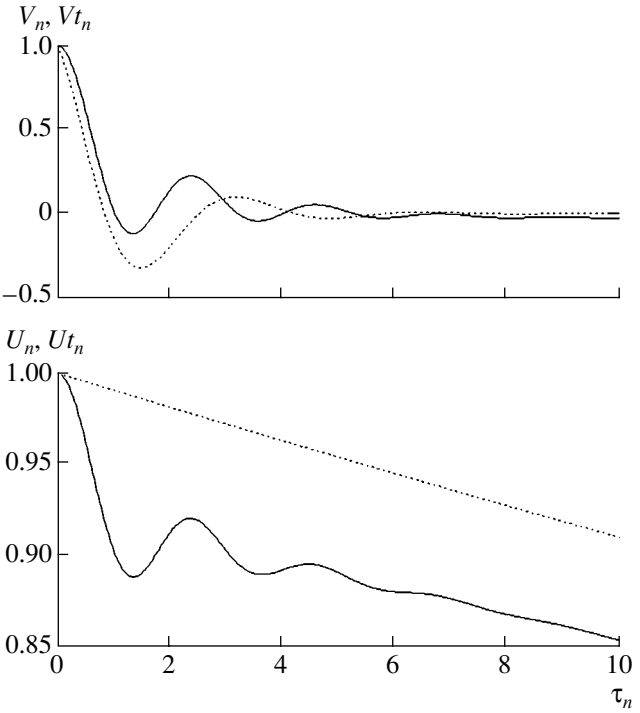

Fig. 3. Same as in Fig. 1, but for $\delta = 0.1$, $\varepsilon = 0.03$, $n = 0$, $M = 14$, $q = 1$, $V_0 = 1$, $U_0 = 1$, $T = 10$, $N = 400$, $\Omega = 1.871$, $\gamma_1 = 0.717$, and $\gamma_3 = 9.469 \times 10^{-3}$.

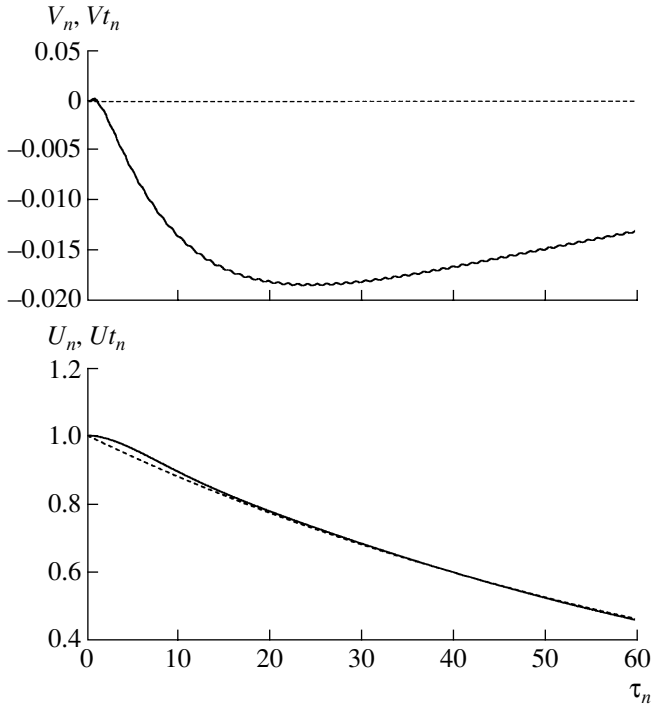

Fig. 4. Same as in Fig. 1, but for $\delta = 0.1$, $\varepsilon = 0.03$, $n = 0$, $M = 14$, $q = 3$, $V_0 = 0$, $U_0 = 1$, $T = 60$, $N = 800$, $\Omega = 5.613$, $\gamma_1 = 0.05$, and $\gamma_3 = 0.013$.

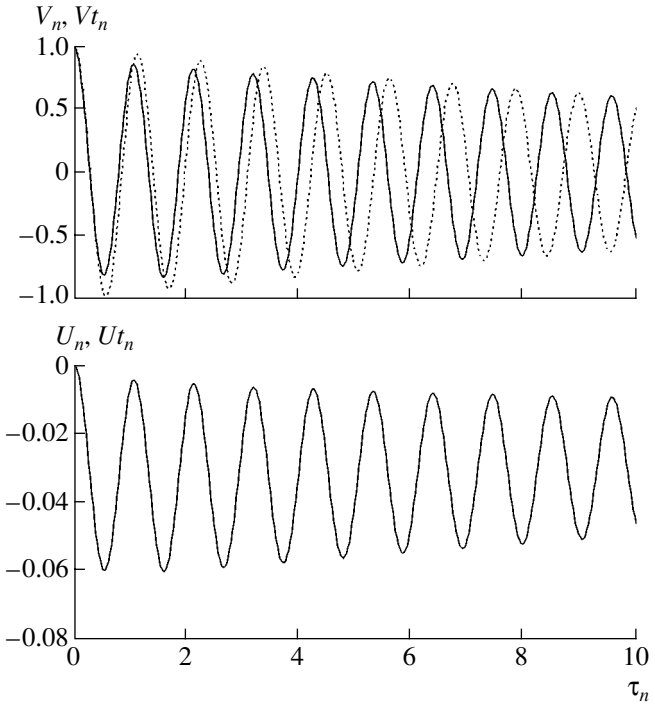

Fig. 5. Same as in Fig. 1, but for $\delta = 0.1$, $\varepsilon = 0.03$, $n = 0$, $M = 14$, $q = 3$, $V_0 = 1$, $U_0 = 0$, $T = 10$, $N = 400$, $\Omega = 5.613$, $\gamma_1 = 0.05$, and $\gamma_3 = 0.013$.

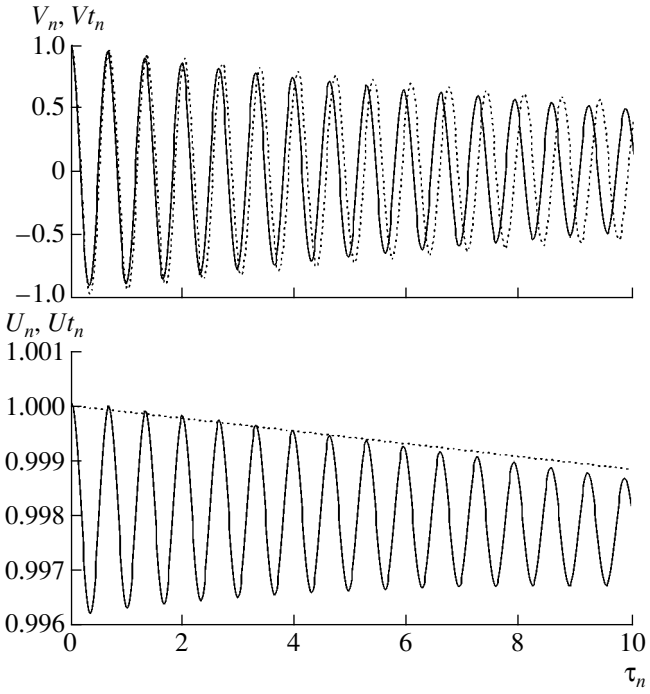

Fig. 6. Same as in Fig. 1, but for $\delta = 0.01$, $\varepsilon = 1.161 \times 10^{-3}$, $n = 2$, $M = 14$, $q = 5.01$, $V_0 = 1$, $U_0 = 1$, $T = 10$, $N = 600$, $\Omega = 9.373$, $\gamma_1 = 0.062$, and $\gamma_3 = 1.163 \times 10^{-4}$.

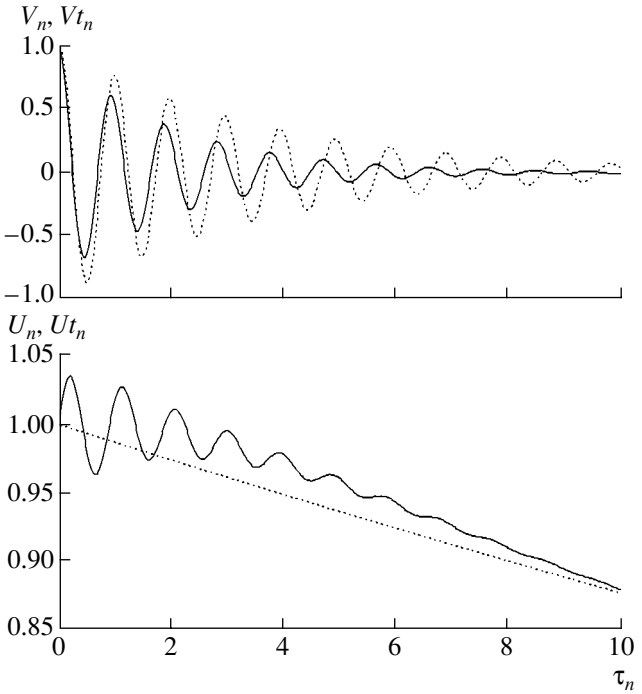

Fig. 7. Same as in Fig. 1, but for $\delta = 0.05$, $\varepsilon = 0.03$, $n = 2$, $M = 14$, $q = 3.428$, $V_0 = 1$, $U_0 = 1$, $T = 10$, $N = 600$, $\Omega = 6.414$, $\gamma_1 = 0.274$, and $\gamma_3 = 0.013$.

smaller values of the safety factor ($q = 1$, Fig. 3), the function $V_E(\tau)$ relaxes in a nearly aperiodic fashion.

When the initial value of the ambipolar field is equal to its equilibrium value (i.e., $V_E(0) = 0$), there are essentially no oscillations (Fig. 4); in this case, the function $V_E(\tau)$, first, becomes negative and then, after a time of about ν_t^{-1}, starts to damp at the same rate γ_3 as the function $U(\tau)$:

$$V_E(\tau) \sim e^{\gamma_2 \tau} - e^{-\gamma_3 \tau},$$

where $\gamma_3 \sim \nu_t$ is given by formula (40).

For $U(0) = 0$, the relaxation of the functions $V_E(\tau)$ and $U(\tau)$ is of an oscillatory nature, although the amplitude of oscillations of the longitudinal velocity (about 3%) is much smaller than the amplitude of oscillations of V_E (Fig. 5).

The relaxation of the ambipolar electric field in a stellarator has much in common with the relaxation in a rippled tokamak. The most significant difference is that, in accordance with formula (38), the effect of the longitudinal viscosity on the damping of the relaxation oscillations in a stellarator is much stronger than that in a rippled tokamak. Thus, in a tokamak, the damping rate of oscillations of $V_E(\tau)$ is essentially insensitive to the longitudinal viscosity. In contrast, even in a stellarator with $q \gg 1$ and $\nu_t \ll 1$, weakly damped oscillations are possible only under the condition

$$\varepsilon^2 \delta^{-2} n^2 q / 2M \ll 1,$$

i.e., only in the central part of the plasma column (because $\varepsilon \sim r^2$). This is illustrated in Figs. 6 and 7, which show the functions $V_E(\tau)$ and $U(\tau)$ calculated for two different radii corresponding to two different ratios of δ to ε.

We will conclude with two general remarks.

In [1], it was mentioned that, for toroidal magnetic confinement systems possessing a symmetry in one of the angular variables, i.e., when $\delta \neq 0$ and $\varepsilon = 0$ or when $\delta = 0$ and $\varepsilon \neq 0$, the right-hand sides of Eqs. (1) differ only by a constant factor. Consequently, for symmetric systems, the functions $V_E(\tau)$ and $U(\tau)$ cannot be uniquely determined from Eqs. (27); in order to do this, it is necessary to take into account the transverse viscosity [6].

According to Eqs. (11), time variations of the ambipolar electric field give rise to additional diffusive (and heat) fluxes, which, in turn, produce small variations in the density and temperature. However, as far as the author is aware, no experimental data are available on the existence of relaxation oscillations of the ambipolar electric field in the toroidal magnetic confinement systems under discussion.

ACKNOWLEDGMENTS

This study was supported by the Russian Foundation for Basic Research, project nos. 99-02-17641 and 00-15-96676.

REFERENCES

1. L. M. Kovrizhnykh, Comm. Plasma Phys. Control. Fusion **18** (5), 309 (1998).
2. L. M. Kovrizhnykh, Fiz. Plazmy **25**, 827 (1999) [Plasma Phys. Rep. **25**, 760 (1999)].
3. A. Galeev and R. Sagdeev, in *Reviews of Plasma Physics*, Ed. by M. A. Leontovich (Atomizdat, Moscow, 1973; Consultants Bureau, New York, 1979), Vol. 7.
4. L. M. Kovrizhnykh, Itogi Nauki Tekh., Ser. Fiz. Plazmy **3**, 239 (1982).
5. L. M. Kovrizhnykh, Nucl. Fusion **24**, 851 (1984).
6. M. N. Rosenbluth, P. H. Rutherford, J. B. Taylor, *et al.*, in *Proceedings of International Conference on Plasma Physics and Controlled Nuclear Fusion Research, Madison, 1971* (IAEA, Vienna, 1971), Vol. 7, p. 495.

Translated by I.A. Kalabalyk

Plasma Physics Reports, Vol. 29, No. 4, 2003, pp. 290–295. Translated from Fizika Plazmy, Vol. 29, No. 4, 2003, pp. 318–324.

PLASMA DYNAMICS

Properties of Soft X-ray Emission from a Fast Capillary Discharge

K. Koláček*, J. Schmidt*, V. Boháček*, M. Řípa*, A. A. Rupasov, A. S. Shikanov**, P. Kubeš***, and J. Kravárik*****

**Institute of Plasma Physics, Academy of Sciences of the Czech Republic, Za Slovankou 3, P. O. Box 17, 18221 Prague 8, Czech Republic*

***Lebedev Physical Institute, Russian Academy of Sciences, Leninskiĭ pr. 53, Moscow, 119991 Russia*

****Department of Electrical Engineering, Czech Technical University, Technická 2, 16627 Prague 6, Czech Republic*

Received September 26, 2002

Abstract—Results are presented from experimental studies of the time resolved, spatially resolved, and spectrally resolved soft X rays emitted along the axis of a fast capillary discharge. *© 2003 MAIK "Nauka/Interperiodica".*

1. INTRODUCTION

One of the most challenging features of high-current pulsed capillary discharges is possibility of their operating as a soft X-ray (SXR) laser. This is because of the stability (due to the small compression ratio) of the pinching discharge column. In practice, there are two main ways of creating the population inversion in capillary discharges: the electron-collisional recombination pumping scheme and the electron-collisional excitation pumping scheme. The recombination pumping scheme usually uses hydrogen-like ions, the upper laser level of which is populated via three-body recombination, while the lower laser level is efficiently depopulated. This is accomplished in evacuated small-diameter (<1 mm) capillaries, in which plasma is created by ablating the wall material and remains in close contact with the wall, which ensures rapid conductive cooling. The gain and the anomalous line intensity ratios, although weakly dependent on the discharge length, were reported, e.g., in [1, 2]. On the other hand, excitation pumping schemes usually use neon or nickel-like ions, whose upper level is populated via electron collisions. This may be achieved in gas-filled capillaries of large diameter (3–6 mm) by a fast current rise (at the rate as high as ~$(1–4) \times 10^{12}$ A/s) in a preionized gas, which ensures the rapid detachment from the capillary wall (by the Z-pinch effect). In this way, the amount of material ablated from the wall is small, and the influence of the wall material on the discharge characteristic in the first half-period of the discharge current is expected to be negligible. The strong amplification of the neonlike Ar IX 46.9-nm line, the demonstration of lasing, and the achievement of the saturation limit and a high average power were reported in [3–5].

In the present paper, we report on the SXR measurements performed with a pulsed capillary discharge at the Institute of Plasma Physics of the Academy of Sciences of the Czech Republic (Prague). The time-integrated and time-resolved spatial and spectral characteristics of SXR emission in the direction of the capillary axis in various discharge regimes are measured.

2. APPARATUS

The apparatus (see Fig. 1) consists of a Marx generator, a coupling section (spacer), a fast capacitor (pulse

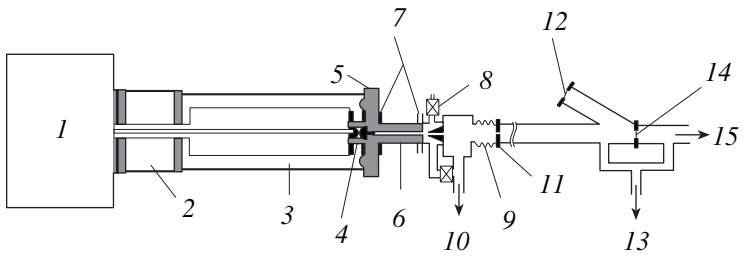

Fig. 1. Schematic of the device: (*1*) oil-filled Marx generator, (*2*) coupling section filled with SF_6, (*3*) fast water capacitor, (*4*) main spark gap, (*5*) insulator, (*6*) capillary, (*7*) Rogowski coil, (*8*) needle valve, (*9*) bellows, (*10*, *13*) vacuum pump, (*11*) diaphragm, (*12*) diagnostic window, (*14*) filter, and (*15*) output to a detector.

1063-780X/03/2904-0290$24.00 © 2003 MAIK "Nauka/Interperiodica"

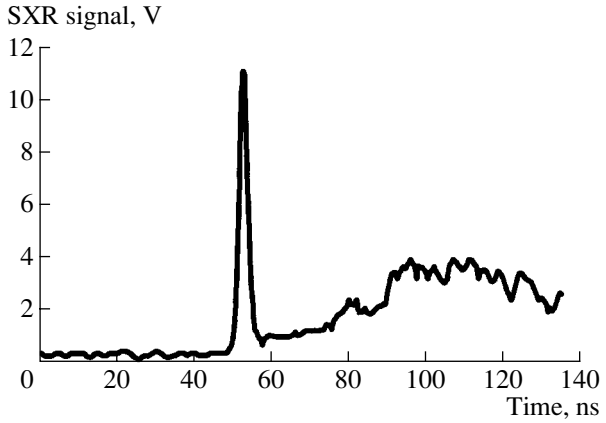

Fig. 2. Signal from a PIN diode filtered with a 0.75-μm Al filter.

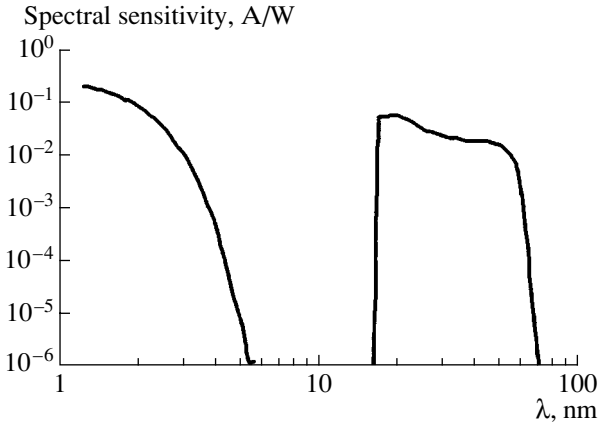

Fig. 3. Spectral sensitivity of a PIN diode covered by a 0.75-μm Al filter.

forming line) with a closely coupled main spark gap, and a capillary. The gas filling and pumping assembly is attached to the outer end of the capillary. The design of the apparatus is described in more detail in [6].

The fully screened oil-insulated Marx generator is used as a power source. It has eight stages, each of them containing two couples (positively and negatively charged) of two 400-nF/100-kV condensers connected in series. The generator (with an erected capacitance of 12.5 nF) is charged by the ±28-kV charging voltage to produce an erected voltage of 448 kV. The short-circuit inductance of the generator is 14.2 μH, and the serial resistance is 5.7 Ω.

The coupling section (spacer) is a SF_6 gas–filled short coaxial cylindrical line with dimensions of $\varnothing 426 \times \varnothing 88 \times 287$ mm (L_s = 95 nH, C_s = 10 pF, and R_s = 95 Ω), which serves as an interface between the oil-insulated Marx generator and the water-filled pulse forming line.

As a fast capacitor, we use a $\varnothing 262 \times \varnothing 158 \times 675$-mm coaxial cylindrical line filled with dielectric (deionized water). Its capacitance C_l = 6.01 nF, inductance L_l = 68.28 nH, and impedance $Z_l = (L_l/C_l)^{1/2}$ = 3.37 Ω. The main spark gap with an attached capillary assembly is placed at the end of the line. The inner part of the spark gap is filled (through the Marx generator, the coupling section, and the fast capacitor) by SF_6 gas, while the outer part of the electrode gap is filled by water. In this way, the spark gap capacitance, which is one of the factors determining the prebreakdown current, is significantly increased. This current preionizes the gas in the capillary, thus ensuring the sufficiently fast rise of the main current, as was mentioned in the introduction. As a result, the plasma in the capillary is very rapidly decoupled from the capillary wall (by the Z-pinch effect) and the amount of the ablated wall material remains small.

The 20-cm-long, 4-mm-diameter polyamide capillary is directly attached to the main spark gap. The capillary is placed in a shielding and circuit-closing metallic cylinder with a diameter of 60 mm. The working gas is injected through an annular slit around the outer surface of the grounded electrode, whereas an axial orifice

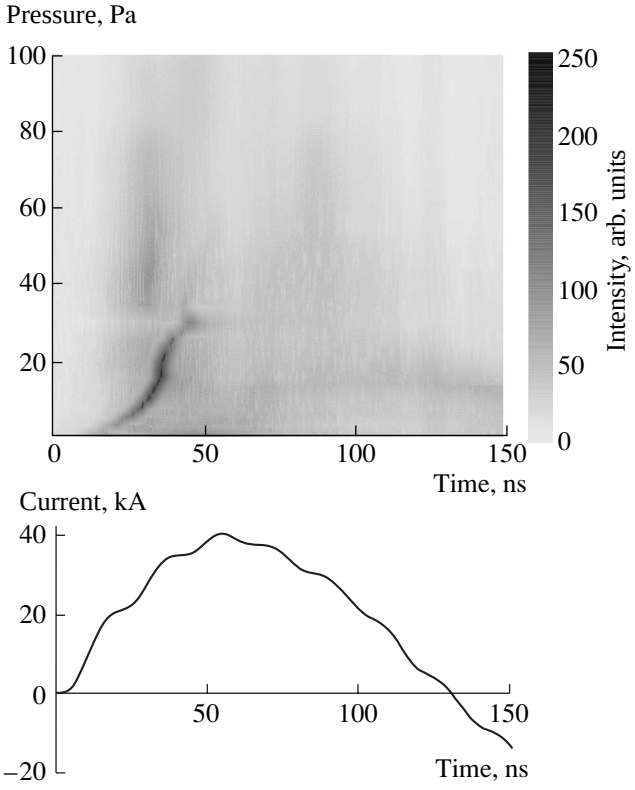

Fig. 4. SXR intensity as a function of time and pressure (on the top) and the waveform of the capillary discharge current (at the bottom).

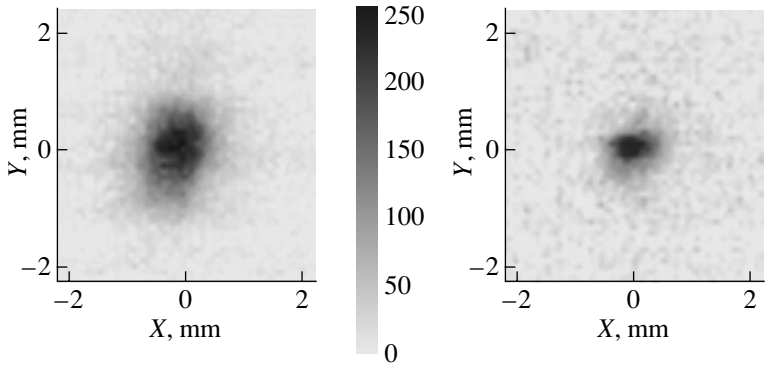

Fig. 5. Time-integrated (on the left) and time-resolved (with an 11-ns exposition that started 15 ns before the current maximum) (on the right) SXR intensities far from capillary mouth (the photos are presented on different intensity scales).

in this electrode is used to pump out the gas and output the generated radiation (see [7] for details).

3. SXR EMISSION ALONG THE CAPILLARY AXIS

3.1. Time-Resolved Spectrally Integrated SXR Signal

Earlier [7], we found the geometry and parameters of the discharge at which the SXR emission along the capillary axis had the time behavior shown in Fig. 2. The SXR emission was detected by a PIN diode covered with a 0.75-μm Al filter (the spectral sensitivity of the detector is given in Fig. 3). These results are very similar to those published three years before us by Rocca *et al.* [4], who reported on the achievement of the saturation limit for the spontaneous emission amplification. Hence, there were reasons to suppose that under our conditions, i.e., in the regime characterized by a short (nanosecond) SXR spike, an amplified spontaneous emission is also present.

One of the important parameters influencing the duration of the SXR signal is the working gas (argon) pressure. The time–pressure diagram of the SXR signal (here, darker shading corresponds to a greater intensity) and a typical time dependence of the discharge current are shown in Fig. 4. The SXR intensity in the direction of the capillary axis was monitored by a PIN diode covered with a 0.75-μm Al filter, and the time derivative of the capillary current was taken by a Rogowski coil and then numerically integrated. An HP 54542C oscilloscope with a 500-MHz bandwidth, 700-ps rise-time, and 2-GHz sample rate in each of four channels was used to record the emission pulses. The high contrast of the SXR peak in comparison with the remaining part of the SXR signal is worthy of mention. However, the fact that this peak appears before the current maximum attests to the possibility of further optimizing the facility regimes and parameters.

3.2. Spatially Resolved Spectrally Integrated SXR Signal

The exit radiation cone coming out of the capillary mouth and collimated with a 0.8-mm orifice (placed at a distance of 372 mm from the capillary mouth) was photographed through the fully opened entrance slit of

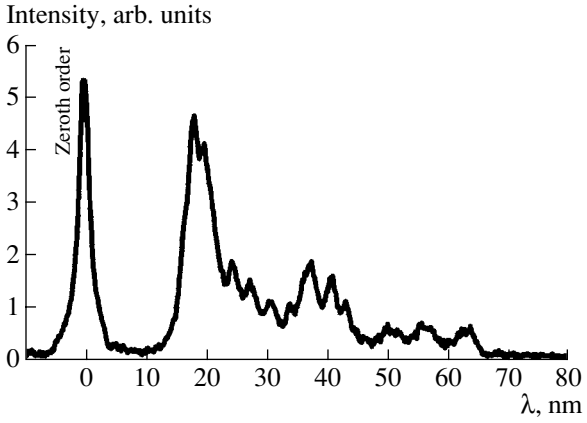

Fig. 6. Capillary discharge spectrum taken by a transmission grating spectrograph 32.1 ns after the current maximum with an exposure time of 11 ns.

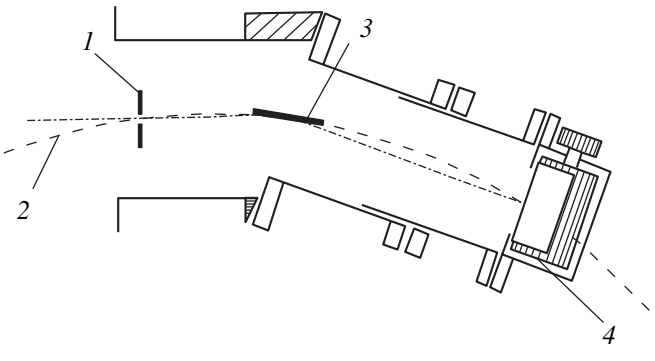

Fig. 7. Grazing-incidence spectrograph LSP-VUV1-3S-M: (*1*) entrance slit, (*2*) Rowland circle, (*3*) diffraction grating, and (*4*) X-ray film.

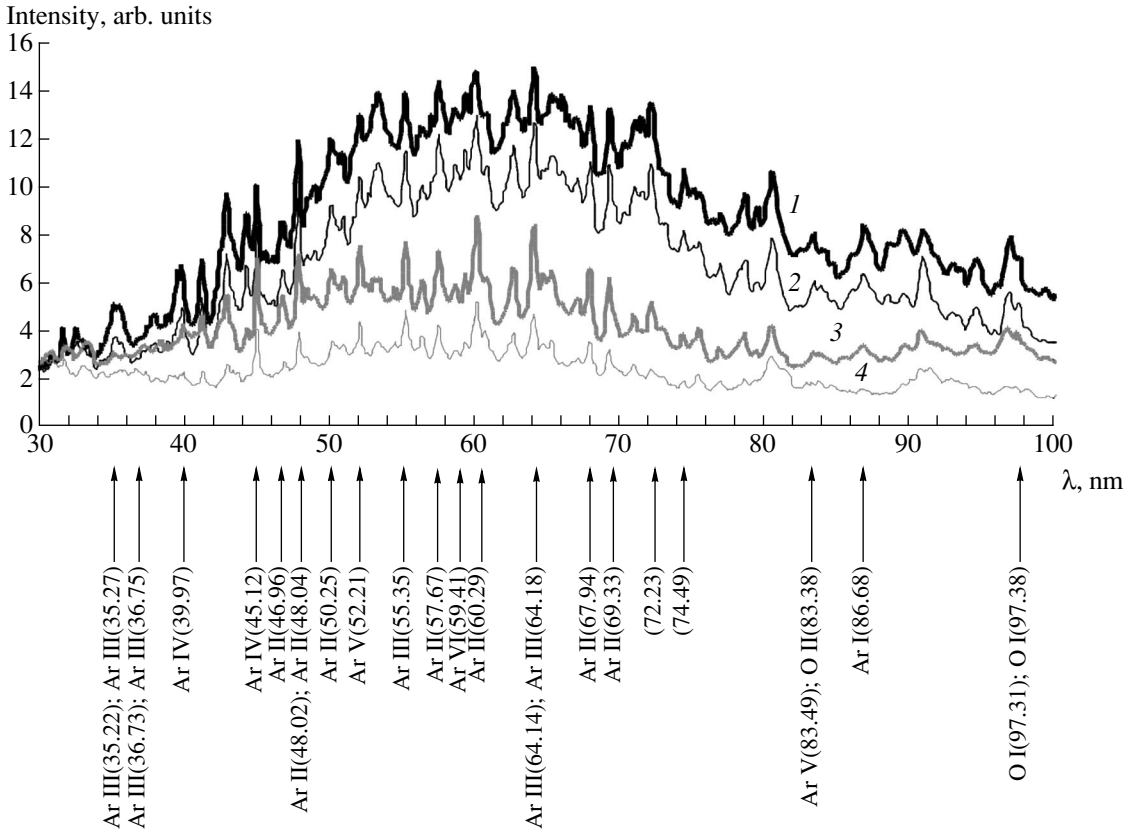

Fig. 8. Time-integrated spectra taken by a grazing-incidence spectrograph at different distances of the entrance slit from the capillary axis: (*1*) 0, (*2*) 0.5, (*3*) 1, and (*4*) 1.5 mm.

the spectrometer (at a distance of 1725 mm from the mouth) in the zeroth order of the toroidal (imaging) diffraction grating. As in the previous case, visible light was cut off by a 0.75-μm Al filter. It turned out (see Fig. 5) that a 2-mm-diameter beam with a flat-top time-integrated profile was well collimated (down to a diameter of 400 μm) in the case of an 11-ns exposition that started 15 ns before near the instant of the current maximum.

3.3. Spectrally Resolved SXR Signal

The first SXR spectral measurements were performed with a simple transmission grating spectrograph (behind a 0.75-μm Al filter). The grating with a step of $d = 1$ μm consisted of $N = 100$ free-standing gold bars of length 1.8 mm with a necessary supporting structure. The grating served as an entrance slit (with a width of $w = 100$ μm) and as a dispersing element with the linear dispersion $D_{\text{lin}} = d/b$, where $b = 346.5$ mm is the distance between the detector and the grating. The diffraction-limited resolution of the grating was $R_d = \lambda/\Delta\lambda_d = N$ and the geometrically limited resolution was $R_g = \lambda/\Delta\lambda_g = \lambda/d[(w/b) + (s + w)/a]$, where $a = 753.5$ mm is the distance between the source and the grating and s is the transverse dimension of the source. At a supposed source dimension of $s = 1$ mm and for the $\lambda = 46.9$ nm neonlike argon line, which is here most interesting to us, these resolutions are $R_d = 100$ ($\Delta\lambda_d = 0.47$ nm) and $R_g = 26.8$ ($\Delta\lambda_g = 1.75$ nm).

The spectra were recorded by two tandem microchannel plates (MCPs) backed with a phosphor screen. The image produced was photographed with a TV camera and digitized with a personal computer.

The time-integrated spectra were smeared, because SXR emission is relatively long and the spectra of various elements (present at the later stages of the discharge) add up with spectra of various ionization states of Ar (present during the first half-period of the discharge current). It should be noted, however, that even the time-resolved spectra (see Fig. 6) had insufficient spectral resolution because of the necessary compromise between the spectral resolution and the exposition time required to obtain a sufficiently intense signal. Besides the zeroth-order signal, there are pronounced spikes corresponding to the cutoff of the Al filter at 17.1 nm in the first, second, and third spectral orders of the transmitting diffraction grating. Since the spectral intensity near the cutoff is relatively high, the profiles of the above spikes can be interpreted as a superposition of the spectral lines of argon and oxygen in various ionization states. It is seen in Fig. 6 that, in the 47 ± 2-nm

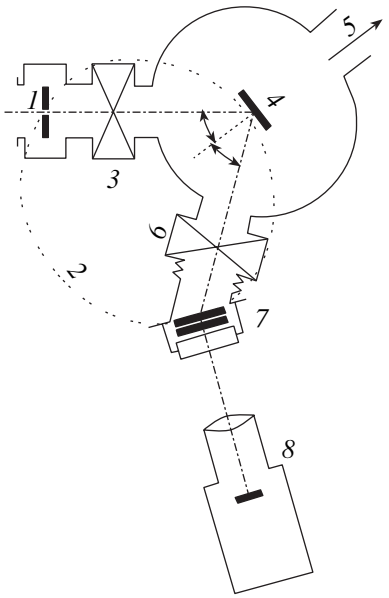

Fig. 9. Seya–Namioka spectrograph with a detection system: (*1*) entrance slit, (*2*) Rowland circle, (*3*, *6*) vacuum valves, (*4*) diffraction grating, (*5*) vacuum pump, (*7*) MCP detector, and (*8*) CCD camera.

spectral range, which is of most interest to us, the intensity is nonzero; however, the insufficiently high spectral resolution of these preliminary measurements does not allow us to separate individual spectral lines in this spectral region.

About fourfold better resolution was expected from the time-integrated spectra taken with an LSP-VUV1-3S-M compact grazing-incidence spectrograph (see Fig. 7) with a fixed 30-μm entrance slit, 4° grazing angle, 300-groove/mm Au-coated grating, 1000-mm radius, 28 × 30-mm ruled area, 30- to 100-nm spectral range, and spectral resolution of $\lambda/\Delta\lambda > 100$. Despite the fact that the drum with an X-ray film was approximately perpendicular to the falling rays and, hence, only a part of the spectrum around the film intersection with the Rowland circle was in focus, only a faintly visible unsharpness could be observed in the off-focus region because of the very small width (2 mm) of the diffracted beam.

Due to time integration, spectral lines of lower ionization states prevail in the spectrum (see Fig. 8). Spectra taken in various positions corresponding to the parallel shift of the spectrometer with respect to the capillary axis confirm the result of Section 3.2 that the diameter of the time-integrated beam is 2 mm.

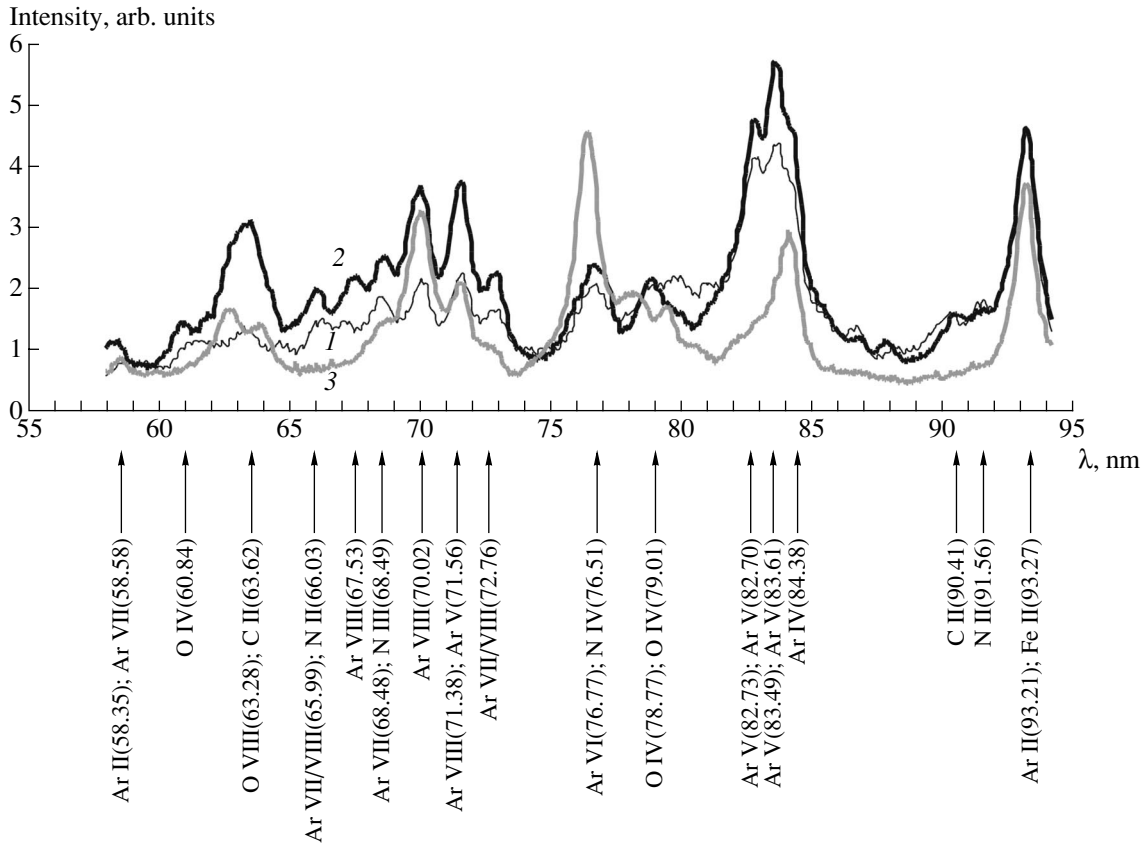

Fig. 10. Time-resolved spectra taken by a Seya–Namioka spectrograph for different shifts Δt of the exposition beginning with respect to the current maximum: (*1*) –22.5, (*2*) –13, and (*3*) 22 ns.

An XUV–visible Seya–Namioka spectrometer (see Fig. 9) with a 1200-groove/mm tungsten-plated toroidal grating (with the tangential and sagittal radii of R_t = 500 mm and R_s = 333 mm, respectively) had approximately the same spectral resolution. Two tandem MCPs were placed tangentially to the Rowland circle. An image produced on a phosphor screen was photographed with a TV camera and digitized with a personal computer.

The spectral lines in the time-integrated spectra were so broadened that they were hardly distinguishable. In the time-resolved spectra (Fig. 10), the Ar VIII lines were identified, whose intensity was maximum in the first half-period of the discharge current. The most intense lines were the Ar V lines corresponding to an ionization potential of 75.02 eV. The only line whose intensity increased by the end of the first half-period of the discharge current was the N IV line.

4. CONCLUSION

Despite the fact that we have observed the same time behavior of the axial SXR emission as Rocca *et al.* [4] (who reported on the achievement of the SXR lasing saturation in a discharge) and despite the fact that we recorded a well-collimated beam at the instant of its maximum compression, our spectroscopic measurements did not indicate lasing at the 46.88-nm line. It is, however, unclear whether (in the time-integrated case) a laser line lasting a nanosecond can be observed against the background of the time-integrated spectra, whether (in the time resolved case) the gating of the detector (MCPs) corresponds exactly to the instant of the maximum compression (simultaneous spectroscopic and PIN-diode measurements were impossible), whether the alignment of the system is good enough, etc. However, our recent numerical simulations [10] confirm that no lasing is required to explain all of the results described above and that they all can be explained in terms of the so-called efficient plasma collapse, driven by a radial shock wave. Therefore, the achievement of lasing inevitably requires the development of reliable methods for monitoring plasma dynamics and determining plasma parameters as functions of the initial (the gas-filling pressure, prepulse current, strength of the external axial magnetic field, etc.) and boundary (the capillary radius and length and the capillary wall material) discharge conditions. A more detailed study is in progress.

ACKNOWLEDGMENTS

This work was performed under auspices and support of the Czech Grant Agency (contract no. 202/98/0831); the Ministry of Education, Youth, and Sports of the Czech Republic (contract no. INGO LA055); and the Russian Foundation for Basic Research (project no. 01-02-17589).

REFERENCES

1. C. Steden and H. J. Kunze, Phys. Lett. A **151**, 534 (1990).
2. H. J. Shin, D. E. Kim, and T. N. Lee, Phys. Rev. E **50**, 1376 (1994).
3. J. J. Rocca, V. Shlyaptsev, F. G. Tomasel, *et al.*, Phys. Rev. Lett. **73**, 2192 (1994).
4. J. J. Rocca, D. P. Clark, J. L. A. Chilla, *et al.*, Phys. Rev. Lett. **77**, 1476 (1996).
5. B. R. Benware, C. D. Macchietto, C. H. Moreno, and J. J. Rocca, Phys. Rev. Lett. **81**, 5804 (1998).
6. K. Koláček, V. Boháček, J. Schmidt, *et al.*, in *Proceedings of the 12th International Conference on High-Power Particle Beams, Haifa, 1998*, Vol. 2, p. 619.
7. K. Koláček, J. Schmidt, V. Boháček, *et al.*, J. Tech. Phys. **40**, 493 (1999).
8. K. Koláček, J. Schmidt, V. Boháček, *et al.*, in *Proceedings of the 13th International Conference on High-Power Particle Beams, Nagaoka, 2000*, Vol. 1, p. 151.
9. R. H. Huddlestone and S. L. Leonard, *Plasma Diagnostic Techniques* (Academic, London, 1965), p. 8.
10. P. Vrba, K. Koláček, J. Schmidt, *et al.*, in *Proceedings of the International Symposium on Plasma Research and Application, Warsaw, 2001*, Paper 3.23.

Translated by the authors

Plasma Physics Reports, Vol. 29, No. 4, 2003, pp. 296–299. Translated from Fizika Plazmy, Vol. 29, No. 4, 2003, pp. 325–328.

DUSTY PLASMA

Interaction between Dust Grains near a Conducting Wall

A. M. Ignatov

Institute of General Physics, Russian Academy of Sciences, ul. Vavilova 38, Moscow, 119991 Russia
e-mail: aign@fpl.gpi.ru

Received September 26, 2002

Abstract—The effect of a conducting electrode on the interaction of dust grains in an ion flow is discussed. It is shown that two grains levitating above the electrode at the same height may attract one another. This results in the instability of a dust layer. © *2003 MAIK "Nauka/Interperiodica".*

1. INTRODUCTION

A good deal of experiments in dusty plasma physics are performed with aerosol grains suspended in a plasma sheath. A negatively charged dust grain in the sheath levitates above a horizontal electrode due to the balance of two forces: the gravity force, directed downward, and the sheath electric field, which pushes the grain upward. The near-sonic or supersonic ion flow in the sheath creates a wake field downstream of the grain. Since the latter is confined by a certain Mach cone, it is commonly accepted that the wake field affects the motion of grains that are situated downstream only. The usual assumption is that the intergrain potential is smooth in the horizontal direction; i.e., two grains levitating at the same height repel one another via the screened Coulomb potential. The structure of the wake field and the grain interaction in an ion flow were studied in detail in [1–6]. The asymmetric interaction of vertically aligned grains was also observed experimentally [7].

In the analytical theory and computer simulations cited above, it was assumed that the plasma density is constant and the influence of the conducting electrode is negligible. Although both assumptions evidently fail under conditions of a real plasma sheath, taking into account the plasma nonuniformity seems to be a very difficult problem. In order to estimate the influence of the electrode on the grain interaction, here we use the zeroth approximation, which seems to be the only one treatable analytically.

In this paper, the following simple model is accepted. Let there be a monoenergetic ion stream entering a conducting electrode (or a grid) located at the horizontal plane ($z = 0$). The stream velocity u exceeds the ion thermal velocity, but it is much less than the electron thermal velocity. The electrons are assumed to obey a Boltzmann distribution. Two problems are addressed: first, how the electrode modifies the interaction between two grains levitating at the same height and, second, how this affects the spectrum of dust acoustic waves propagating along a single dust layer.

2. INTERGRAIN INTERACTION

The electrostatic potential produced by a point charge Q located at $\mathbf{r} = \mathbf{r}_0$ is given by the solution to Poisson's equation

$$\Delta\hat{\varepsilon}\varphi(\mathbf{r}) = -4\pi Q\delta(\mathbf{r} - \mathbf{r}_0), \tag{1}$$

where $\hat{\varepsilon}$ is the operator of the static dielectric permittivity of an ambient plasma. In the accepted model, the spatial Fourier transform of $\hat{\varepsilon}$ is given by

$$\varepsilon(\mathbf{k}) = 1 - \frac{\omega_i^2}{(k_z u + i0)^2} + \frac{k_D^2}{k^2}, \tag{2}$$

where u is the velocity of the ion flow, ω_i is the ion plasma frequency, and k_D is the inverse electron Debye length. The ion flow is parallel to the z-axis and directed downward ($u < 0$).

In an unbounded plasma, the natural boundary condition for Eq. (1) is $\varphi|_{r\to\infty} \longrightarrow 0$. It is convenient to express the solution to Eq. (1) in terms of its Green's function: $\varphi(\mathbf{r}) = QG^0(\mathbf{r} - \mathbf{r}_0)$, where the Fourier transform of $G^0(\mathbf{r})$ with respect to the transverse coordinate $\mathbf{r}_\perp = (x, y)$ is

$$G^0_{k_\perp}(z) = \int \frac{dk_z}{2\pi} e^{ik_z z} \frac{4\pi}{k^2\varepsilon(\mathbf{k})}. \tag{3}$$

Here, $\mathbf{k}_\perp = (k_x, k_y)$ stands for the transverse components of a wave vector. With the dielectric function given by Eq. (2), the zeros of the denominator in Eq. (3) are

$$\begin{aligned} k_z &= \pm k_D q - i0, \\ k_z &= \pm i k_D \kappa, \end{aligned} \tag{4}$$

where

$$q^2 = \frac{1}{2}\left\{\sqrt{(q_\perp^2 + 1 - \mu^2)^2 + 4\mu^2 q_\perp^2} - q_\perp^2 + \mu^2 - 1\right\}, \tag{5}$$

1063-780X/03/2904-0296$24.00

$$\kappa^2 = \frac{1}{2}\left\{\sqrt{(q_\perp^2 + 1 - \mu^2)^2 + 4\mu^2 q_\perp^2} + q_\perp^2 - \mu^2 + 1\right\}, \quad (6)$$

$q_\perp = k_\perp/k_D$ is the normalized transverse wavenumber, and $\mu = \omega_i/k_D u$ is the inverse Mach number.

The integral in Eq. (3) is easily evaluated, resulting in

$$G_{k_\perp}^0(z) = \frac{2\pi}{k_D}\frac{1}{q^2 + \kappa^2}[\kappa e^{-\kappa k_D|z|} + 2\theta(-z)q\sin(qk_D z)]. \quad (7)$$

The spatial structure of the potential is recovered by the Fourier transform of Green's function (7) with respect to $k_\perp$. The first term in parentheses in expression (7) gives rise to the Debye–Hückel potential distorted by the ion flow, while the second term represents the wake field situated downstream of the charge [1–3]. Both the opening of the Mach cone confining the wake and the field structure inside of it depend on the stream velocity.

Now we turn to the evaluation of the electric potential of a charge located near a conducting wall. Let the wall be situated on the $z = 0$ plane, while the charge is placed above it, $z_0 > 0$. The potential is then given by the solution to Eq.(1) supplemented with the boundary condition $\varphi|_{z=0} = 0$. As it is well known from electrostatics, we can make allowance for this boundary condition by introducing the surface charge density $\sigma_{k_\perp}^{\text{ind}}$ induced at the conducting surface. Then, the potential of a unit charge is written as

$$G_{k_\perp}(z, z_0) = G_{k_\perp}^0(z - z_0) + G_{k_\perp}^0(z)\sigma_{k_\perp}^{\text{ind}}. \quad (8)$$

Taking into account the boundary condition $G_{k_\perp}(0, z_0) = 0$, we find the surface charge density $\sigma_{k_\perp}^{\text{ind}}$ and, finally, arrive at

$$G_{k_\perp}(z, z_0) = G_{k_\perp}^0(z - z_0) - \frac{G_{k_\perp}^0(z)G_{k_\perp}^0(-z_0)}{G_{k_\perp}^0(0)}. \quad (9)$$

One may doubt whether the description of a bounded dispersive medium in terms of the response function of an unbounded medium is justifiable. However, more accurate and lengthy calculations give the same result. The physical reason is that there are no ions reflected by the conducting wall within the present model. The mathematical reason is that Eq. (1) actually masks a set of partial differential equations with two real characteristics directed downward.

Of particular interest for the following is the interaction potential of two charges placed at the same height z_0. Since

$$G_{k_\perp}(z_0, z_0) = \frac{4\pi}{k_D}\frac{e^{-\kappa a}}{\kappa^2 + q^2}[\kappa\sinh(\kappa a) + q\sin(qa)], \quad (10)$$

where $a = k_D z_0$, the normalized potential is

$$w(\rho) = 2\int_0^\infty q_\perp dq_\perp J_0(q_\perp\rho) \times \frac{e^{-\kappa a}}{\kappa^2 + q^2}[\kappa\sinh(\kappa a) + q\sin(qa)], \quad (11)$$

where $G(r_\perp, z_0, z_0) = k_d w(\rho)$ and $\rho = k_d r$. The asymptotic behavior of $w(\rho)$ is determined by Eq. (10) at $q_\perp \longrightarrow 0$. The latter essentially depends on whether the ion flow is supersonic or subsonic. In the case of a supersonic flow ($\mu < 1$), roots (5) and (6) at $q_\perp \longrightarrow 0$ are approximated as

$$q \approx q_\perp\frac{\mu}{\sqrt{1 - \mu^2}}, \quad \kappa \approx \sqrt{1 - \mu^2}, \quad (12)$$

and the leading term of the asymptotic expansion of $w(\rho)$ (11) is

$$w(\rho)|_{\rho\to\infty} \sim \frac{2}{\mu}(1 - \mu^2)^{3/2}e^{-a\sqrt{1-\mu^2}}\frac{\theta(a\mu - \rho\sqrt{1 - \mu^2})}{\sqrt{a^2\mu^2 - \rho^2(1 - \mu^2)}} + O(e^{-r}). \quad (13)$$

This expression may be interpreted as a mirror reflection of the wake field produced by the grain at $0 < z < z_0$. A more detailed numerical investigation of potential (13) shows that $w(\rho)$ is always positive for $\mu < 1$.

Quite another behavior is observed for the case of a subsonic flow ($\mu > 1$). Roots (5) and (6) at $q_\perp \longrightarrow 0$ are now

$$q \approx \sqrt{\mu^2 - 1}, \quad \kappa \approx q_\perp\frac{\mu}{\sqrt{\mu^2 - 1}}, \quad (14)$$

while the potential at infinity behaves like

$$w(\rho)|_{\rho\to\infty} \sim \frac{2a\mu}{\mu^2 - 1}\sin(a\sqrt{\mu^2 - 1})\frac{1}{\rho^3}. \quad (15)$$

The most important distinction between expressions (13) and (15) is that in the subsonic regime the potential is attractive if

$$\sin(a\sqrt{\mu^2 - 1}) < 0. \quad (16)$$

The numerically evaluated example of potential (15) demonstrating the attraction is depicted in Fig. 1. It should be pointed out that inequality (16) guarantees the long-range attraction between grains. With the opposite inequality imposed on a and μ, the potential is

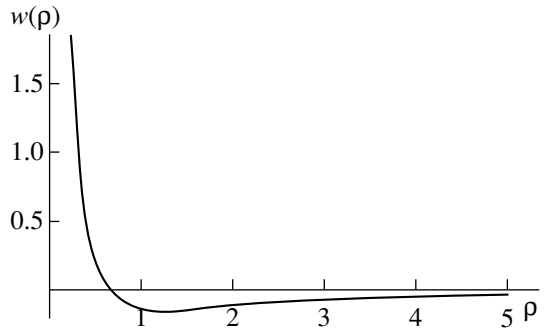

Fig. 1. Distribution of the potential in the transverse direction for $\mu = 2$ and $a = 2.7$.

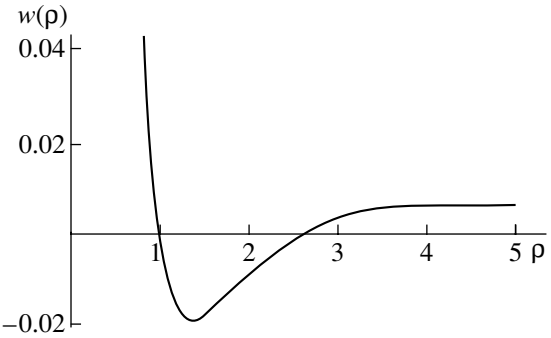

Fig. 2. Distribution of the potential in the transverse direction for $\mu = 2$ and $a = 4$.

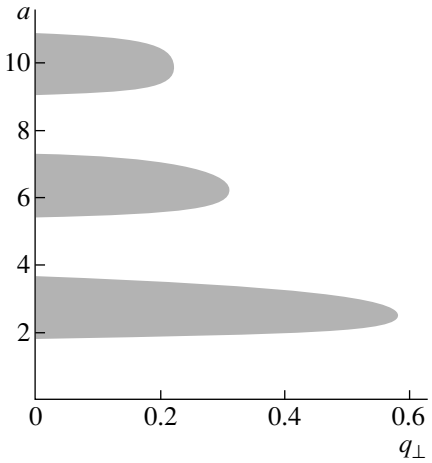

Fig. 3. Instability regions in the $(q_\perp, a)$ plane for $\mu = 2$.

repulsive at large distance but the attractive branch may appear at smaller scales, as is shown in Fig. 2.

Evidently, the existence of an attractive branch of the interparticle interaction may result in the formation of various patterns and clusters even in the absence of an external potential well confining grains in the horizontal direction. Also, the even distribution of grains in a dust layer may become unstable. The latter possibility is discussed in the next section.

3. DUST LAYER

Now we consider a two-dimensional gas consisting of dust grains hovering over a conducting electrode. Ignoring intergrain correlations, the linearized equations of motion are written as

$$\frac{\partial \sigma}{\partial t} + \nabla_\perp(\sigma_0 \mathbf{v}) = 0, \tag{17}$$

$$\frac{\partial \mathbf{v}}{\partial t} = -\nu\mathbf{v} - \frac{Q^2}{M} k_d \nabla_\perp \int d\mathbf{r}'_\perp w[k_D(\mathbf{r}_\perp - \mathbf{r}'_\perp)], \tag{18}$$

where σ_0 is the unperturbed value of the surface density and σ is the density perturbation. Here, we consider horizontal motions only; i.e., $v_z = 0$. The term $-\nu\mathbf{v}$ in Eq. (18) corresponds to the grain friction on an ambient neutral gas. The intergrain interaction is described by the potential given by Eq. (11). Although the grain charge Q generally depends on the ambient plasma parameters, for simplicity we ignore its variability.

Assuming that all of the quantities are proportional to $\exp(-i\omega t + i\mathbf{k}_\perp \mathbf{r}_\perp)$, we easily get the dispersion relation for the gas oscillations

$$\omega(\omega + i\nu) = g_d \frac{k_\perp^2}{2\pi} G_{k_\perp}(z_0, z_0), \tag{19}$$

where $g_d = 2\pi Q^2 \sigma_0 / M$.

This expression describes dust sound waves in the continuous medium approximation. In the long-wavelength limit, $q_\perp \longrightarrow 0$, the dispersion relation takes the form

$$\omega(\omega + i\nu) = \frac{g_d k_d q_\perp^2}{\sqrt{|1-\mu^2|}} \begin{cases} e^{-a\sqrt{1-\mu^2}} \sinh(a\sqrt{1-\mu^2}), & \mu < 1, \\ \sin(a\sqrt{\mu^2-1}), & \mu > 1. \end{cases} \tag{20}$$

Evidently, the layer is unstable; i.e., $\mathrm{Im}\,\omega > 0$ if $G_{k_\perp}(z_0, z_0) < 0$. In the long-wavelength limit, this is possible only in a subsonic flow and the corresponding constraint coincides with Eq. (16). A more detailed investigation shows that the potential $G_\perp(z_0, z_0)$ is always positive if $\mu < 1$. However, in the subsonic regime ($\mu > 1$), there are regions of instability; i.e., $G_{k_\perp}(z_0, z_0) < 0$ if $0 < q_\perp < q_{\max}(a, \mu)$. The latter are shown as shaded areas in Fig. 3. With increasing distance ($a \longrightarrow \infty$) to the wall or decreasing stream velocity ($\mu \longrightarrow \infty$), the instability regions shrink to zero, $q_{\max}(a, \mu) \sim a^{-1/2}, \mu^{-1/2}$.

4. CONCLUSION

To summarize, we have shown that the presence of a conducting wall may drastically change the electrostatic interaction of dust grains in an ion flow. In particular, the electrostatic image of the grain wake field may result in attraction between grains levitating at the same height, which, in turn, yields a Jeans-type instability of the dust layer.

It would be unduly naive to draw quantitative conclusions from the present calculations. However, it seems reasonable that even in a real plasma sheath, which is essentially nonuniform, the electrostatic image of the grain wake field may also affect the motion of another grains outside the Mach cone. Although the screened Coulomb interaction is observed in most experiments, there are indications that the intergrain potential may be more complicated. It was recently reported that, under certain conditions, a void (i.e., a dust-free region) appears in the central part of a single dust layer [8]. The appearance of a two-dimensional void in a layer consisting of some hundreds of grains can hardly be explained in the same manner as a three-dimensional void; the latter requires a strong influence of the dust component on the discharge structure [9]. Although currently one cannot exclude that some additional external forces appeared in the experiment of [8], we can conjecture that the two-dimensional void formation is provided by the complicated intergrain interaction, e.g., the one described in this paper.

ACKNOWLEDGMENTS

This study was supported in part by the Russian Foundation for Basic Research (project no. 02-02-16439) and the Netherlands Organization for Scientific Research (NWO) (grant no. 047.008.013).

REFERENCES

1. Ya. L. Al'pert, A. V. Gurevich, and L. P. Pitaevskiĭ, *Artificial Satellites in a Rarefied Plasma* (Nauka, Moscow, 1964).
2. M. Nambu, S. V. Vladimirov, and P. K. Shukla, Phys. Lett. A **203**, 40 (1995).
3. V. S. Vladimirov and M. Nambu, Phys. Rev. E **52**, R2172 (1995).
4. O. Ishihara and S. V. Vladimirov, Phys. Plasmas **4**, 69 (1997).
5. G. Lapenta, Phys. Rev. E **62**, 1175 (2000).
6. G. Lapenta, Phys. Rev. E **66**, 026409 (2002).
7. A. Melzer, V. A. Schweigert, and A. Piel, Phys. Rev. Lett. **83**, 3194 (1999).
8. R. P. Dahiya, G. V. Paeva, W. W. Stoffels, *et al.*, Phys. Rev. Lett. **89**, 125001 (2002).
9. D. Samsonov and J. Goree, Phys. Rev. E **59**, 1047 (1999).

Translated by the author

Plasma Physics Reports, Vol. 29, No. 4, 2003, pp. 300–306. Translated from Fizika Plazmy, Vol. 29, No. 4, 2003, pp. 329–335.

BEAMS IN PLASMA

Quasilinear Relaxation of a Low-Density Electron Beam in a Plasma

V. G. Ledenev and A. P. Starygin

Institute of Solar and Terrestrial Physics, Siberian Division, Russian Academy of Sciences, Irkutsk, 664033 Russia

Received July 24, 2002

Abstract—The quasilinear relaxation of a low-density electron beam under the action of plasma turbulence, which is generated during the development of a beam instability, when the beam is formed due to rapid local electron heating (acceleration) is analyzed in the one-dimensional approximation. It is shown that quasilinear diffusion results in the formation of a local plateau at the top of the electron distribution function without causing any significant spread in velocities of the beam electrons and that the relaxation process proceeds primarily through the spatial expansion of electrons with different velocities. © *2003 MAIK "Nauka/Interperiodica".*

1. INTRODUCTION

The propagation of electron beams in a plasma during the development of a beam instability has been studied fairly well (see, e.g., [1]). The main effect accompanying the propagation of electron beams is thought to be the quasilinear relaxation of the electron distribution function under the action of plasma waves generated by the beam instability [2]. The quasilinear relaxation leads to the formation of a so-called "plateau" in the electron distribution function; as a result, the beam instability is suppressed. The quasilinear relaxation process was investigated both experimentally [3] and numerically [4]. A model based on this relaxation effect is used, in particular, to interpret type-III bursts of radio emission from the Sun [5, 6]. However, in order for the plateau to form, the electron beam should be sufficiently dense and the electron distribution function should be uniform over a sufficiently long distance for a sufficiently long time, because each of the excited plasma waves interacts with electrons having a definite velocity. When the electron distribution function changes in time and space, the excited waves sooner or later depart from resonance with the electrons because the wave group velocity is low. The resonance is destroyed at the fastest rate when an electron beam is formed as a result of rapid energy deposition in a small local region. The electrons escaping from the deposition region quickly fly apart in space; as a result, at each spatial point and at any given time, there are electrons with a certain velocity (in the case of free expansion, these are electrons with the velocity $v = x/t$, where x is the distance from the energy deposition region and t is the time from the instant of deposition). The shorter the heating (acceleration) time of the electrons and the smaller the energy deposition region, the smaller the velocity spread at each spatial point. Consequently, an important role in the relaxation of an electron beam is played by the kinematic effect of the spatial expansion of electrons with different velocities. This situation can occur, e.g., in type-III solar radio bursts, which are generated by low-density electron beams [7].

2. ANALYSIS BY THE PERTURBATION METHOD

It is natural to assume that, at the very beginning of the generation of radiation, the distribution function of high-energy electrons has the form corresponding to the case of free expansion: $f(v, x, t) = F(x - vt)$, where F is an arbitrary function. The distribution function f can be specified as $f(v, x, t) = A\exp[-(x - vt)^2/(\Delta v)^2 t_0^2]$, where Δv is the electron velocity spread, t_0 is the heating time, and A is the normalizing coefficient. At each point in the spatial region $x \gg \Delta v t_0$, a narrow spectrum of plasma waves with phase velocities $v_f \approx x/t$ is excited. Because of the low group velocity, these waves depart from resonance with the electrons on a time scale of about $\Delta t \sim \Delta v t_0/(v - \Delta v t_0/t)$; i.e., for $t \gg t_0$, we have $\Delta t \sim \Delta v t_0/v$. In order for the instability to occur, it is necessary that its growth rate exceed its damping rate, which is determined by the larger of two quantities: the Coulomb collision frequency or the reciprocal of the time in which the resonance is destroyed, $(\Delta t)^{-1}$. If the damping rate of the plasma waves is determined by the latter parameter, then we can set the growth rate to be $\gamma \approx (n_b/n_0)(v/v_{tb})^2\omega_{pe}$ [8] (where n_b is the beam density, n_0 is the density of the background plasma, ω_{pe} is the electron plasma frequency, and v_{tb} is the velocity spread of the beam) and compare the reciprocal of the growth rate with the time scale on which the resonance is destroyed in order to obtain the following estimate of the beam density for $v \sim v_{tb} \sim \Delta v t_0/t$ at the stability boundary: $n_b/n_0 \sim v/(\Delta v \omega_{pe} t_0)$. According to this estimate, the higher the beam velocity and the shorter the

1063-780X/03/2904-0300$24.00

heating time, the higher the beam density required for the onset of the instability. This is because the time during which the plasma waves depart from resonance with the electrons decreases with increasing beam velocity and decreasing heating time. Thus, for the parameter values characteristic of type-III solar bursts, i.e., for heating to a temperature of about $T \sim 10^7$ K ($\Delta v \sim 10^9$ cm/s) and for $t_0 \sim 0.1$ s, $v \sim 10^{10}$ cm/s, and $\omega_{pe} \sim 10^9$ s^{-1}, we obtain $n_b/n_0 \sim 10^{-7}$, i.e., $n_b \sim 40$ cm^{-3}. This estimate approximately corresponds to the beam densities at which the growth rate becomes higher than the Coulomb collision frequency in the solar corona. After the onset of instability, the evolution of the electron beam is governed by the combined action of the kinematic effect of the spatial expansion of the beam electrons and the quasilinear effect of the excited plasma waves on the electron distribution function.

Let us consider the initial stage of the evolution of the electron distribution function under the action of plasma waves generated by the beam instability. In the one-dimensional approximation, the interaction of electrons with plasma waves is described by the kinetic equation [1, 2]

$$\partial f/\partial t + v(\partial f/\partial x) = (\partial/\partial v)[D(\partial f/\partial v)], \qquad (1)$$

where $D = (8\pi^2 e^2/m^2)W/v$, e and m are the charge and mass of an electron, and W is the spectral energy density of the waves.

We assume that, in a certain local region, rapid electron heating results in the formation of a broad electron energy spectrum. Recall that, in the case of the free expansion of hot electrons from the heating region, their distribution function can be represented in the form $f_0(v, x, t) = A\exp[-(x - vt)^2/(\Delta v)^2 t_0^2]$, which satisfies Eq. (1) with zero on the right-hand side. For a sufficiently low spectral energy density W (e.g., at the onset of beam instability), the electron distribution function can naturally be represented as $F = f_0 + f_1$ with $f_1 \ll f_0$, where f_1 is the perturbation of the distribution function under the action of plasma waves. The perturbation can be determined by solving Eq. (1) with the right-hand side written in terms of $f_0(v, x, t)$. Under the assumptions W = const and $t \gg t_0$, the solution has the form

$$F(v, x, t) = A\exp\left[-\frac{(x - vt)^2}{(\Delta v)^2 t_0^2}\right] \times\left\{1 + \frac{2BW}{(\Delta v)^2 t_0^2 v}\left[\frac{t^3}{6} - \frac{xt^2}{2v} + \frac{2(x - vt)^2 t^3}{3(\Delta v)^2 t_0^2}\right]\right\}, \qquad (2)$$

where $B = 8\pi^2 e^2/m^2$.

Figure 1 shows the electron distribution functions calculated by formula (2) at different distances from the heating region at a fixed time for two cases: (i) free expansion and (ii) developed plasma turbulence. We can see that the main effect of the interaction of plasma waves with electrons is an increase in the electron velocity spread. This effect stems from the fact that the electrons are subject to diffusion in velocity space at both (positive and negative) slopes of the distribution function. At the positive slope, diffusion occurs due to the energy transfer to the excited plasma waves, whereas, at the negative slope, diffusion results from the absorption of the waves generated by faster electrons. The faster the electrons, the more efficiently they will interact with plasma turbulence, because, as can be seen from Eq. (1), at a constant spectral energy density of the turbulence, the diffusion coefficient in energy space is proportional to the electron velocity.

If the electrons in the energy deposition region are accelerated, then the spatial distribution of their density peaks at a certain directed electron velocity. In this case, the distribution function of the freely moving

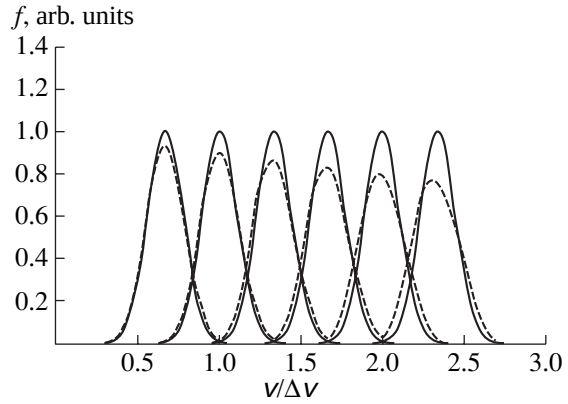

Fig. 1. Electron velocity distribution functions calculated at the time $t = 50t_0$ for $BWt_0/(\Delta v)^3 \sim 10^{-10}$ and for different distances from the heating region (from $50\Delta v t_0$ to $175\Delta v t_0$) in the cases of free expansion (solid curves) and developed plasma turbulence (dashed curves).

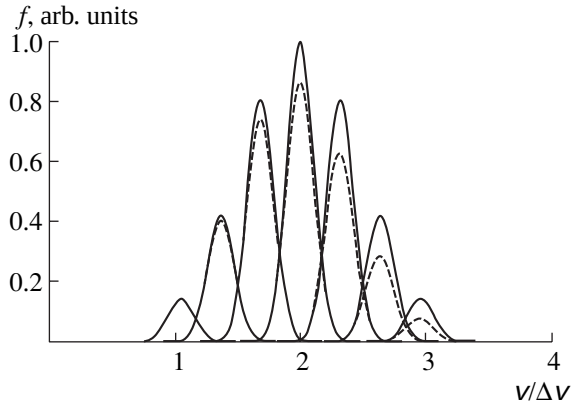

Fig. 2. Distribution functions of the preaccelerated electrons, calculated at the time $t = 50t_0$ for $v_0 \approx 2\Delta v$ and $BWt_0/\Delta v^3 \sim 10^{-12}$ and for different distances from the heating region (from $50\Delta v t_0$ to $175\ \Delta v t_0$) in the cases of free expansion (solid curves) and developed plasma turbulence (dashed curves).

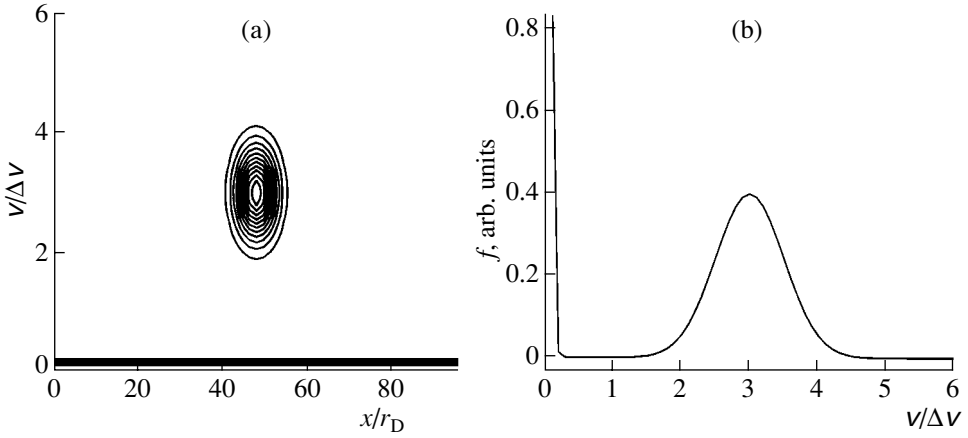

Fig. 3. (a) Contours of the initial distribution functions of the beam electrons and the electrons of the background plasma and (b) their cross section along the line passing through the peak in the distribution function of the beam electrons.

electrons can be represented as

$$f_0(x, v, t) = A\exp\left[-\frac{(x-vt)^2}{(\Delta v)^2 t_0^2} - \frac{(v-v_0)^2}{(\Delta v)^2}\right],$$

where v_0 is the electron velocity at which the electron density is maximum. In turn, under the same assumptions, the perturbed electron distribution function has the form

$$F(v, x, t) = A\exp\left[-\frac{(x-vt)^2}{(\Delta v)^2 t_0^2} - \frac{(v-v_0)^2}{(\Delta v)^2}\right] \times\left\{1 + \frac{2BW}{(\Delta v)^2 t_0^2 v}\left[\frac{t^3}{6} - \frac{xt^2}{2v} - \frac{v_0}{v}t_0^2 t + \frac{2}{(\Delta v)^2 t_0^2}\left[(vt-x)^2\frac{t^3}{3} + (vt-x)(v-v_0)t_0^2 t^2 + (v-v_0)^2 t_0^4 t\right]\right]\right\}. \quad (3)$$

Figure 2 shows the electron distribution functions calculated by formula (3) at different distances from the heating region at a fixed time for two cases: (i) free expansion and (ii) developed plasma turbulence. It can be seen that the shape of the distribution function of fast electrons again changes to a larger extent.

Of course, the above solutions do not cover the overall relaxation process; this can only be done by taking into account the effect of the evolution of the electron distribution function on the spectrum of the plasma waves, i.e., by solving a self-consistent problem (see below). Nevertheless, the above approximate analysis leads to the conclusion that the quasilinear relaxation of an electron beam formed as a result of rapid local energy deposition differs considerably from the relaxation of a spatially uniform electron beam [1, 2].

3. NUMERICAL SIMULATIONS

The conclusion derived from an approximate analysis is confirmed by numerical simulations. We numerically solved the following one-dimensional set of equations describing the interaction of a spatially localized electron beam with the plasma waves that it itself generates [2]:

$$\frac{\partial f}{\partial t} + v\frac{\partial f}{\partial x} = \frac{\partial}{\partial v}\left(D\frac{\partial f}{\partial v}\right), \quad D = \frac{8\pi^2 e^2}{m^2}\frac{W}{v},$$

$$\frac{\partial W}{\partial t} = 2\gamma W, \quad \gamma = \frac{\pi}{2}\frac{\omega_{pe}}{n_0}v^2\frac{\partial f}{\partial v},$$

where W is the spectral energy density of the plasma waves, D is the electron diffusion coefficient in velocity space, γ is the growth rate of the waves, n_0 is the plasma density, and ω_{pe} is the electron plasma frequency.

The simulations were carried out using the method of separating the physical processes [9]. We rewrite the basic set of equations in dimensionless variables in the form

$$\frac{\partial f}{\partial \bar{t}} + \bar{v}\frac{\partial f}{\partial \bar{x}} = 0,$$
$$\frac{\partial f}{\partial \bar{t}} = \frac{\partial}{\partial \bar{v}}\frac{\bar{\omega}}{|\bar{v}|}\frac{\partial f}{\partial \bar{v}}, \quad (4)$$
$$\frac{\partial \bar{\omega}}{\partial \bar{t}} = \bar{\omega}\bar{v}^2\frac{\partial f}{\partial \bar{v}},$$

where $f = \pi(\Delta v)f_0/n_b$, $\bar{\omega} = \pi W\omega_{pe}/n_b m(\Delta v)^3$, $\bar{t} = \omega_{pe}(n_b/n_0)t$, $\bar{v} = v/\Delta v$, f_0 is the sum of the distribution functions of the beam electrons and the electrons of the background plasma, n_b is the beam density, and Δv is

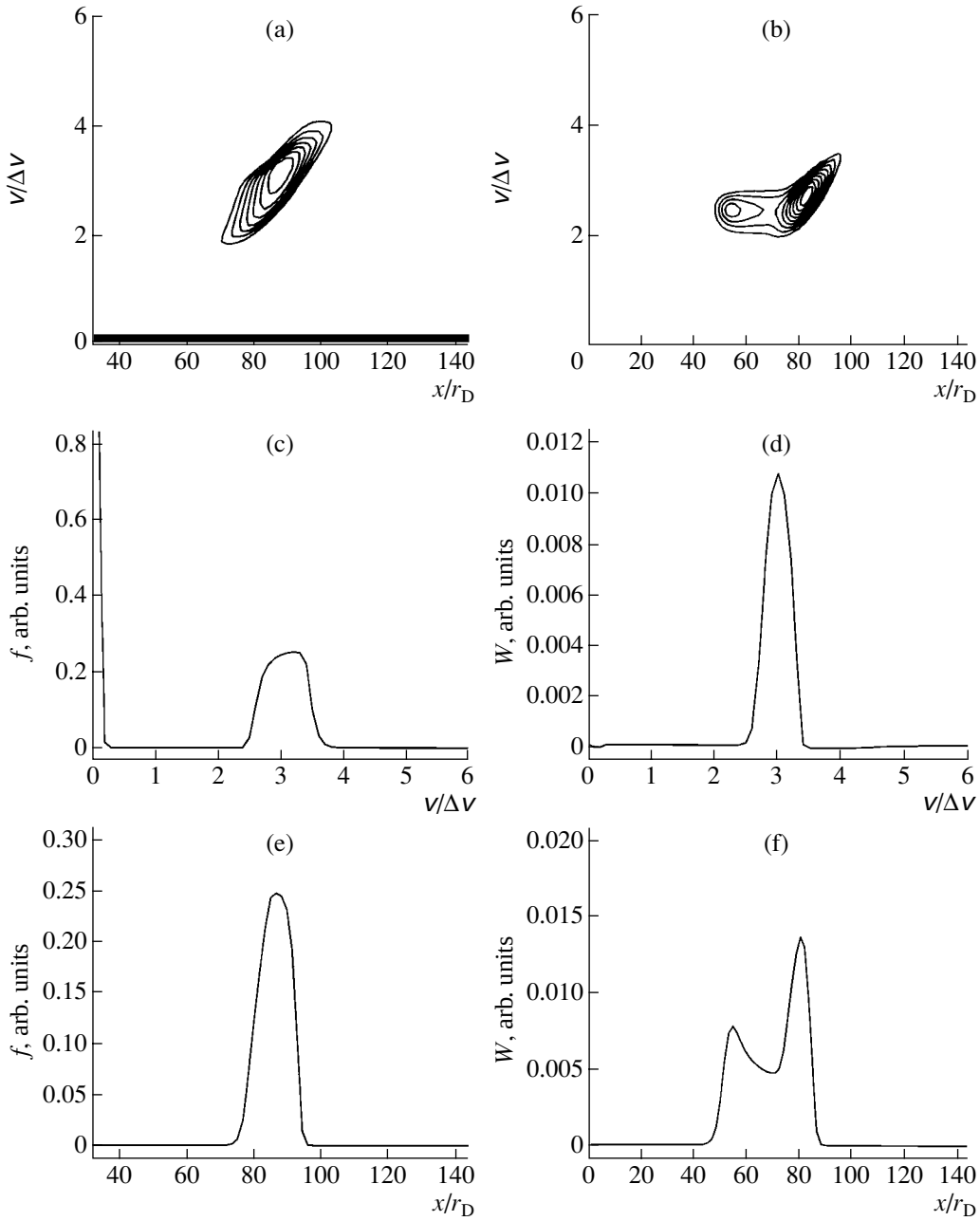

Fig. 4. (a) Contours of the distribution functions of the beam electrons and the electrons of the background plasma at the time $t = 12.65/f_{pe}$ and their cross sections along the lines passing through the peaks in the distribution function of the beam electrons (c) in velocity space and (e) in coordinate space; (b) contours of the spectral energy density of the plasma turbulence and its cross sections along the lines (d) $x = 80r_D$ and (f) $v = 2.5\Delta v$.

the initial thermal spread of the beam. The initial distribution functions of the beam electrons and the electrons of the background plasma in coordinate and velocity spaces are assumed to be Maxwellian. The first of Eqs. (4) describes the kinematics of the electrons flying apart in space, and the second one describes electron diffusion in velocity space under the action of plasma waves. The first of Eqs. (4) was solved in the first half of each time step, and the second equation was solved in the remaining half. At each time step, the solution to the first equation gives the change in the distribution function of the electrons due to their spatial expansion, and the solution to the second equation gives the change in the distribution function due to diffusion in velocity space.

The transport equation, i.e., the first of Eqs. (4), was solved by means of a one-dimensional monotonic scheme with a SUPERBEE limiting procedure [10]. The diffusion equation was solved by the sweep method [11]. The spatial step was $1.6r_D$, where r_D is the

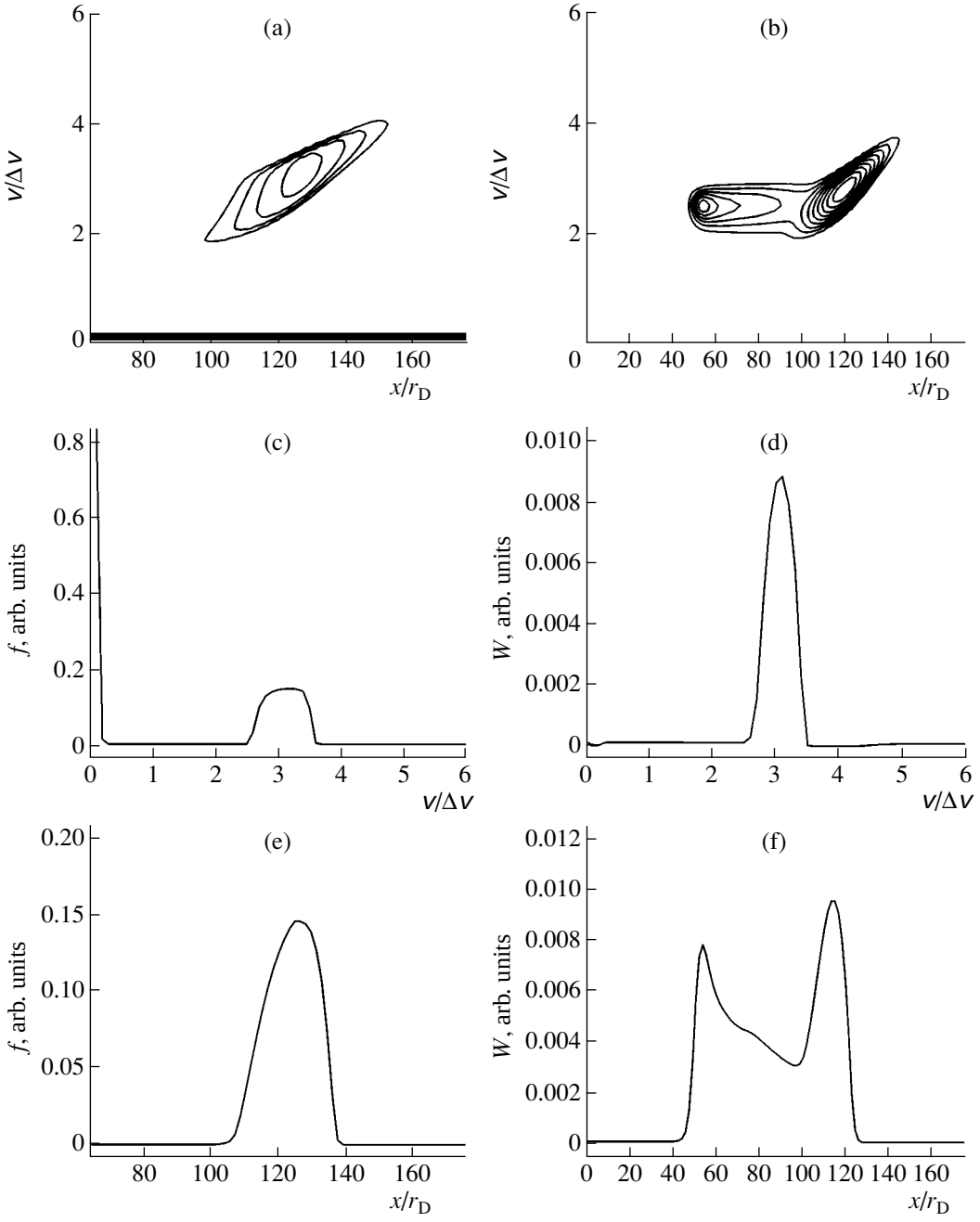

Fig. 5. Same as in Fig. 4, but for $t = 25.3/f_{pe}$ and $x = 110r_D$.

Debye radius. The ratio of the electron temperature in the background plasma to the beam temperature was 1 : 10, and the related density ratio was 10 : 1. The normalized initial energy spectrum of the plasma turbulence was assumed to be uniform, with the spectral density $\bar{\omega} = 10^{-3}$. The results of simulations are illustrated in Figs. 3–6. We can see that the relaxation of an electron beam is governed primarily by the kinematic effect of the spatial expansion of electrons. This effect manifests itself as a decrease in the beam density with time. On the other hand, the velocity spread of the beam changes to a smaller extent. The distribution function of the beam electrons changes to a much larger extent—its top becomes flatter, acquiring the shape of a local plateau. The formation of the plateau at the top of the distribution function is attributed to the fact that the spectral energy density of the plasma waves is maximum around the top; as a result, the electron diffusion in velocity space is most intense at the top. This indicates that plasma waves excited at the given spatial point grow until the slow electrons that come to this point cause them to be displaced into the local plateau region, where the growth rate nearly vanishes and the plasma

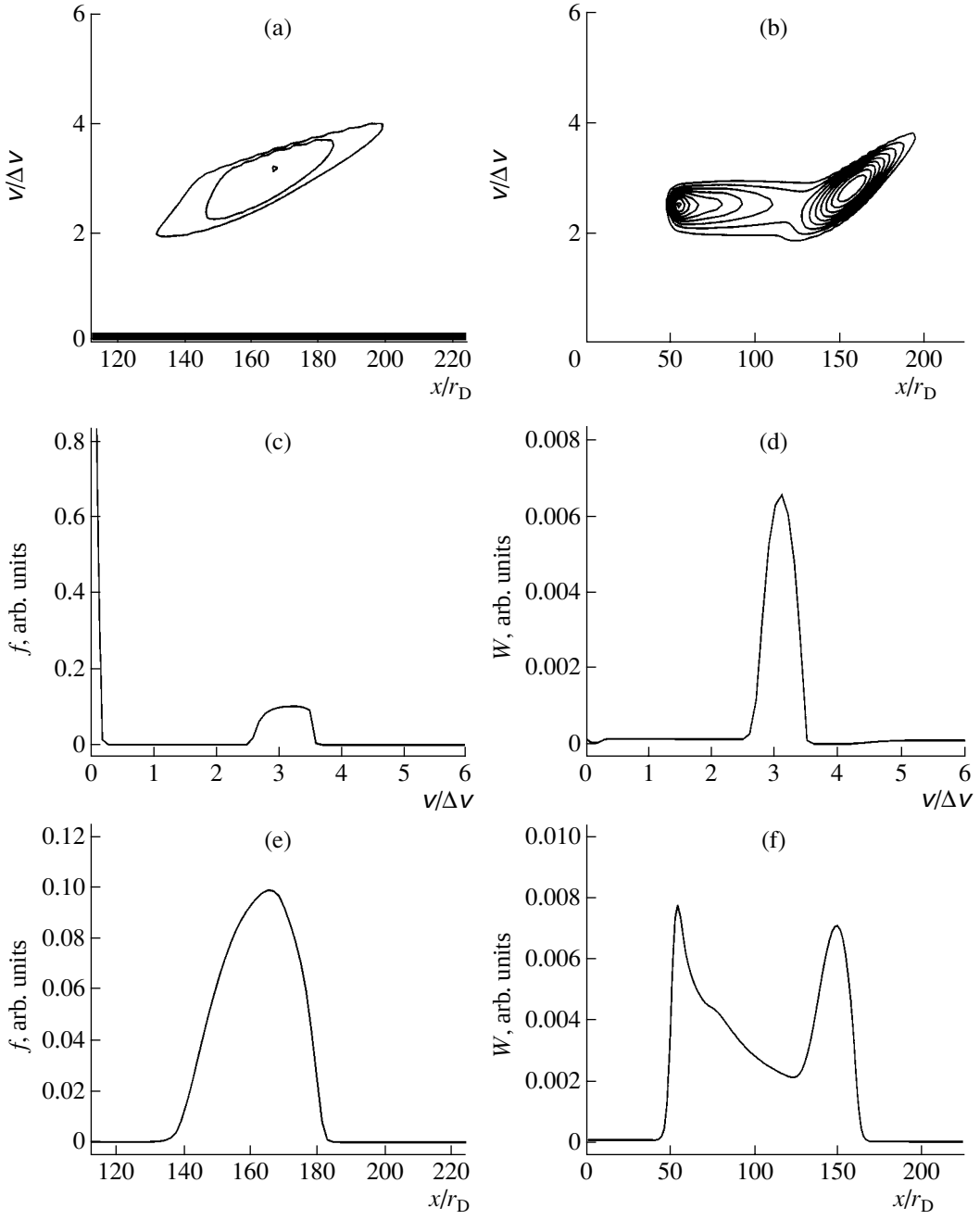

Fig. 6. Same as in Fig. 4, but for $t = 38/f_{pe}$ and $x = 160r_D$.

turbulence is maintained at a certain quasi-steady level. Then the waves occur at the negative slope of the distribution function, where they dampen. Consequently, this relaxation stage is governed by the balance between the width and the steepness of the portion of the distribution function over which the waves grow and by the spectral energy density of the plasma turbulence. In turn, the width and the steepness of this portion are determined by the effects of electron diffusion in velocity space and the expansion of the electrons in configuration space. Numerical simulations show that this relaxation stage occurs over a wide range of electron beam densities. As time elapses, the beam density decreases and the spectral energy density of the turbulence also becomes lower. As may be seen in Figs. 3a, 4a, 5a, 6a, most of the beam electrons are displaced toward the trailing edge of the beam because they expend their energy to generate plasma turbulence. One can also see a slight increase in the electron velocity spread at the trailing edge of the beam, while the spread at the beam's leading edge is seen to decrease. The beam electrons at the peak in their spatial density dis-

tribution propagate with a constant velocity. The peak in the spectral energy density of the turbulence is also displaced at a nearly constant speed. We can thus conclude that the results of our numerical simulations agree with the data from observations of type-III solar radio bursts, whose driving source moves with a constant velocity. The simulations also show that there is another peak in the spectral energy density of the plasma turbulence. This peak, which was not displaced in the course of a run, is associated with weakly damped oscillations generated at the very beginning of the relaxation process.

4. CONCLUSION

The initial stage of the one-dimensional relaxation of an electron beam under the action of plasma turbulence with a broad spectrum has been analyzed by perturbatively solving the kinetic equation. The beam is formed due to rapid local heating, and the initial condition correspond to free spatial expansion of the beam electrons. The analysis shows that the combined action of the kinematic effect of the spatial expansion of electrons with different velocities and the effect of electron diffusion in velocity space under the action of plasma turbulence leads to an increase in the velocity spread of the local electron beams that are formed at each point in space.

The further relaxation process has been simulated numerically by solving a self-consistent set of the quasilinear equations describing electron diffusion in velocity space under the action of plasma waves and the excitation of plasma waves by the electrons whose distribution function changes in both space and time. The results of simulations show that diffusion results in the formation of a plateau at the top of a local distribution function. At the same time, the velocity spread of each local beam changes insignificantly. As for the relaxation process, it proceeds primarily through the spatial expansion of electrons with different velocities.

ACKNOWLEDGMENTS

This study was supported by the Russian Foundation for Basic Research, project no. 00-02-16819.

REFERENCES

1. *Plasma Electrodynamics*, Ed. by A. I. Akhiezer *et al.* (Nauka, Moscow, 1974; Pergamon, Oxford, 1975).
2. A. A. Vedenov and D. D. Ryutov, in *Reviews of Plasma Physics*, Ed. by M. A. Leontovich (Atomizdat, Moscow, 1972; Consultants Bureau, New York, 1975), Vol. 6.
3. S. M. Levitskiĭ and I. P. Shashurin, Zh. Éksp. Teor. Fiz. **52**, 350 (1967) [Sov. Phys. JETP **25**, 227 (1967)].
4. R. S. Churaev and A. V. Agapov, Fiz. Plazmy **6**, 422 (1980) [Sov. J. Plasma Phys. **6**, 232 (1980)].
5. V. V. Zheleznyakov, *Radioemission of the Sun and the Earth* (Nauka, Moscow, 1964).
6. V. V. Zheleznyakov and V. V. Zaitsev, Astron. Zh. **47**, 60 (1970) [Sov. Astron. **14**, 47 (1970)].
7. V. G. Ledenev, Sol. Phys. **149**, 279 (1994).
8. A. B. Mikhailovskii, *Theory of Plasma Instabilities* (Atomizdat, Moscow, 1975; Consultants Bureau, New York, 1974).
9. G. I. Marchuk, *Splitting Methods* (Nauka, Moscow, 1988).
10. G. S. Rivin and P. V. Voronina, Opt. Atmos. Okeana **10**, 6 (1997).
11. A. N. Tikhonov and A. A. Samarskii, *Equations of Mathematical Physics* (Nauka, Moscow, 1972; Pergamon Press, Oxford, 1964).

Translated by O.E. Khadin

Plasma Physics Reports, Vol. 29, No. 4, 2003, pp. 307–327. Translated from Fizika Plazmy, Vol. 29, No. 4, 2003, pp. 336–356.

NONLINEAR PHENOMENA

Effect of the Ponderomotive Force on the Development of Beam–Plasma Instability

Yu. P. Bliokh*, M. G. Lyubarsky, N. M. Zemlyansky***, V. I. Mirny***, V. O. Podobinsky***, G. V. Sotnikov***, and Ya. B. Fainberg*****

**Physics Department, Technion, Haifa, Israel*

***Karazin National University, pl. Svobody 4, Kharkov, 61077 Ukraine*

****Institute of Plasma Electronics and New Acceleration Methods, National Science Center Kharkov Institute of Physics and Technology, ul. Akademicheskaya 1, Kharkov, 61108 Ukraine*

Received September 12, 2002; in final form, October 24, 2002

Abstract—The amplitude of the wave generated in a plasma during the development of beam–plasma instability is nonuniform in the longitudinal direction. The ponderomotive force associated with this nonuniformity leads to a redistribution of the plasma density; as a result, the wave amplitude and its spatial distribution change. As the beam current grows, the ponderomotive force plays an increasingly important role and radically changes the mechanism by which the beam–plasma instability saturates. Ion acoustic waves generated by the ponderomotive force propagate in the direction opposite to the propagation direction of the beam, thereby ensuring distributed feedback and giving rise to a strong low-frequency self-modulation of the wave amplitude and phase. Results are presented from experimental investigations of the self-modulation regime of the beam–plasma instability in a magnetized plasma waveguide. Theoretical estimates of the parameters of the low-frequency self-modulation agree well with the experimental data. © *2003 MAIK "Nauka/Interperiodica"*.

1. INTRODUCTION

One of the areas of study in plasma electronics is the generation and amplification of high-power microwave radiation in plasma-filled electrodynamic structures. Considerable progress in this direction made it possible to create high-power microwave sources operating in both pulsed (sources based on relativistic electron beams) [1–3] and continuous (sources based on nonrelativistic electron beams) modes [4, 5].

Numerous experimental and theoretical results obtained for more than 50 years of active research in plasma electronics have provided a fairly clear insight into the physics of the processes occurring in the interaction of charged-particle beams with plasmas. However, in our opinion, there remains an important aspect of this interaction that has been studied insufficiently as yet, specifically, the interrelation between the conditions for the generation of microwave fields by the beams in a plasma and the plasma parameters.

Each of these two effects—(i) the influence of the plasma parameters (such as density, temperature, and spatial inhomogeneity) on the conditions for the generation of microwave fields by charged-particle beams and (ii) changes in the parameters of the plasma under the action of microwave radiation propagating in it—is well known and, on the whole, has been investigated in great detail. However, to the best of our knowledge, their combined action on the development of the beam–plasma instability (BPI) and, especially, on the evolution of a beam–plasma discharge (BPD), has not been studied systematically, although the role of this interrelation may be very important.

As an example of the combined action of these two effects, we consider a possible scenario of the development of the instability of a beam injected into an initially homogeneous plasma. After the transient processes in the plasma have come to an end, the amplitude of the excited wave relaxes to a steady-state longitudinally nonuniform distribution. Because of the nonuniformity of the microwave field amplitude, the plasma density also becomes nonuniform. This nonuniformity may be produced either by the microwave ponderomotive force that expels the plasma from the region of strong microwave field or by the microwave discharge that is initiated in the region where the amplitudes of the microwave oscillations are sufficiently large. The low-frequency (ion acoustic or magnetosonic) waves of the density of the plasma expelled by the microwave ponderomotive force or the plasma additionally produced by a microwave discharge propagate away from the source of perturbation. The BPI, which originally gave rise to nonuniformity, now develops in an inhomogeneous plasma and acts to change the amplitude of the wave generated by the beam and redistribute the wave amplitude in space. Accordingly, the plasma density continues to be nonuniform, but for another reason: the plasma and the fields generated by the beam are set into self-consistent motion. As a result, a inhomogeneous plasma evolves into a new steady state or into a self-modulation interaction regime. In both cases, the

1063-780X/03/2904-0307$24.00

amplitudes of the beam-generated waves and their spectrum can differ strongly from those in a homogeneous plasma.

The changes in the parameters of a medium under the action of radiation propagating in it constitute the material of nonlinear optics. In the above example, the medium (plasma) also changes its properties (density) under the action of microwave radiation. However, the radical difference between the problem at hand and the problems that are the subject of nonlinear optics is in the change of the properties of the medium that affect the *generation* of radiation. Because of the resonant nature of the wave generation, the characteristic that is most sensitive to variations in the parameters of the medium in the beam–plasma interaction is the efficiency with which the wave is generated.

The above example of the plasma nonlinearity illustrates a new effect peculiar to the BPI—distributed delayed feedback, which transforms the system under consideration into an oscillator. In fact, the plasma density perturbations excited in the region of maximum microwave field move in the propagation direction of the beam and in the opposite direction and affect the conditions for the generation of microwaves, thereby changing the microwave field amplitude in the region where the perturbations are excited. The system "remembers" these plasma density perturbations until they escape from the interaction region.

Our paper is organized as follows. In Sections 2–4, a mathematical model of a magnetized plasma-filled traveling-wave tube (TWT) amplifier is constructed with allowance for the plasma nonlinearity produced by the microwave ponderomotive force and is then used to study the effect of this force on the amplitude of the microwave generated by an electron beam in a steady-state operating mode of the amplifier. In Section 5, results are presented of theoretical and experimental investigations of the dynamic regimes of the BPI (the thresholds for the onset of low-frequency self-modulation, as well as the spectral and power parameters) that arise as a result of the generation of ion acoustic waves by the microwave ponderomotive force in a magnetized plasma waveguide.

We restrict ourselves to considering only nonrelativistic devices based on the Cherenkov interaction between waves and charged particles. However, since the effects to be examined are associated with the influence of the plasma nonlinearity on the resonant properties of the wave–particle interaction, the study can be extended to include systems with relativistic electron beams and systems based on some other elementary resonance effects (such as normal and anomalous Doppler effects).

2. EVALUATION OF THE EFFECT OF THE MICROWAVE PONDEROMOTIVE FORCE ON THE DEVELOPMENT OF THE BPI

The experimental data reported in [6–8] and the analyses carried out therein show that, as the beam current or the plasma density grows, the plasma nonlinearity plays an increasingly important role in the dynamics of the BPI and that the nonlinearity originally arises in response to microwave ponderomotive forces. That is why we restrict ourselves to considering the effect of the microwave ponderomotive force as a mechanism ensuring the interrelation between the parameters of the plasma and of the microwaves generated in it. In addition, we are interested exclusively in one-dimensional (longitudinal) plasma motions, assuming that the guiding external magnetic field is strong enough for the transverse motions to be neglected.

In this section, we present preliminary estimates that make it possible to determine the ranges of the plasma and electron-beam parameters in which the plasma density perturbations produced by the microwave ponderomotive force have an important effect on the conditions for microwave generation.

A charged-particle beam can excite the eigenmodes of an electrodynamic system if the velocity v_b of the beam particles is close to the phase velocity v_{ph} of the eigenmodes:

$$\frac{|v_b - v_{ph}|}{v_b} < \frac{\delta k}{k}, \tag{1}$$

where δk is the instability growth rate and k is the wave vector of a synchronous wave.

The wave generated during the BPI grows in the direction of the beam propagation. The microwave ponderomotive force associated with the longitudinal nonuniformity of the wave field deforms the plasma density profile. This force is exerted on a slowly moving charged particle by a spatially nonuniform microwave field [9]. The motion of a particle in such a field is the superposition of its fast oscillations and slow regular drift. In turn, the particle drifts as if it were affected by the force

$$\mathbf{F} = -\nabla\left(\frac{e^2 E_0^2}{4m\omega^2}\right);$$

where E_0 is the electric field amplitude, ω is the oscillation frequency, and e and m are the charge and mass of an electron.

Since the microwave ponderomotive force F is inversely proportional to the mass of a particle, it acts primarily on the lightest plasma particles—electrons. The electrons moving relative to the ions give rise to the charge separation (polarization) electric field, which makes the independent motion of the electrons and ions impossible. Consequently, the microwave ponderomotive force F sets each of the charged plasma compo-

nents into common motion, thereby expelling the plasma from the region of stronger microwave electric field.

The density n_p of the plasma is one of the most important parameters determining the properties of the waves propagating in it. In particular, the phase velocity v_{ph} of a wave with a fixed frequency ω is a function of the plasma density, $v_{ph} = v_{ph}(n_p)$. In a plasma with a nonuniform density $n_p(x)$, the wave phase velocity is coordinate dependent, $v_{ph} = v_{ph}(x)$. As a result, synchronization condition (1) fails to hold over the entire length of the beam–wave interaction region and is only satisfied along the parts over which $v_{ph} \simeq v_b$. Since the width $\frac{\delta k}{k} v_b$ of a resonance in the phase velocity is, as a rule, small in comparison with v_b, the BPI is very sensitive to the degree of plasma inhomogeneity. The plasma density perturbation δn_p caused by the nonuniformity of the amplitude of the excited wave is determined by the condition that the microwave ponderomotive force is equal to the force of the excess pressure:

$$\nabla\left(\frac{e^2E_0^2}{4m\omega^2}\right) = \nabla\delta n_p\frac{T_e}{n_p}, \tag{2}$$

which yields

$$\delta n_p \simeq n_p\frac{e^2E_0^2}{4m\omega^2T_e}; \tag{3}$$

where T_e is the plasma electron temperature.

The change in the wave phase velocity, $\delta v_{ph} = \delta n_p\frac{\partial v_{ph}}{\partial n_p}$, that results from this perturbation can significantly influence the development of the instability when

$$\delta v_{ph} = v_b\frac{\delta k}{k}. \tag{4}$$

Conditions (3) and (4) imply that the deformation of the plasma density profile under the action of the microwave ponderomotive force of the excited wave can have a strong impact on the development of the BPI if the wave amplitude E_0 is sufficiently large:

$$\frac{E_0^2}{4\pi} \sim \frac{\omega^2}{\omega_p^2}T_e v_b\frac{\delta k}{k}\left(\frac{\partial v_{ph}}{\partial n_p}\right)^{-1}, \tag{5}$$

where $\omega_p = \sqrt{\frac{4\pi e^2 n_p}{m}}$ is the electron plasma frequency.

The maximum amplitude E_m of the wave generated during the BPI is determined by the condition

$$\frac{E_m^2}{4\pi}\left(\omega\frac{\partial D}{\partial\omega}\right)v_g \sim \frac{\delta k}{k}n_b m v_b^3, \tag{6}$$

where n_b is the beam density, v_g is the wave group velocity, and $D(\omega, k, \omega_p)$ is a function whose zeros determine the dispersion of the eigenmodes of the system. The left-hand side of condition (6) is the density of the energy flux through the waveguide cross section in terms of the amplitude of the longitudinal component of the electric field in the region occupied by the plasma.

According to conditions (5) and (6), the microwave ponderomotive force can significantly change the parameters of the BPI if the parameter

$$\Lambda_0 = \frac{n_b m v_b^2}{T_e v_g}\frac{\omega_p^2}{\omega^2}\frac{\partial v_{ph}}{\partial n_p}\left(\omega\frac{\partial D}{\partial\omega}\right)^{-1}$$

is sufficiently large,

$$\Lambda_0 > 1. \tag{7}$$

Since the quantities $\partial v_{ph}/\partial n_p$ and $\partial D/\partial\omega$ are functions of the parameters of the waveguide structure (plasma density, plasma temperature, external magnetic field, geometric dimensions, etc.), specific conditions on the beam current and energy under which the microwave ponderomotive force play an important role can be obtained only for particular waveguides. As an example, we turn to the experimental investigations carried out in [6–8] and consider a plasma waveguide in a strong longitudinal magnetic field and a hybrid slow-wave structure partially filled with plasma.

2.1. Magnetized Plasma Waveguide

In this case, the function D coincides with the dielectric function for slow potential waves and has the form

$$D(\omega, k; \omega_p) = 1 - \frac{\omega_p^2}{\omega^2} + \frac{k_\perp^2}{k^2},$$

where $k_\perp \sim 1/R$ is the transverse vector of the wave in a waveguide of radius R.

Using the dispersion relation $D(\omega, k, \omega_p) = 0$, we calculate the group velocity of the wave and its phase velocity as functions of the plasma density in order to write condition (7) in the form

$$\frac{n_b}{n_p}\left(\frac{eU_b}{T_e}\right) > 10\frac{k_\perp^4}{(k^2 + k_\perp^2)^2} \simeq 10. \tag{8}$$

In deriving this condition, we assumed that the transverse and longitudinal components of the wave vector are of the same order of magnitude. Such a relation is

optimum for microwave generation because, at $k \ll k_\perp$, the growth rate of the BPI is slow and, at $k \gg k_\perp$, the excited wave is weakly coupled to the external waveguide.

The parameters of the device with which the experiments described in Section 5 were carried out ($U_b \sim$ 1 kV, $T_e \sim 3$ eV, and $n_p \sim 10^9$ cm^{-3}, the cross-sectional area of the beam being 3 cm^2) can be substituted into condition (8) to yield the following condition on the beam current at which the microwave ponderomotive forces are anticipated to have a significant effect: $I_b >$ 20 mA. In those experiments, the beam current was as high as several tens of milliamperes. Hence, even the above formulas, serving merely as estimates, imply that the results of measurements should be interpreted with allowance for the changes in the plasma density under the action of microwave radiation.

2.2. Hybrid Slow-Wave Structure

Such low beam currents at which the plasma density profile in a magnetized plasma waveguide is significantly deformed can be explained by the high sensitivity of the wave phase velocity to variations in the plasma density. In the hybrid slow-wave structure with which the experiments described in [6–8] were carried out, the plasma occupied no more than 10% of the entire volume and had a lesser impact on the dispersion properties of the eigenmodes in comparison with a magnetized plasma waveguide. In addition, for such a structure, the parameter $\omega\partial D/\partial\omega$ in condition (7) is large, because nearly all of the power flows through the coupling slits of the cavities and the longitudinal field in the plasma is much weaker than the field in the cavities. For an arbitrary waveguide structure in which the volume occupied by the plasma is relatively small, the quantity $\omega\partial D/\partial\omega$ was rigorously calculated in [10, 11]. Here, we present only the final result of calculations for the hybrid structure described in [6, 7]: for an optimum plasma density such that $\omega_p \sim \omega$, the microwave ponderomotive force effects should be significant at a beam current of about 3 A, which corresponds to a generated microwave power of about 20 kW.

At this point, it is pertinent to recall that all of the above conditions are merely estimates and should not be thought of a strict sense.

3. BASIC EQUATIONS

We begin with a number of simplifying assumptions, with which the mathematical model becomes more illustrative and the problem of the self-consistent dynamics of the plasma and microwave can be investigated in its pure form, i.e., without reference to the effects that are unimportant for our purposes.

We consider the hierarchy of the time scales characteristic of the problem. The shortest time scale is the period T_1 of microwave oscillations generated by the beam. If the growth rate of the BPI is small, i.e., inequality $\delta k \ll k$ is satisfied, then the behavior of the generated wave can be described by the reduced equations for the complex wave amplitude and the processes occurring on this time scale can be excluded from consideration.

The longer time scales $T_2 = L\dfrac{|v_b - v_{ph}|}{v_b v_{ph}}$ and $T_3 = L/v_g$ are associated with the finite length of the system (see, e.g., [12]). The first of these two scales is the shortest time scale on which the wave amplitude varies at the exit from the system (an oscillator or an amplifier). The second is the time during which the steady operating mode of an amplifier—a system without high-frequency feedback—is achieved. In the presence of external or internal high-frequency feedback, it is necessary to take into account the fourth characteristic time scale, namely, the time T_4 required for a microwave signal to pass through the feedback circuit.

The times T_1, T_2, T_3, and T_4 satisfy the following inequalities, which may turn out to be strong:

$$T_4 > T_3 > T_2 \gg T_1.$$

The time scales just introduced are characteristic of vacuum microwave devices based on the Cherenkov interaction between a charged-particle beam and slow waves. In a plasma waveguide or in a plasma-filled slow-wave structure, there is an additional characteristic time scale—the propagation time T_5 of the plasma density perturbations, i.e., the time required for a low-frequency (ion acoustic, magnetosonic, etc.) plasma wave to pass through the volume occupied by the plasma. This may be the time of the propagation of perturbations in either the longitudinal or transverse direction, depending on the strength of the guiding magnetic field and the ratio between the longitudinal and transverse gradients of the amplitude of the microwaves. Because of the large difference in the longitudinal and transverse dimensions of the plasma (in experimental devices, the plasma length is, as a rule, several tens of centimeters, and the transverse dimensions are no larger than several centimeters) and in the propagation velocities of the perturbations (from about 10^6 cm/s for ion acoustic waves to about 10^8 cm/s for magnetosonic waves), the relationships among the time scales T_2, T_3, T_4, and T_5 may be very different. The simplest two are the limiting cases $T_5 \ll T_2$ and $T_5 \gg T_4$. The first case was considered in [13, 14] in studying the effect of transverse magnetosonic plasma oscillations generated by the microwave ponderomotive forces of the excited wave on the operation of a TWT oscillator with delayed feedback. The inequality $T_5 \ll T_2$ makes it possible to analytically relate the instantaneous amplitude of the microwave to that of the plasma density perturbation and thereby eliminate the perturbation from consideration.

The second case requires further simplification because the inequality $T_5 \gg T_4$ does not allow us to determine which of the possible two factors—high-frequency feedback or plasma motion—will lead to the onset of unsteady regimes. That is why, in order to single out the effects associated exclusively with the plasma motion, we restrict our analysis to an amplifier—a system without high-frequency feedback. In this case, the time scale T_4 drops out of the equations of the problem and the inequality $T_5 \gg T_3$ makes it possible to neglect transient processes occurring on the time scales T_3 and T_2 and describe the instantaneous longitudinal profile of the amplitude of the microwave by the steady-state distribution corresponding to a given longitudinal profile of the plasma density.

We assume that the guiding magnetic field is strong enough for the radial motions of the beam and plasma particles to be neglected. Under this assumption, the time scale T_5 is the time required for an ion acoustic wave to pass along the system, and the condition $T_5 \gg T_3$ is equivalent to the inequality

$$v_g \gg c_s, \tag{9}$$

where $c_s = \sqrt{T_e/M}$ is the ion acoustic velocity and M is the mass of the a plasma ion. Under the conditions of the most practical interest for microwave electronics, we have $v_b \simeq v_{ph} \sim v_g \sim 10^9$–$10^{10}$ cm/s $\gg c_s \sim 10^6$–10^7 cm/s; i.e., inequality (9) is satisfied by a large margin.

Recall that, because of its resonant nature, the BPI is very sensitive to the degree of plasma inhomogeneity. Consequently, we can work under the condition

$$\delta n_p/n_p \ll 1 \tag{10}$$

and describe plasma motions in the linear approximation.

Because of the transverse nonuniformity of the field of the excited wave, the longitudinal motions of the beam particles at different radii are different [15]. In order for this effect to also be excluded from consideration, we assume that the cross-sectional area S_b of the beam is much smaller than the cross-sectional area S_p of the plasma. Under this assumption, the radial nonuniformity of the amplitude of the microwave oscillations in the axial region can be neglected.

Now, we turn to the construction of a mathematical model. Using inequality $\delta k \ll k$, which indicates that the growth rate of the BPI is small, we can represent the longitudinal component of the electric field of the excited wave as

$$E(\mathbf{r}, z, t) = E_0(z, t)G(\mathbf{r})\exp(ik_0 - i\omega_0 t) + \text{c.c.}; \tag{11}$$

where $E_0(z, t)$ is the slowly varying complex amplitude, the function $G(\mathbf{r})$ describes the dependence of the field of the eigenmode of the structure on the radial coordinate $\mathbf{r}$, and the frequency of the wave and its vector are related by the resonance condition $\omega_0 = k_0 v_b$.

The longitudinal profile of the amplitude of the wave generated by the beam is determined by solving the time-independent equations for the BPI,

$$\frac{\partial \varepsilon}{\partial \zeta} + i\frac{k_0 - k(\zeta, \tau)}{\delta k_0}\varepsilon = -\frac{1}{2\pi}\int_0^{2\pi} e^{-i\varphi(\varphi_0, \zeta)}d\varphi_0,$$
$$\frac{\partial^2 \varphi}{\partial \zeta^2} = \text{Re}(\varepsilon e^{i\varphi}), \tag{12}$$

where $\zeta = \delta k_0 z$ is the dimensionless longitudinal coordinate, $\varepsilon = \dfrac{ek_0 E_0 G(0)}{m v_b^2 \delta k_0^2}$ is the dimensionless wave amplitude, $\varphi = \omega(z/v_b - t)$ is the phase of the beam particles in the wave, φ_0 is the initial phase in the plane of beam injection $z = 0$, and

$$\delta k_0 = k_0\left(\frac{\omega_b^2 G^2(0)\left(S_b \Big/ \int\limits_{S_w} G^2 ds\right)}{\omega^2 k_0(\partial D/\partial k_0)}\right)^{1/3}$$

is the spatial growth rate of the BPI in a homogeneous plasma. The integral of the function G^2 is taken over the cross-sectional area S_w of the waveguide structure. By virtue of the above assumption that the beam radius is small, the integral over the cross-sectional area of the beam in the definition of the growth rate is replaced with the quantity $G^2(0)S_b$. The local value of the wave vector $k(\zeta, \tau)$ of the eigenmode of the slow-wave structure is the solution to the dispersion relation $D[\omega, k(\zeta, \tau), \omega_p(\zeta, \tau)] = 0$. Since high-frequency feedback is absent and inequality (9) is satisfied, we can describe the BPI by the above time-independent equations, in which case the unsteady nature of the plasma in the structure can be accounted for through the parametric dependence of the wave vector $k(\zeta, \tau)$ of the excited wave on the dimensionless time $\tau = \delta k_0 c_s t$. This choice of the dimensionless time is convenient for our purposes: we thus take into account both the spatial scale δk_0^{-1}, which characteristic of the BPI, and the rate c_s of variation in the plasma parameters.

In what follows, we assume that the electron beam amplifies the natural noise fluctuations rather than the external signal fed through the entrance plane of the system. If the interaction region is sufficiently long, the BPI, being resonant in nature, acts as a natural narrowband filter; moreover, the longer the system, the narrower the bandwidth of the filter [16]. Consequently, we can assume that, to zeroth order in the width of the amplification band, there is only a single wave in the system, specifically, the one that has the maximum gain. This assumption enables us to determine the frequency $\omega_0 = k_0 v_b$ and the wave vector k_0 from the

known instantaneous plasma density profile. In fact, the local instability growth rate $\mathrm{Re}(\delta k)$ near its maximum is a quadratic function of the instantaneous detuning $\nu(\zeta) = \dfrac{k_0 - k(\zeta)}{\delta k_0}$:

$$\mathrm{Re}[\delta k(\nu)] = \mathrm{Re}[\delta k(0)] - \frac{1}{2}\mathrm{Re}[\delta k''(0)]\nu^2.$$

The total amplification coefficient q is determined by the expression

$$q = \exp\left(\int_0^{\zeta_\nu} \mathrm{Re}\{\delta k[\nu(\zeta)]\}d\zeta\right),$$

where the integration interval is chosen so that, along its length ζ_ν, the detuning $\nu(\zeta)$ is small and the amplification coefficient q is large. Such a region always exist in the initial portion of a sufficiently long system, in which the microwave ponderomotive force is so weak that the plasma is practically homogeneous (however, as will be shown below, the plasma density in this portion differs from that in the absence of the microwave ponderomotive force).

We choose the value k_0 so that the amplification coefficient is maximum for a given dependence $k(\zeta)$. It is easy to see that the maximum is reached at

$$k_0 = \frac{1}{\zeta_\nu}\int_0^{\zeta_\nu} k(\zeta)d\zeta.$$

The calculations presented below were carried out precisely for this choice of the k_0 value.

Equations (12) should be supplemented with boundary conditions. We assume that the beam velocity and beam density at the entrance to the system ($\zeta = 0$) are constant and specify the initial field amplitude and phase as

$$\begin{aligned} &\varepsilon(0, \tau) = \varepsilon_0, \quad \varphi(0, \tau) = \varphi_0, \\ &\frac{\partial\varphi}{\partial\zeta}(0, \tau) = 0, \quad 0 \le \varphi_0 \le 2\pi. \end{aligned} \tag{13}$$

These conditions are sufficient to determine the field ε at any point of the system, provided that the longitudinal plasma density profile and, accordingly, the dependence $k(\zeta)$ are known.

In order for the set of Eqs. (12) and (13) to be closed, it is necessary to (i) determine the dependence of the wave vector k of the excited wave on the local plasma density n_p and (ii) derive dynamic equations describing how the plasma density changes under the action of the microwave ponderomotive force of the wave field. The dependence $k(n_p)$ is determined by solving the dispersion relation $D(\omega, k, \omega_p) = 0$ in which the field frequency ω is constant and the electron plasma frequency ω_p depends on the plasma density n_p integrated over the plasma cross section. In order to determine this dependence, we rewrite the dispersion relation in a form analogous to that used in [17]:

$$D \sim \langle G, \hat{D}G\rangle\langle G, G\rangle^{-1},$$

where the angular brackets indicate integration over the cross section of the structure. In the case at hand, $\hat{D}$ is a linear operator with which Maxwell's equations for longitudinal electric field (11) of constant amplitude are written as $\hat{D}G = 0$. In the operator $\hat{D}$ so defined, the plasma density contributes additively to the dielectric function, $\varepsilon(\omega) = 1 - \omega_p^2/\omega^2$; therefore, the plasma density enters the function D through the quantity $\langle G(\mathbf{r}), n_p(\mathbf{r}), G(\mathbf{r})\rangle$ and the dispersion relation can be rewritten in the form

$$D[\omega, k(\zeta, \tau), \bar{n}_p] = 0, \tag{14}$$

where the upper bar stands for the normalized averaging over the plasma cross section,

$$\bar{f} = \left(\int_{S_p} G^2 f\, ds\right)\left(\int_{S_p} G^2 ds\right)^{-1}.$$

We represent the wave vector and plasma density as $k(\zeta) = k^{(0)} + \Delta k(\zeta)$ and $n_p = n_0(\mathbf{r}) + \delta n_p(\mathbf{r}, \zeta, \tau)$, where $k^{(0)}$ is the solution to Eq. (14) with $\bar{n}_p = n_0$. Using the smallness of the plasma density perturbations, we expand the left-hand side of the dispersion relation in powers of the small parameter $\delta n_p/n_p \ll 1$. Taking into account the relationship

$$\frac{\partial v_{ph}}{\partial n_0} = \frac{v_{ph}^2}{\omega}\frac{\partial D}{\partial n_0}\left(\frac{\partial D}{\partial k^{(0)}}\right)^{-1},$$

we arrive at the following final relationship between the perturbations of the wave vector and plasma density:

$$\Delta k = -\frac{1}{2}\frac{\omega_p}{v_{ph}}\frac{\partial v_{ph}}{\partial\omega_p}k^{(0)}\frac{\delta\bar{n}_p}{n_0}.$$

With the representation $k_0 = \dfrac{1}{\zeta_\nu}\int_0^{\zeta_\nu} k(\zeta)d\zeta$ chosen above, the term $[k_0 - k(\zeta)]\delta k_0^{-1}$ takes the form

$$\begin{aligned} [k_0 - k(\zeta)]\delta k_0^{-1} &= \left(\frac{1}{\zeta_\nu}\int_0^{\zeta_\nu}\delta k(\zeta)d\zeta - \delta k(\zeta)\right)\delta k_0^{-1} \\ &= \frac{1}{2}\frac{\omega_p}{v_{ph}}\frac{\partial v_{ph}}{\partial\omega_p}\frac{k_0}{\delta k_0 n_0}\left(\delta\bar{n}_p(\zeta) - \frac{1}{\zeta_\nu}\int_0^{\zeta_\nu}\delta\bar{n}_p(\zeta)d\zeta\right) \\ &\equiv \eta(\zeta) - \frac{1}{\zeta_\nu}\int_0^{\zeta_\nu}\eta(\zeta)d\zeta, \end{aligned}$$

where we have introduced the function

$$\eta(\zeta, \tau) = \frac{k_0}{2\delta k_0}\frac{\omega_p}{v_{ph}}\frac{\partial v_{ph}}{\partial \omega_p}\frac{\delta \bar{n}_p(\zeta, \tau)}{n_0}.$$

Now, we can write Eqs. (12) in the final form:

$$\frac{\partial \varepsilon}{\partial \zeta} + i\left(\eta - \frac{1}{\zeta_v}\int_0^{\zeta_v}\eta d\zeta\right)\varepsilon = -\frac{1}{2\pi}\int_0^{2\pi} e^{-i\varphi(\varphi_0, \zeta)}d\varphi_0,$$
$$\frac{\partial^2 \varphi}{\partial \zeta^2} = \mathrm{Re}(\varepsilon e^{i\varphi}). \tag{15}$$

Further, we average the electron and ion continuity equations and the equation of motion of the electron and ion plasma components over the fast oscillations to obtain the following equation describing the slow motion of the plasma as a single entity:

$$\frac{\partial^2 \delta n_p}{\partial t^2} - c_s^2\frac{\partial^2 \delta n_p}{\partial z^2}$$
$$= \frac{e^2 n_0}{Mm\omega^2}G^2(\mathbf{r})\frac{\partial}{\partial z}\left[\frac{\partial |E_0|^2}{\partial z} - \frac{2}{v_{ph}}\frac{\partial |E_0|^2}{\partial t}\right]. \tag{16}$$

Here, by virtue of inequality (10), we retain only the terms that are linear in δn. We also neglect the dispersion of ion acoustic waves because the characteristic wavelengths in our problem are either comparable with the system length L or several times shorter. In other words, these characteristic spatial scales are too short for the dispersion of ion acoustic waves to have any significant effect. In an amplifier, the time variations in the amplitude of the electric field of a microwave are associated exclusively with plasma motions; consequently, the second term on the right-hand side is as small as $c_s/v_{ph} \ll 1$ in comparison with the first term and thus can be omitted. As a result, Eq. (16) reduces to

$$\left(c_s^2\frac{\partial^2}{\partial z^2} - \frac{\partial^2}{\partial t^2}\right)\delta n_p = \frac{n_0}{M}\frac{\partial F}{\partial z}, \tag{17}$$

where $F = -\dfrac{e^2}{4m\omega^2}G^2(\mathbf{r})\dfrac{\partial}{\partial z}|E_0(z, t)|^2$ is the microwave ponderomotive force.

The steady solutions to Eq. (17) describe the plasma density redistribution, and the unsteady ones describe the generation of ion acoustic waves by an external distributed force (the right-hand side of the equation) and their propagation under the action of this force. However, we are interested only in the effect of the plasma density value on the dispersion properties of an electrodynamic structure. But the dispersion properties are described by the function η, which depends on the plasma density integrated over the plasma cross section. Multiplying Eq. (17) by the function G^2 and integrating over the cross section of the waveguide structure, we obtain a second-order differential equation describing the dependence of the function η on the microwave ponderomotive force. This second-order equation can be reduced to the following two first-order equations:

$$\frac{\partial \eta}{\partial \tau} + \frac{\partial u}{\partial \zeta} = 0, \quad \frac{\partial u}{\partial \tau} + \frac{\partial \eta}{\partial \zeta} = \Phi(\zeta, \tau), \tag{18}$$

where u is the dimensionless plasma velocity averaged over the plasma cross section,

$$u(\zeta, \tau) = \frac{k_0}{2\delta k_0}\frac{\omega_p}{v_{ph}}\frac{\partial v_{ph}}{\partial \omega_p}\frac{\bar{v}(\zeta, \tau)}{c_s},$$

with v the dimensional plasma velocity. The dimensionless microwave ponderomotive force Φ is defined by the expression $\Phi = -\Lambda\dfrac{\partial |\varepsilon|^2}{\partial \zeta}$. The parameter

$$\Lambda = \frac{mv_b^2}{2T_e}\left(\frac{\delta k_0}{k_0}\right)^3\frac{\omega_p}{v_{ph}}\frac{\partial v_{ph}}{\partial \omega_p}$$
$$\times \int_{S_p} G^4(\mathbf{r})ds\left(G^2(0)\int_{S_p} G^2(\mathbf{r})ds\right)^{-1} \tag{19}$$

is the main parameter of the problem. With the help of the above expression for the growth rate δk_0 of the BPI, we can readily see that the parameter Λ_0, which satisfies condition (7) and serves merely to obtain estimates, differs from the main parameter Λ only in having the factor that bears witness to the radial plasma density profile.

Equations (18) should be supplemented with boundary conditions at the entrance (left) boundary of the system, $\zeta = 0$, and at its exit (right) boundary, $\zeta = l = \delta k_0 L$, where L is the dimensional length of the system. In what follows, we use the most general linear boundary conditions with which Eqs. (18) can be solved on the closed unit interval $0 \le \zeta \le l$ in a mathematically correct way:

$$(1 + \gamma)\eta(0, \tau) + (1 - \gamma)u(0, \tau) = 0,$$
$$(1 + \gamma)\eta(l, \tau) - (1 - \gamma)u(l, \tau) = 0. \tag{20}$$

Here, the reflection coefficients of the entrance and exit ends of the system for an ion acoustic wave are assumed to be the same and are denoted by γ ($-1 < \gamma < 1$). The signs in boundary conditions (20) are chosen so that the anti-Hermitian part of the operator in differential equation (18) with these boundary conditions is negative. Otherwise, the operator would describe an unstable system, in which perturbations grow even in the absence of external forces.

The closed set of Eqs. (15) and (18) with boundary conditions (13) and (20) constitutes a self-consistent mathematical model of the spatiotemporal dynamics of the magnetized plasma and the microwave field generated in it by an electron beam.

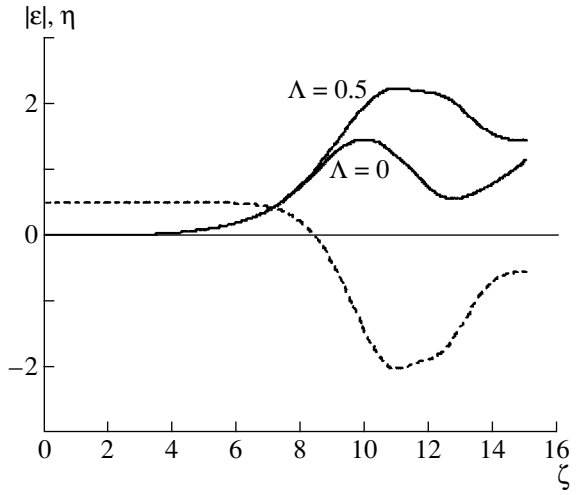

Fig. 1. Steady-state longitudinal profiles of the wave amplitude $|\varepsilon(\zeta)|$ (solid curves) and the plasma density perturbation $\eta(\zeta)$ (dashed curve) calculated for small values of the parameter Λ.

4. STEADY SOLUTIONS AND THEIR STABILITY

We begin with a qualitative analysis of the steady solutions to Eqs. (15) and (18). For $\Lambda = 0$, the plasma density is unperturbed ($\eta = 0$) and Eq. (15) describes the development of the BPI in a homogeneous plasma. In this case, the growth of the wave amplitude is limited by the nonlinearity of the motion of beam electrons [18], and we have $\max\{|\varepsilon|\} \equiv |\varepsilon_{\max}|_{\Lambda = 0} \simeq 1.47$. It is clear that, for $\Lambda \ll 1$, the maximum amplitude $|\varepsilon_{\max}(\Lambda)|$ is determined by the same mechanism for the saturation of the instability.

When the parameter $\Lambda \gg 1$ is large, the wave amplitude is always small, $|\varepsilon| \ll 1$. In fact, the instability stops growing if the detuning is on the order of unity, $\eta \sim 1$. From Eqs. (18), the steady-state value of η can be estimated as $\eta \sim \Lambda|\varepsilon|^2$. Consequently, the maximum amplitude of the excited wave is small, $|\varepsilon_{\max}| \sim \Lambda^{-1/2} \ll 1$. These qualitative estimates indicate that, as the parameter Λ increases, the physical mechanism for the saturation of the BPI changes: for $\Lambda \ll 1$, the instability saturates because of the nonlinear nature of the motion of beam electrons in the wave field and, for $\Lambda \gg 1$, the saturation mechanism is the nonlinear dispersion of the eigenmode of a plasma-filled waveguide structure.

Let us consider the steady solutions to Eqs. (15) and (18) in more detail. The longitudinal plasma density profile satisfying boundary conditions (20) has the form

$$\eta(\zeta) = -\Lambda|\varepsilon(\zeta)|^2 + \frac{\Lambda}{2}(|\varepsilon_l|^2 + |\varepsilon_0|^2); \qquad (21)$$

where $|\varepsilon_{0,l}|$ are, respectively, the amplitudes of the microwave at the left and right boundaries of the system.

Using the inequality $\Lambda|\varepsilon(\zeta)|^2 \ll 1$, which holds over the entire length ζ_ν of the integration interval, and also the inequality $|\varepsilon_l| \gg |\varepsilon_0|$, we obtain from Eq. (15) and expression (21) the equations

$$\frac{\partial\varepsilon}{\partial\zeta} + i\Lambda(|\varepsilon_0|^2 - |\varepsilon(\zeta)|^2)\varepsilon = -\frac{1}{2\pi}\int_0^{2\pi} e^{-i\varphi(\varphi_0,\zeta)}d\varphi_0,$$
$$\frac{\partial^2\varphi}{\partial\zeta^2} = \mathrm{Re}(\varepsilon e^{i\varphi}). \qquad (22)$$

Since Eqs. (22) cannot be solved analytically, we first present the results from solving them numerically and then, based on the interpretation of the numerical results, propose approximate formulas describing the behavior of the solutions at different values of the parameter Λ.

Figure 1 shows the profiles $\eta(\zeta)$ and $|\varepsilon(\zeta)|$ calculated for a comparatively small value $\Lambda \le 1$ and, for comparison, for $\Lambda = 0$ (which corresponds to a homogeneous plasma). We can see that the effect of the microwave ponderomotive forces is to increase the maximum wave amplitude. This effect, which was investigated in [19], is associated with a prolonged synchronization between the decelerated beam and the beam-driven wave, whose phase velocity decreases as its amplitude grows. A decrease in plasma density, which lowers the wave phase velocity (at $\Lambda > 0$), correlates with the growth of the wave amplitude and, consequently, with the reduction in the velocity of the beam electrons. This correlation is ensured by the microwave ponderomotive force, which expels the plasma from the region of the stronger microwave field. The value of the parameter Λ determines the extent to which the changes in the wave velocity and the velocity of the beam electrons are correlated: for $\Lambda \ll 1$, the deceleration of the beam electrons is faster, whereas, for $\Lambda \gg 1$, the wave velocity decreases at a faster rate. Obviously, the synchronism between the wave and the beam is best maintained at a certain value $\Lambda = \Lambda_{\mathrm{opt}} \sim 1$, at which the BPI has the maximum efficiency.

For $\Lambda \gg 1$, a rapid decrease in the wave phase velocity breaks the synchronism and the instability saturates even when the wave amplitude is small, $|\varepsilon| \ll 1$, i.e., before the motion of the beam electrons becomes nonlinear. Representative profiles $\eta(\zeta)$ and $|\varepsilon(\zeta)|$ calculated numerically for $\Lambda \gg 1$ are displayed in Fig. 2. In this case, the wave amplitude $|\varepsilon_{\max}|$ at which the instability saturates can be estimated from the condition that the instability growth rate vanishes when the detuning is approximately equal to $\eta \approx -\Lambda|\varepsilon|^2 = -1.5$:

$$|\varepsilon_{\max}(\Lambda)| \approx \frac{1.5}{\sqrt{\Lambda}} \ll 1. \qquad (23)$$

The smallness of the wave amplitude at large Λ values allows us to simplify Eqs. (22). To do this, we linearize the second of Eqs. (12) in small perturbations

$\delta\varphi \sim \varepsilon \ll 1$ of the phases $\varphi = \varphi_0 + \delta\varphi$ of the beam electrons and integrate over the initial phases in the first of these equations. As a result, we obtain

$$\frac{d^2}{d\zeta^2}\left[\frac{d\varepsilon}{d\zeta} + i\Lambda(|\varepsilon_0|^2 - |\varepsilon|^2)\varepsilon\right] = \frac{i}{2}\varepsilon. \quad (24)$$

Equation (24) can be analyzed by using the results obtained in [20]. In this way, we consider the equation

$$\frac{d^2}{d\zeta^2}\left[\frac{d\varepsilon}{d\zeta} + if(\zeta)\varepsilon\right] = \frac{i}{2}\varepsilon. \quad (25)$$

If the characteristic scale l_f on which the function $f(\zeta)$ varies is large, $l_f \gg 1$, then the solution to Eq. (25) in the adiabatic approximation can be represented as

$$\varepsilon(\zeta) = \varepsilon(0)\exp\left(\int_0^\zeta \delta k(\zeta')d\zeta'\right), \quad (26)$$

where δk is the solution to the characteristic equation

$$\delta k^2[\delta k + if(\zeta)] = i/2. \quad (27)$$

To within an unessential factor in front of the exponential function, the adiabatic approximation well describes the solution to Eq. (25) even for $l_f \geq 1$, provided that the real part of the argument of the exponential function in solution (26) is large and that the function $f(\zeta)$ does not decrease to the value $f = -1.5$. In the vicinity of the point at which the function $f(\zeta)$ has this value and, accordingly, at which the two roots of Eq. (27) merge into one, the adiabatic approximation fails to hold. For smaller values of f, after the point of merging of the roots (the turning point) is passed from $f > -1.5$ to $f < -1.5$, the solution is represented as the sum of two stable ($\mathrm{Re}(\delta k) = 0$) solutions describing two stable waves of equal amplitude.

Locally, in a small neighborhood of the turning point, Eq. (25) can be reduced to the Airy equation describing the reflection of an electromagnetic wave from a smoothly inhomogeneous medium (see, e.g., [21]). The problem of passage through the turning point in an optically active medium (in particular, in the beam–plasma system under consideration) and the problem of the reflection of a wave in an optically inactive medium are mutually inverse. In the problem of reflection, the wave incident from the region where $f < -1.5$ is exponentially damped in the opaque region, i.e., when it penetrates deeper into the medium after passing through the turning point, and produces a reflected wave of the same amplitude. In the problem of passage through the turning point in an optically active medium, the wave incident from the region where $f > -1.5$ grows exponentially when approaching the turning point and, behind the turning point, it decays into two waves of equal amplitudes.

If we choose the function $f(\zeta)$ to be $f(\zeta) = \Lambda(|\varepsilon_0|^2 - |\varepsilon(\zeta)|^2)$, where $\varepsilon(\zeta)$ is a solution to Eq. (24), then we can see that Eqs. (24) and (25) have the same solution. Hence, the technique of the above analysis can be applied to explain the behavior of the solutions to Eq. (24) that are shown in Fig. 2. In the initial stage (until $f > -1.5$), the real part of one of the roots δk of the characteristic equation is positive and the wave amplitude grows, in which case the function f decreases up to the value $f = -1.5$, which corresponds to the turning point. Behind this point, there is no instability and the field has the form of the beatings of two stable waves. Behind the maximum of the total field, the wave amplitude decreases and the system again passes into the instability region ($f > -1.5$). However, the initial conditions in the instability region are now different from those at the beginning of the process. The beam electrons are already bunched; therefore, in this stage, the wave interacts with a modulated beam. In this case, the dependence $|\varepsilon(\zeta)|$ is described by a linear function. That the field amplitude at the beginning of this stage decreases stems from the following circumstance: when a bunch of the beam electrons enters the instability region, it occurs in the accelerating phase of the field and acquires energy from the wave. After passing through the point at which $|\varepsilon| = 0$, the field phase changes by π and the modulated beam again excites the wave. This interpretation of the behavior of the solutions to Eq. (24) is confirmed by the results from particle-in-cell simulations of the motion of the beam electrons using the general nonlinear equations.

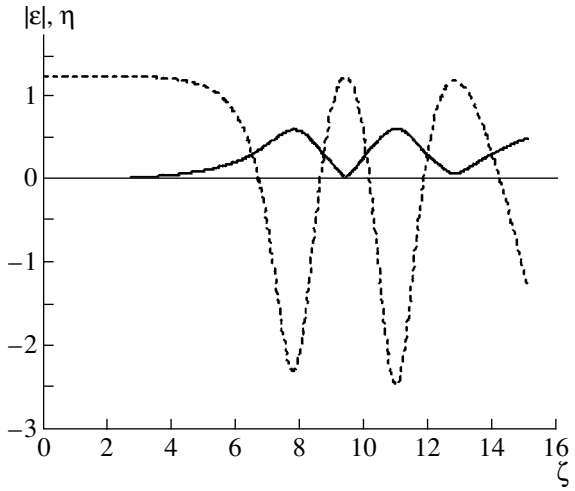

Fig. 2. Steady-state longitudinal profiles of the wave amplitude $|\varepsilon(\zeta)|$ (solid curve) and the plasma density perturbation $\eta(\zeta)$ (dashed curve) calculated for $\Lambda = 10$.

Now, we present estimates that make it possible to determine the dependence $|\varepsilon_{\max}(\Lambda)|$. For $\Lambda \gg 1$, we can use formula (23). For $\Lambda \ll 1$, the mechanism for the instability saturation is associated with the trapping of the beam electrons by the field of the beam-generated wave. Consequently, near the maximum in the dependence $|\varepsilon(\zeta)|$, the beam electrons are so well bunched with respect to the wave phase that we can considerably

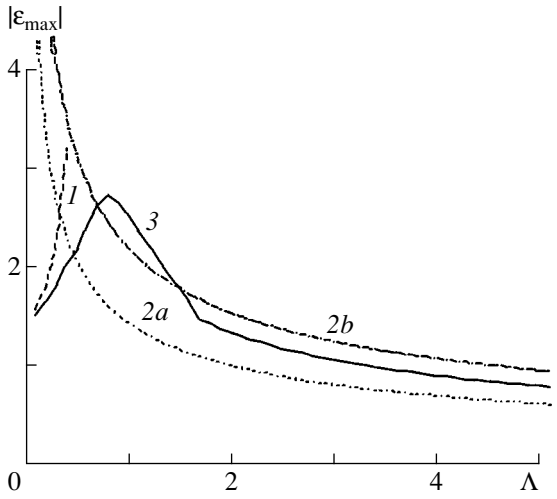

Fig. 3. Profiles of the instability saturation amplitude $|\varepsilon_{max}(\Lambda)|$ calculated for $\Lambda \ll 1$ by formula (32) (curve *1*) and for $\Lambda \gg 1$ by formula (23) without (curve *2a*) and with (curve *2b*) allowance for an increase in the wave amplitude behind the turning point. Profile (*3*) was obtained by solving Eqs. (22) numerically.

simplify the problem by treating the bunch as being pointlike. In this approximation, Eqs. (22) take the form

$$\frac{\partial \varepsilon}{\partial \zeta} - i\Lambda|\varepsilon(\zeta)|^2\varepsilon = -e^{-i\varphi}, \quad \frac{\partial^2 \varphi}{\partial \zeta^2} = \mathrm{Re}(\varepsilon e^{i\varphi}), \quad (28)$$

where we have neglected the initial wave amplitude $|\varepsilon_0|$. Equations (28) have the integral of motion

$$\frac{d\varphi}{d\zeta} + \frac{1}{2}|\varepsilon|^2 = \mathrm{const}, \quad (29)$$

which is the energy conservation law. Substituting the wave amplitude in the form $\varepsilon = \rho e^{i\theta}$ into Eqs. (28) and (29) yields the equations

$$\frac{d\rho}{d\zeta} = -\cos\psi,$$
$$\frac{d\psi}{d\zeta} = \mathrm{const} - \frac{1}{2}\rho^2(1-2\Lambda) + \frac{1}{\rho}\sin\psi, \quad (30)$$

where $\psi = \varphi + \theta$. Equation (30) can also be written as

$$\frac{d\rho}{d\psi} = -\cos\psi\left[\mathrm{const} - \frac{1}{2}\rho^2(1-2\Lambda) + \frac{1}{\rho}\sin\psi\right]^{-1}.$$

Choosing the quantity $\tau = \sin\psi$ as an independent variable, we obtain

$$\frac{d\rho}{d\tau} = -\left[\mathrm{const} - \frac{1}{2}\rho^2(1-2\Lambda) + \frac{1}{\rho}\tau\right]^{-1}. \quad (31)$$

The dependence on the parameter Λ can be eliminated from Eq. (31) by making the replacement $\rho = y/\sqrt{1-2\Lambda}$ and $\tau = x/\sqrt{1-2\Lambda}$. This indicates that the dependence of the maximum wave amplitude on the parameter Λ is determined by the formula

$$|\varepsilon_{max}(\Lambda)| \approx \frac{|\varepsilon_{max}(0)|}{\sqrt{1-2\Lambda}}. \quad (32)$$

Figure 3 depicts the functions $|\varepsilon_{max}(\Lambda)|$ calculated by solving Eqs. (22) numerically and obtained from approximate formulas (23) and (32). Formula (23) somewhat underestimates the value of $|\varepsilon_{max}(\Lambda)|$ because it does not account for the aforementioned increase in the wave amplitude behind the turning point. The dependence $|\varepsilon_{max}(\Lambda)|$ obtained with allowance for this effect is shown by curve *2b* in Fig. 3. Formula (32) overestimates the maximum wave amplitude because it was derived under the assumption that the bunch of beam electrons is pointlike.

Let us summarize the results obtained from studying the question as to how the steady-state regimes of the BPI in a plasma-filled slow-wave structure change with increasing plasma density and/or beam current (parameter Λ). For small values of this parameter ($\Lambda \ll 1$), the ponderomotive effects can be neglected. For somewhat larger values ($\Lambda < 1$), the wave amplitude at which the instability saturates is governed by the simultaneous effect of two nonlinear mechanisms: (i) the trapping of the beam electrons by the field of the excited wave and (ii) the nonlinearity of the plasma. The effect of the plasma nonlinearity produced by the microwave ponderomotive force is a reduction in the plasma density and, as a consequence, a decrease in the wave phase velocity. Because of the synchronous decrease in the electron beam velocity and in the phase velocity of a microwave, the bounce period of the trapped beam electrons is longer than that in a homogeneous plasma and the microwave field is stronger. Starting from $\Lambda \approx 1$, the phase velocity of a microwave differs substantially from the beam velocity even in the bunching stage. The positive effect of the decrease in the phase velocity of a microwave on the trapped beam electrons is partially reduced by a decrease in the efficiency with which the wave traps the beam electrons and an increase in the energy spread of the electrons in the bunch. As a result, at a certain Λ value, the saturation amplitude reaches its maximum and then decreases. For $\Lambda \gg 1$, the plasma density is essentially nonuniform even in the linear stage of the amplification process; in this case, the maximum amplitude of the microwave is determined exclusively by the plasma nonlinearity (the departure of the wave from resonance with the beam) and is so small that the wave ceases to trap the beam electrons.

The problem of the stability of steady solutions was investigated in [22]. Here, we briefly outline the results obtained in that paper. The onset of a regime in which the output signal from the system under consideration (an amplifier with a plasma-filled waveguide structure) is self-modulated is due to the generation of an ion

acoustic wave by the microwave ponderomotive force. The ion acoustic wave propagates in the direction opposite to the propagation direction of the beam, thereby giving rise to distributed feedback and changing the system into a generator of low-frequency waves. The frequency Ω at which self-oscillations are generated satisfies the equation

$$\sin(l\Omega/2) = 0, \tag{33}$$

provided that the parameter Λ is larger than its critical value

$$\Lambda_c = 3(\alpha l)^{1/2}[2^{1/3}|\varepsilon_0|^2\exp(2\alpha l)]^{-1}, \tag{34}$$

where $\alpha = \sqrt{3}/2^{4/3}$ is the dimensionless growth rate of the BPI in a homogeneous plasma.

According to formula (34), which is valid for $|\varepsilon_0|\exp(\alpha l) \le 1$ and $\alpha l \gg 1$, the critical value of the parameter Λ decreases with increasing system length l and (as expected) should become minimum in the range $|\varepsilon_0|\exp(\alpha l) \ge 1$, in which this formula fails to hold. The exact minimum critical value Λ_c was obtained by investigating the stability of the steady solutions to Eqs. (15) and (18) with boundary conditions (13) and (20) by numerical methods. The parameters of the problem—the length of the interaction region, the initial wave amplitude, and the reflection coefficient of an ion acoustic wave from the ends of the system—were chosen to be close to those in the experiments described in Section 5. The solutions obtained numerically showed that the minimum critical value of the parameter Λ only slightly depends on the reflection coefficient γ and is equal to $\Lambda_c = 0.6$. Accordingly, the steady solutions that have been examined above in the case $\Lambda \gg 1$ are unstable and, therefore, cannot be observed experimentally. However, some of the properties of these solutions, e.g., the saturation amplitude given by approximate formula (23), determine the parameters of the unsteady interaction regimes.

5. THEORETICAL AND EXPERIMENTAL STUDY OF THE SELF-MODULATION REGIME OF THE BPI

The self-consistent dynamics of the plasma and of the microwave fields generated in it by an electron beam was investigated in experiments with a magnetized plasma waveguide. The experimental device in the form of a 12-cm-diameter glass tube with length $L = 76$ cm was placed in a uniform guiding magnetic field with a strength of 1.5 kG. The tube was filled with a gas (Ar, He) at a controlled pressure. The parameters of an electron beam injected into a neutral gas were as follows: the beam current was 50 mA, the energy of the beam electrons was 1 keV, and the beam radius was 1 cm. The plasma in the system was produced by impact ionization of a neutral gas by beam electrons and, in a sufficiently strong microwave field, by conventional ionization processes occurring in a BPD. The plasma density and the amplitude of the microwave field generated by the beam were measured by Langmuir probes and receiving antennas, installed 15 cm from the tube ends. The signals from the probes were digitized (with a time resolution of 0.1 μs) and stored in a computer for further processing. The only parameter that was varied in the experiments described below was the neutral gas pressure (and, accordingly, the density of the produced plasma), while the beam parameters were not changed.

Before proceeding to a description of the experimental data and comparing them with the theoretical results, let us make the following remarks. A description of the behavior of the solutions to Eqs. (15) and (18) with boundary conditions (13) and (20) in different ranges of the parameters Λ, l, ε_0, and γ is a laborious and complicated task. That is why we present only the results that were obtained for the parameter values corresponding to the experimental conditions under discussion. Theoretical investigation of the BPI in unsteady regimes ($\Lambda > \Lambda_c$) was carried out mainly by numerical methods, and, when possible, analytic estimates were obtained for certain parameter ranges. The guiding magnetic field in the experiments was strong enough for the motion of plasma electrons to be treated as one-dimensional over the entire range of gas pressures. Since the main processes in experiments with each of the two gas species were observed to be qualitatively the same, we will describe only the results of experiments with argon.

Numerical calculations of the dispersion properties of the experimental plasma waveguide made it possible to determine the resonant frequency f, the dimensionless length δkL, and the parameter $\delta k/k_0$ as functions of the plasma density. The calculated results are illustrated in Figs. 4a–4c.

Using the plots shown in Figs. 4a–4c, the results of theoretical investigations carried out for steady-state regimes, and the results from numerical simulations of unsteady regimes, we determined how the mean oscillation energy $\tilde{W}_e(0)$ of the plasma electrons at the axis of the system; the parameter Λ defined by formula (19); and its critical value Λ_c, at which the steady-state regime becomes unstable, depend on the plasma density. The corresponding plots are presented in Fig. 4d, in which the dashed line indicates the mean oscillation energy of the plasma electrons above which they are capable of ionizing argon. In calculations, we varied the plasma electron temperature from 3 eV (which corresponds to the absence of a BPD) to 10 eV (which corresponds to the most highly developed stage of the discharge).

It follows from Fig. 4a that the threshold plasma density for the onset of the BPI is 0.8×10^9 cm^{-3}. However, the amplification coefficient is larger than unity only when the dimensionless length of the system δkL

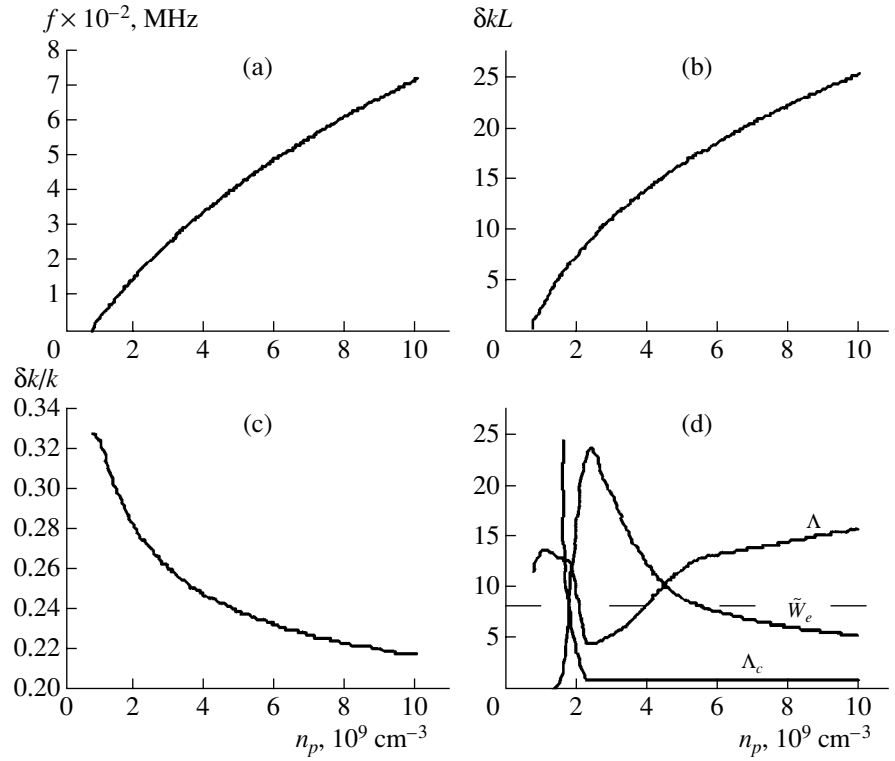

Fig. 4. System parameters calculated as functions of the plasma density: (a) the resonant generation frequency f; (b) the dimensionless length δkL of the system; (c) the parameter $\delta k/k$; and (d) the parameter Λ, its critical value Λ_c, and the mean oscillation energy $\tilde{W}_e$ of the plasma electrons. The dashed line indicates the mean oscillation energy of the plasma electrons above which they are capable of ionizing argon.

is sufficiently large, $\delta kL \geq 3$. According to Fig. 4b, this condition is satisfied for $n_p \geq 1.1 \times 10^9$ cm^{-3}. At such a plasma density, the calculated frequency of the excited synchronous wave is 60 MHz. In experiments, microwave signals above the fluctuation level were observed to arise at a frequency of 56 MHz in the pressure range $p \geq 1.1 \times 10^{-5}$ torr. The pressure of a plasma with the density $n_p = 1.1 \times 10^9$ cm^{-3} can be estimated from the condition that the number of ions produced by the beam in the entire chamber volume is equal to the number of ions escaping from the chamber through its ends:

$$I_b N_0 \sigma_b / eS_b = n_p c_s / L, \tag{35}$$

where N_0 is the neutral gas density and σ_b is the rate of ionization of the molecules of a neutral gas by the beam electrons. The rate of escape of the ions in the longitudinal direction is equal to the ion acoustic speed c_s. According to formula (35), the pressure is estimated to be 2.0×10^{-5} torr; this value may be considered to agree fairly well with the experimentally measured pressure, especially if we take into account the fact that formula (35) is only approximate.

Before proceeding to an analysis of how the nature of the BPI changes as the neutral gas pressure is increased, we determine the range of plasma densities at which the instability can occur.

The maximum oscillation energy $\tilde{W}_{\max}$ of the plasma electrons in the wave field at the axis of the structure is described by the expression

$$\tilde{W}_{\max} = 2\tilde{W}_e = 2eU\left(\frac{\delta k}{k_0}\right)^4 |\varepsilon|^2. \tag{36}$$

The BPI may develop in the system when this energy is higher than the ionization energy of argon, $W_i \approx 16$ eV. The corresponding value of the mean energy, $\tilde{W}_e(0) = 8$ eV, is shown by the dashed line in Fig. 4d.

At plasma densities close to 1.1×10^9 cm^{-3}, the device operates in the linear amplification regime in which the microwave amplitude near the exit end is small. At such plasma densities, the critical value Λ_c given by formula (34) is large and the condition $\Lambda > \Lambda_c$ for the onset of the low-frequency instability fails to hold. The energy of oscillations of the plasma electrons in the wave field is insufficient for the onset of the BPI.

As the pressure increases, the quantity Λ changes insignificantly. The logarithm of the gain increases in proportion to $\sim\delta kL$ (Fig. 4b), which leads to an abrupt

reduction in the threshold value Λ_c and an increase in $\tilde{W}_e$. At a plasma density of 1.67×10^9 cm^{-3} (corresponding to a pressure of 3.0×10^{-5} torr), the steady operating mode becomes unstable ($\Lambda = \Lambda_c$). At a slightly higher pressure (3.2×10^{-5} torr), $\tilde{W}_e(0)$ becomes equal to the threshold value. This scenario was observed experimentally; the corresponding pressures were found to be 1.65×10^{-5} and 1.7×10^{-5} torr, respectively.

As the steady operating mode of the device becomes unstable, microwave ponderomotive forces give rise to a low-frequency instability; as a result, the amplitude of the wave amplified by the beam becomes deeply (up to 100%) modulated at the exit from the system. That is why the mean and pulsed powers of a microwave signal may differ substantially from one another. Let us employ the theory developed in Sections 2–4 to estimate the mean square amplitude of the signal.

The onset and growth of the plasma density perturbations are described by Eqs. (18), an equivalent form of which is

$$\frac{\partial^2 \eta}{\partial \tau^2} - \frac{\partial^2 \eta}{\partial \zeta^2} = \Lambda \frac{\partial^2 |\varepsilon|^2}{\partial \zeta^2}. \quad (37)$$

Let the initial profile $|\varepsilon(\zeta)|$ of the amplitude of the wave generated by the beam in an originally homogeneous plasma be steady state. The maximum amplitude $|\varepsilon|_{\max}$ occurs in the region $\Delta\zeta \sim 1$. For $\Lambda \gg 1$, the microwave ponderomotive force expels the plasma from this region so rapidly that the plasma density perturbation can be regarded as being immobile on the time scale on which it grows. In this case, the second term on the left-hand side of Eq. (37) is much smaller than the first term,

$$\left|\frac{\partial^2 \eta}{\partial \zeta^2}\right| \ll \left|\frac{\partial^2 \eta}{\partial \tau^2}\right|. \quad (38)$$

With allowance for the fact that the instability saturates when $|\eta| \sim 1$, Eq. (37) and inequality (38) yield the following estimate for the characteristic time scale $\Delta\tau_g$ on which the plasma density perturbation grows:

$$\Delta\tau_g \sim \Lambda^{-1/2} |\varepsilon|_{\max}^{-1}. \quad (39)$$

Hence, the BPI stops growing time $\Delta\tau_g$ after its onset; in other words, $\Delta\tau_g$ is the duration of the generated microwave pulse. The interval $\Delta\tau_p$ between the generated pulses is determined by the time during which the plasma density perturbation escape from the interaction region:

$$\Delta\tau_p \sim l_0, \quad (40)$$

where l_0 is the dimensionless distance from the entrance end of the structure to the point at which the wave amplitude is maximum; in order of magnitude, it is equal to the dimensionless length l of the system. For the experimental conditions in question, we have $l \approx 10$.

The process described above is characterized by the dimensionless square pulse (maximum) amplitude $|\varepsilon|^2_{\max}$ and the mean square amplitude

$$|\varepsilon|^2_{\text{mean}} \sim |\varepsilon|^2_{\max} \frac{\Delta\tau_g}{\Delta\tau_p} \sim |\varepsilon|_{\max} \Lambda^{-1/2} l_0^{-1}. \quad (41)$$

The higher the pressure, the more complicated the character of the processes that occur throughout the BPD. In fact, as the mean amplitude of the microwave field continues to grow, the parameter Λ_c decreases and the power of the plasma source (the BPD) increases, raising the density, temperature, and radius of the plasma. As a consequence of the increase in the plasma temperature and radius, the parameter Λ decreases. Numerical simulations show that, because of the synchronous decrease in the parameter Λ and its critical value Λ_c ($\Lambda - \Lambda_c \approx 4$, as seen in Fig. 4d), the extent to which the regime of the amplification of a microwave is nonsteady should be relatively low, in which case the mean square amplitude $|\varepsilon|^2_{\text{mean}}$ at the exit from the system is only slightly smaller than that in the steady-state amplification regime.

An increase in the amplification coefficient leads to a saturation of the BPI within the system; at a density of 2.4×10^9 cm^{-3} (corresponding to a pressure of 4.3×10^{-5} torr), the mean square amplitude of the microwave field reaches its maximum value $|\varepsilon|^2_{\text{mean}} \approx 4.5$, which indicates that the maximum power of the BPD (i.e. of the source of the plasma) is also achieved. Note that the numerically calculated mean square amplitude of the microwave field is larger than that obtained for a homogeneous plasma ($|\varepsilon|^2_{\max} \approx 2.3$) but is smaller than that obtained in Section 4 for a steady-state regime ($|\varepsilon|^2_{\max} \approx 6$) with allowance for the effect of prolonged synchronization due to the microwave ponderomotive force.

Note that the exact dependences of the temperature and radius of the plasma produced during the BPD on its density can only be determined by solving a complicated, two-dimensional, time-dependent, self-consistent problem. In order to derive qualitative dependences, we used the experimental data and the estimates obtained from analytical and numerical calculations. These dependences show that the effective radius of the plasma and its temperature at the very beginning of the BPD are about 1 cm and 3 eV, respectively, and, as the instability evolves into its most highly developed stage, they increase to 2 cm and 10 eV.

Numerical simulations show that, after the microwave field amplitude has reached its maximum value, the parameter Λ_c changes only slightly as the plasma density increases. In this stage, an important role is played by the behavior of the parameter $\delta k/k$ (Fig. 4c). Expression (36) implies that, as this parameter decreases monotonically with increasing pressure

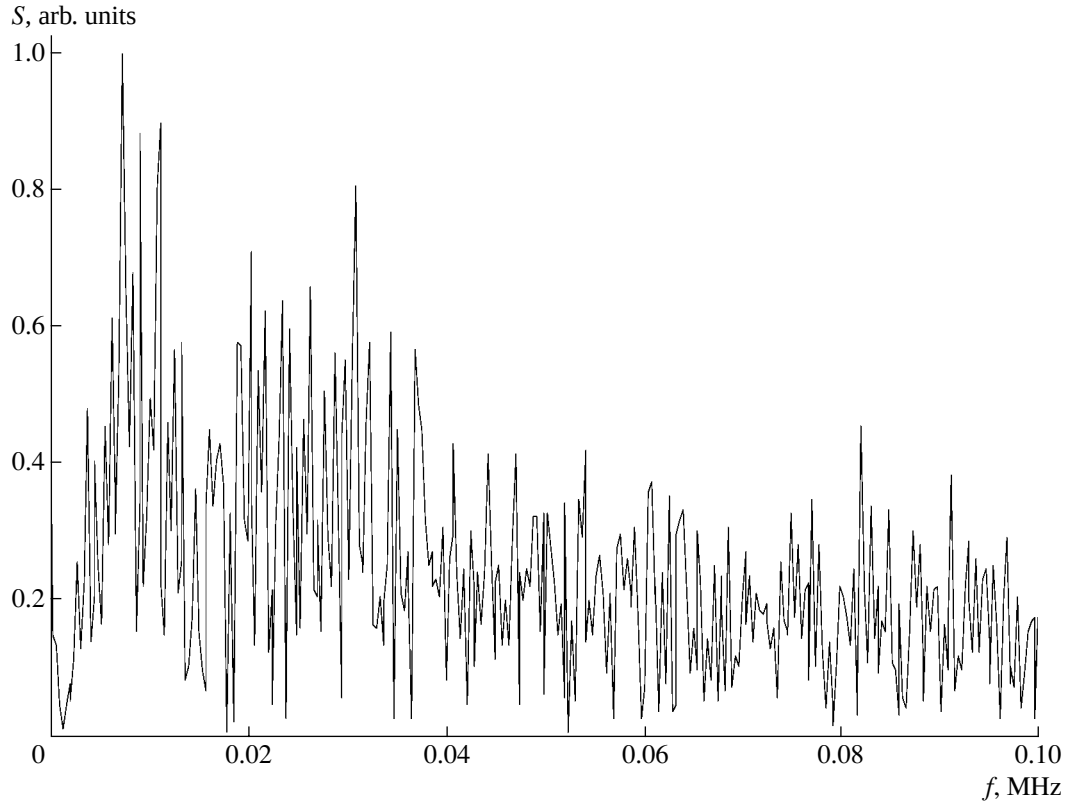

Fig. 5. Spectral amplitude $S(f)$ of plasma density oscillations at a pressure of 1.65×10^{-5} torr before the onset of a BPD.

(even at a constant mean square amplitude $|\varepsilon|^2_{\text{mean}}$), the mean energy of the electron oscillations becomes lower; as a result, both the temperature and the radius of the plasma produced decrease.

In turn, this effect acts to increase the parameter Λ and, by virtue of formula (41), to reduce the mean square amplitude $|\varepsilon|^2_{\text{mean}}$. As a result, the mean energy $\tilde{W}_e$ decreases even more rapidly. At a plasma density of about $n_{pc} \approx 5.8 \times 10^9$ cm^{-3} (at a pressure of 10.5×10^{-5} torr), the energy $\tilde{W}_e(0)$ decreases to the threshold value, at which the BPD comes to a halt and the plasma density falls to a level determined by the impact ionization of a neutral gas by beam electrons. As the pressure is further raised, the parameter Λ gradually increases, enhancing the effects of unsteady processes, and the energy $\tilde{W}_e(0)$ decreases. Hence, at low and high pressures, a BPD does not occur in the system, but the BPI in these two cases is radically different in nature: at a low pressure, the instability appears as the generation of a monochromatic signal, whereas, at a high pressure, the effect is the generation of a signal with broad spectrum due to the strong low-frequency self-modulation of the excited microwave.

Note that the device can operate in the relaxation mode, whose physical essence can be outlined as follows. Let a plasma with a density lower than n_{pc} be created by the impact ionization of a gas at a certain pressure by beam electrons. If the plasma density during the BPD increases to $n_p > n_{pc}$, then, in accordance with the above analysis, the discharge comes to an end and the plasma returns to its former density $n_p < n_{pc}$. Then the process repeats itself. Presumably, it is this effect that explains the experimentally observed regular variations in the brightness of the plasma column at a pressure close to the maximum pressure at which the BPD still exists. However, such a suggestion requires more detailed theoretical and experimental justification.

The above-described way in which the BPI changes its nature as the pressure of the neutral gas increases was inferred from numerical and analytical calculations based on the mathematical model developed here. The experimental results that will be described below corroborate the correctness of the model both qualitatively and quantitatively.

At a low pressure of the neutral gas, the density of the plasma produced is low and the BPD cannot occur. The plasma density perturbations are small; at pressures close to the threshold for the onset of a BPD, they are characterized by a wide noise spectrum, an example of which is presented in Fig. 5.

A BPD develops at pressures higher than the critical pressure (1.7×10^{-5} torr). The onset of the discharge is

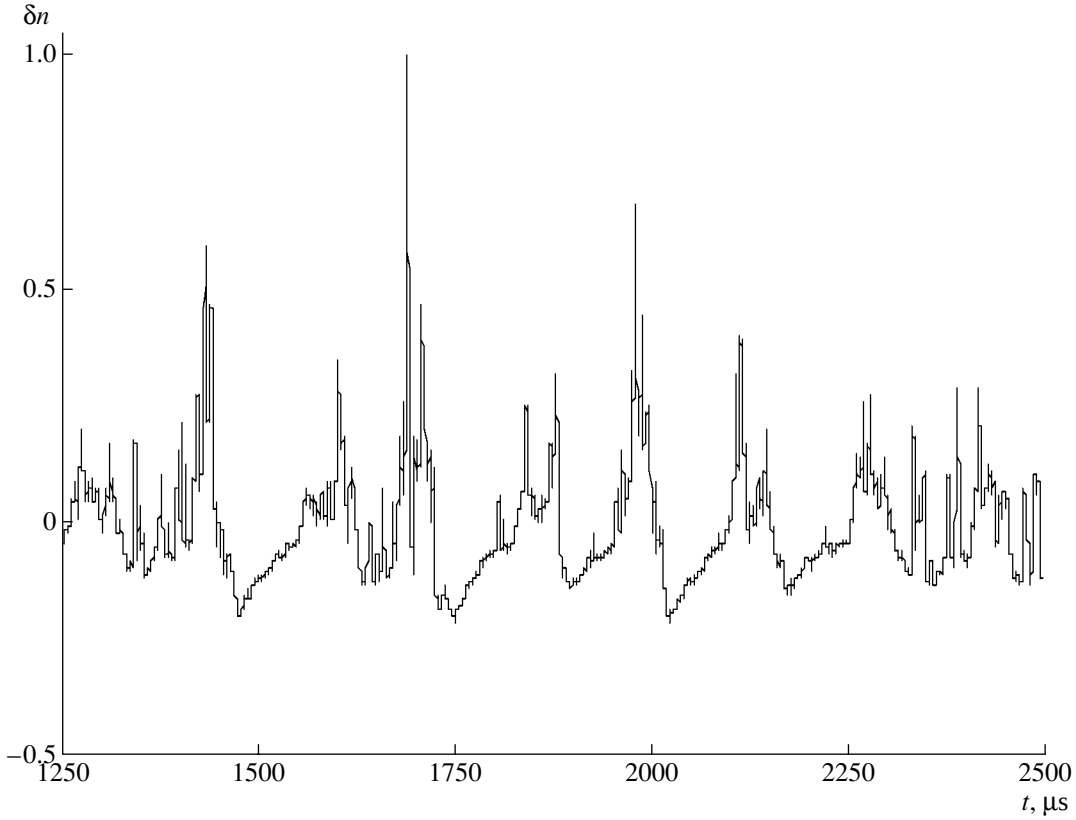

Fig. 6. Plasma density variations $\delta n(t)$ during the BPD.

identified by an abrupt increase in the intensities of signals from the probes; visually, the plasma column becomes far more brighter and wider. In this stage, the dynamics of the plasma density is characterized by two very different time scales (Fig. 6). The period T_{low} of the low-frequency self-modulation of the density at a characteristic frequency of about 6 kHz is well described by the theoretical estimate $T_{\text{low}} \sim L/c_s$.

Against the background of slow variations with the characteristic period T_{low}, short (on a characteristic time scale of several microseconds) sharp peaks in the plasma density are observed, each of which is accompanied by a peak in the amplitude of the generated wave. The upper plot in Fig. 7 presents the time evolutions of the plasma density and wave amplitude in individual peaks (on an enlarged scale). The lower plot demonstrates the cross-correlation function of the variations in the plasma density and wave amplitude in the peaks. The plots shown in Fig. 7 were obtained by numerically filtering out the low-frequency components of the signals.

The time evolutions given in Fig. 7 are typical of a BPD: the plasma density increases under the action of the wave field and decreases after the field vanishes. The maximum of the cross-correlation function is positive and is displaced to the right, indicating that the maximum in the density is reached later than that in the wave amplitude.

Although fast synchronous variations (peaks) in the plasma density and wave amplitude cannot be described by the theory developed here, the above-mentioned experimental data provide evidence that, in the pressure range under consideration, the main plasma source is precisely the BPD. This conclusion is also supported by the calculated results shown in Fig. 4d.

Over the entire pressure range in which a BPD can exist, slow variations in the plasma density are characterized by a line spectrum (representative examples of which are shown in Fig. 8). Note the strong qualitative difference between the spectra of the plasma density oscillations before (Fig. 5) and during (Fig. 8) the BPD.

In the experiments under discussion, all attempts to detect the presence of ion acoustic waves propagating in the direction opposite to the beam propagation direction by measuring the time delay between the signals from spatially separated probes failed regardless of the gas pressure in the discharge. A possible reason for this is that the coefficient of reflection of the ion acoustic waves from the ends of the plasma column may be fairly large. In fact, numerical modeling showed that, even when the reflection coefficient is about 0.4–0.5, the standing waves that exhibit no time delay are

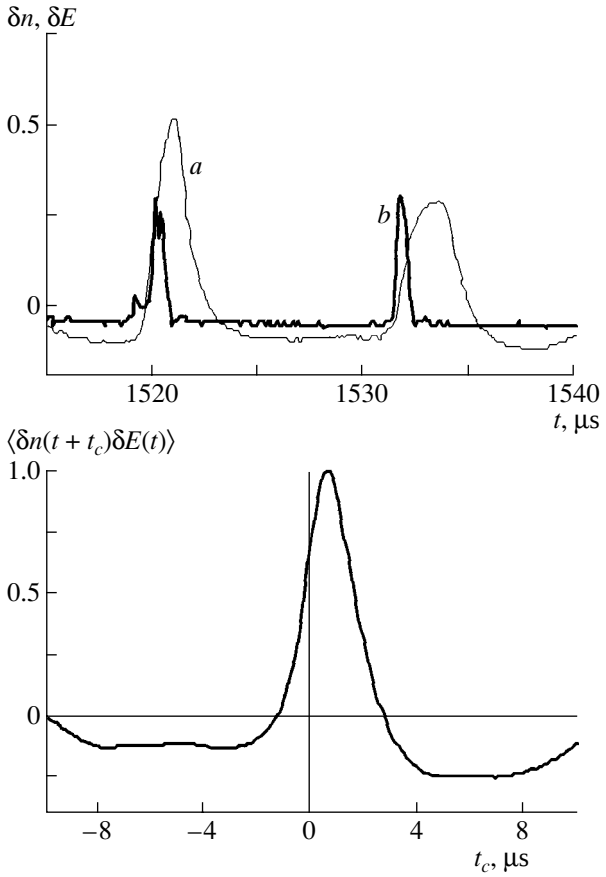

Fig. 7. Waveforms of (*a*) the plasma density variations δn and (*b*) the wave amplitude δE in individual peaks (on the top) and the cross-correlation function $\langle \delta n(t + t_c)\delta E(t)\rangle$ of the plasma density variations and wave amplitude in the peaks (on the bottom).

excited in the system. This result is confirmed by the experimentally measured phase shifts between the dominant spectral components of the signals from the first and second probes (Fig. 8). The even harmonics of the fundamental frequency are seen to have the same phases, whereas the odd harmonics are shifted by 180°. This dependence of the phase difference on the harmonic number is typical of the eigenmodes of a cavity with a symmetric fundamental eigenmode.

The above estimates show that, at pressures above a certain critical pressure, the discharge breaks and the plasma is produced exclusively by the impact ionization of the gas by beam electrons. The disruption of the discharge was experimentally observed to occur at a pressure of 6.0×10^{-5} torr. Representative signals from the probes and a representative spectrum of the plasma density oscillations at pressures higher than 6.0×10^{-5} torr are given in Figs. 9 and 10. Note that, in the absence of a BPD, the spectrum of the plasma density oscillations at a low pressure of the neutral gas (Fig. 5) are similar to that at a high pressure (Fig. 10).

In the absence of a BPD, the amplitude of the low-frequency plasma density oscillations is larger than that during the discharge and the short peaks in the density are lower (cf. Fig. 6 and Fig. 9). One can also see a pronounced time delay (shift) between signals from the probes; the sign of the shift corresponds to a density wave propagating in the direction opposite to that of the beam. Note that the weaker the magnetic field, the more pronounced the time delay (see the lower frame of Fig. 9). The structure of the peaks also changes: an abrupt increase in the wave amplitude is now accompanied by a decrease in the plasma density (Fig. 11). This effect, which is characteristic of the microwave ponderomotive force, becomes more pronounced as the gas pressure increases. From Fig. 11, which presents the waveforms obtained experimentally at a pressure of 9.5×10^{-5} torr, we can see that each peak in the field amplitude is accompanied by a dip in the plasma density. The cross-correlation function obtained by filtering out the low-frequency component of the oscillations of the plasma density and field amplitude (see Fig. 12) differs substantially from that in Fig. 7. In the absence of a BPD, the oscillations of the plasma density and field amplitude are in antiphase and the cross-correlation function has a negative extremum at zero time.

Numerical simulations carried out on the basis of the above model demonstrate that the noise component in the spectrum of the density oscillations becomes more intense as the difference $\Lambda - \Lambda_c$ increases. However, in contrast to the spectra characteristic of regimes without a BPD, the noise component in regimes with a developed discharge is suppressed, although the difference $\Lambda - \Lambda_c$ is fairly large and increases with pressure. Presumably, this circumstance stems from the fact that, within the same spatial region, the discharge acts to increase the plasma density while the microwave ponderomotive force acts to decrease it. Because of the combined action of the discharge and the microwave ponderomotive force, the latter becomes less efficient, or, in other words, the effective value of the parameter Λ decreases. This explanation is indirectly confirmed by the fact that, in experiments with helium (whose threshold ionization energy is one and one-half times that of argon), the spectra measured in all regimes, including regimes with a developed BPD, are analogous to those shown in Figs. 5 and 10.

The dispersion parameters and field structures in a magnetized plasma waveguide and the values of the mean square amplitude of the wave calculated for different values of the parameter Λ made it possible to obtain the theoretical dependence of the mean power P_{mean} of the wave generated by the beam on the neutral gas pressure. Figure 13 illustrates the calculated dependence of the power on the neutral gas pressure and the dependences measured in experiments with helium and argon. We offer the following comments regarding the curves shown in this figure. For both gases, the experimental dependence of the power on pressure has a pro-

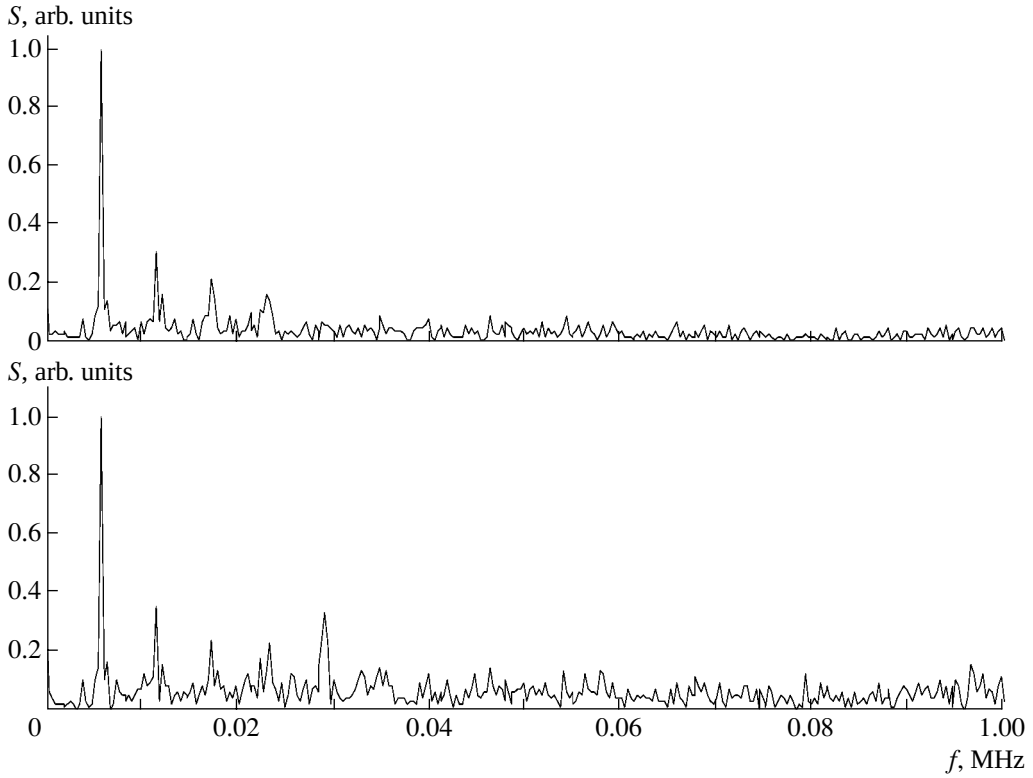

Fig. 8. Low-frequency component of the spectra of the density oscillations. The upper and lower plots present the spectrum of the signal from the first and second probes, respectively.

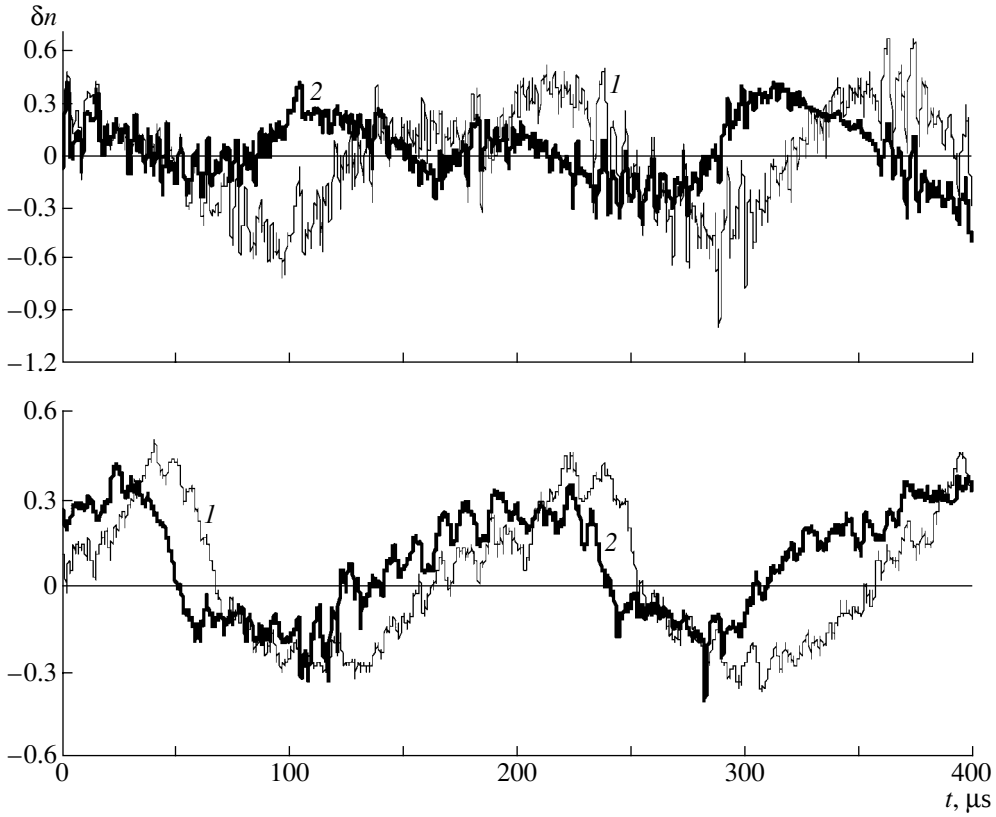

Fig. 9. Signals from the (*1*) first and (*2*) second probes. The magnetic field strength is 1.5 Oe (on the top) and 0.5 Oe (on the bottom).

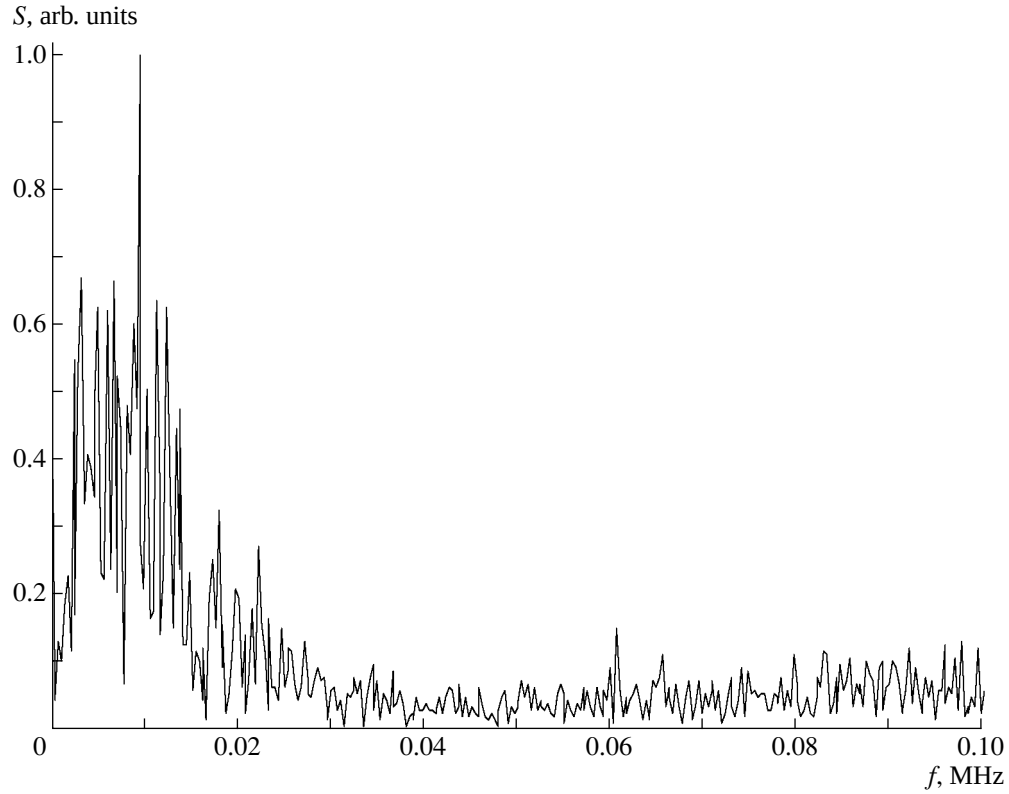

Fig. 10. Spectrum of the plasma density oscillations at a pressure of 6.0×10^{-5} torr.

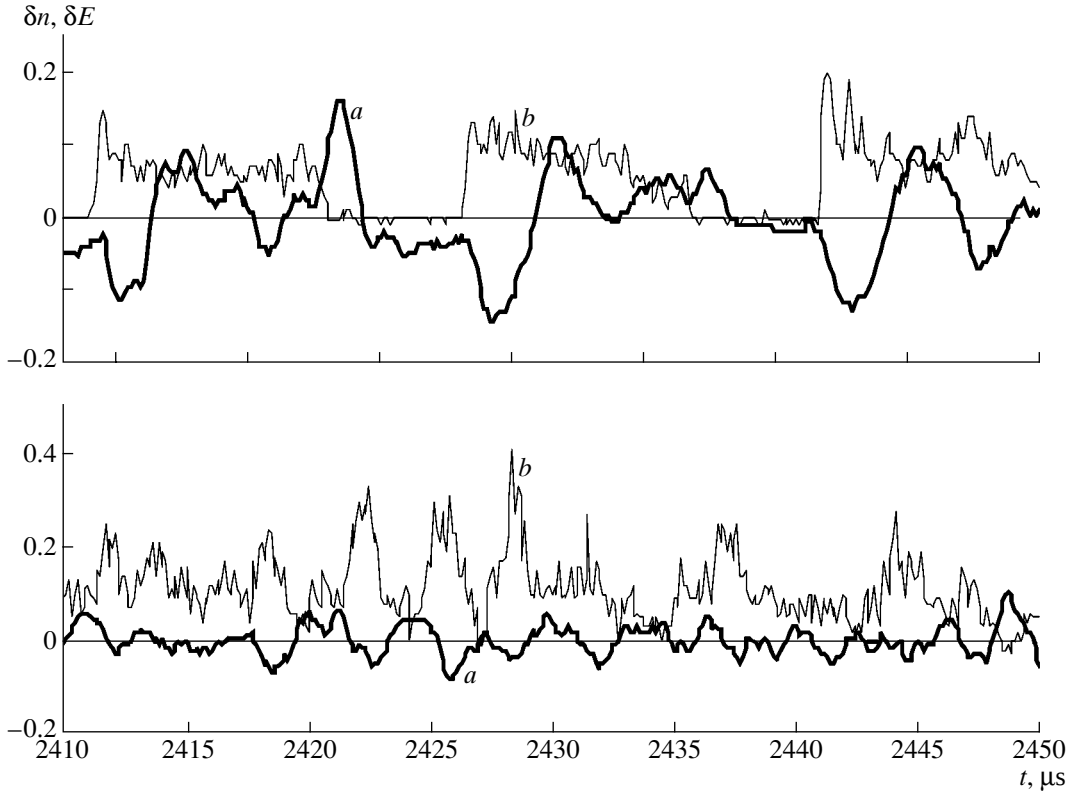

Fig. 11. Waveforms of (*a*) the plasma density variations and (*b*) the wave amplitude in individual peaks in the absence of a BPD at a neutral gas pressure of 6.5×10^{-5} torr (on the top) and 9.5×10^{-5} torr (on the bottom).

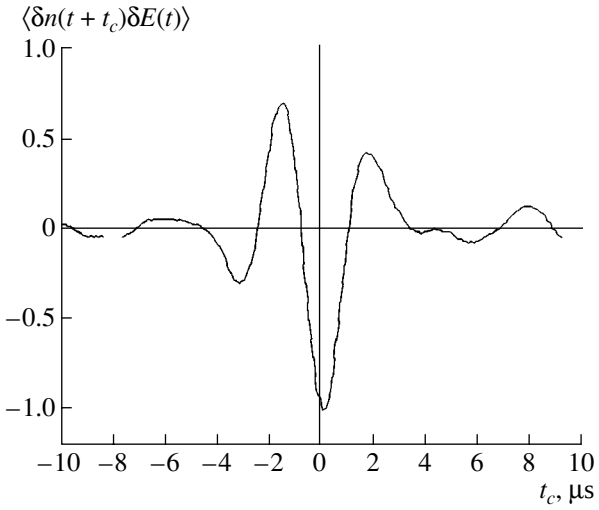

Fig. 12. Cross-correlation function $\langle \delta n(t + t_c)\delta E(t)\rangle$ of the plasma density variations and wave amplitude in the peaks in the absence of a BPD.

nounced second maximum. Based on the above spectral and correlation analyses of the variations in the plasma density and microwave field amplitude, we can conclude that this second maximum is reached at the time at which the discharge terminates. For argon, the density and power values at the second maximum correspond to the second point of intersection of the curve $\tilde{W}_e(0)$ with the dashed line indicating the threshold power above which the BPD can occur (Fig. 4d). In Fig. 13, the theoretical and experimental values obtained for argon are normalized so that this intersection point has the coordinates (1.0, 1.0). The experimental values obtained for helium are normalized so that the second maximum coincides with the point of intersection of the theoretical curve with the corresponding threshold power level. Hence, the horizontal and vertical axes in Fig. 13 are, respectively, the normalized pressure P_* and normalized density W_*. Each of the two experimental curves is matched to the theoretical curve only at one point denoted by large circles *a* and *b*. Since the theoretical curve was calculated for a regime without a BPD, it should be compared with the experimental curves only in the regions that lie below the corresponding threshold power.

According to Fig. 13, the theoretically predicted decrease in the mean output power of a microwave due to the dynamic nature of the amplification regime [see

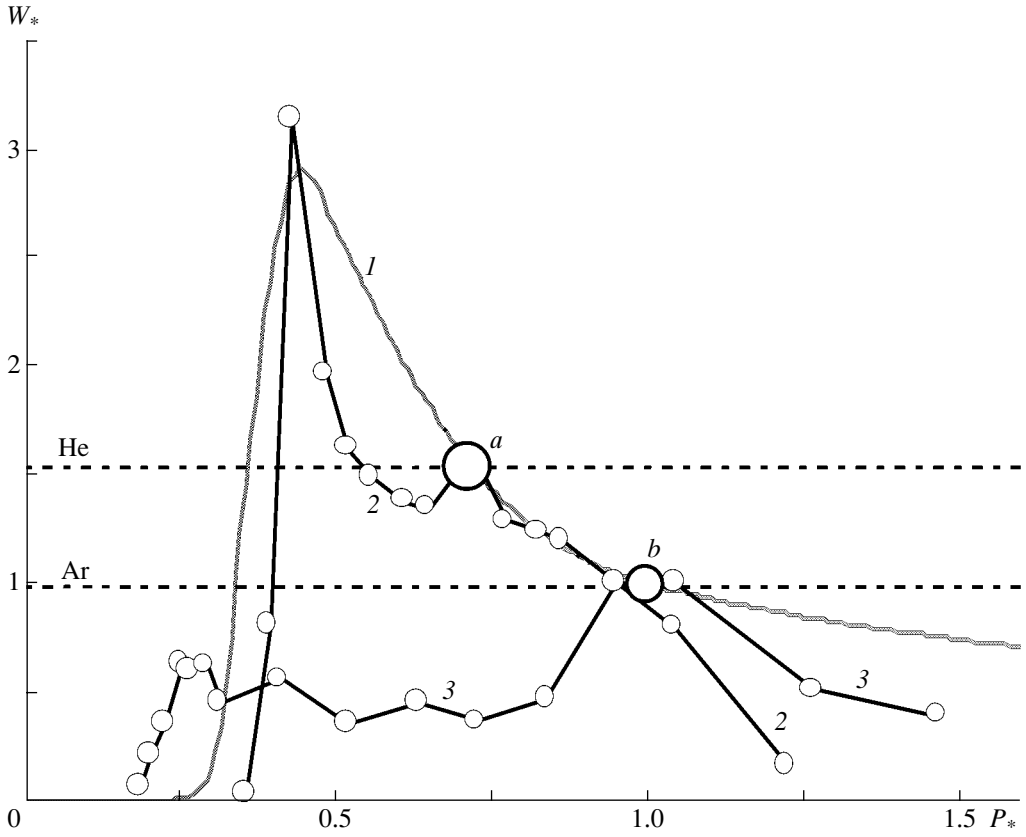

Fig. 13. Pressure dependence of the power of the beam-generated microwaves, calculated theoretically (curve *1*) and measured in experiments with He (curve *2*) and Ar (curve *3*). The dashed lines indicate the threshold powers above which the BPD can occur in the gases indicated. The large circles *a* and *b* denote the points at which the experimental curves are matched to the theoretical curve.

formula (41)] is confirmed by experiment. Note also that the mean output power decreases sharply as the plasma density increases; this is attributed to the fact that the BPI in a magnetized plasma waveguide is highly sensitive to the microwave ponderomotive forces (in Fig. 4d, the parameter Λ is large). Figure 13 demonstrates that, in view of the simplifying assumptions that were made in constructing the theory and also of the minimum number of adjustable parameters used to fit the experimental data, the agreement of the calculated curve with the measured ones may be regarded as satisfactory.

6. CONCLUSION

The above theoretical estimates show that the effect of the plasma nonlinearity is significant even when the beam current is low and, accordingly, the amplitude of the oscillations generated by the beam is small. This is attributed the resonant nature of the interaction between the beam and the wave. In a number of problems concerning the propagation of a wave in a nonlinear medium, the nonlinearity parameter is the ratio of the wave-induced variations in the parameters of the medium to their unperturbed values. In contrast, in the theory developed here, the nonlinearity parameter is the ratio of the variations in the parameters of the medium to the permissible variations that do not violate the synchronization between the wave and the beam electrons. The parameter Λ is just such a nonlinearity parameter. Of course, the specific form of the nonlinearity parameter depends on the dominant mechanism for nonlinearity (microwave pressure, microwave breakdown, etc.), but its physical meaning is always the same.

Here, we have investigated only one mechanism for nonlinearity, specifically, that associated with the microwave ponderomotive force. This mechanism has been chosen because it can be analyzed in a relatively simple way, by making the number of parameters of the problem as small as possible. In the problem in which the main mechanism responsible for nonlinearity is, e.g., microwave breakdown of a neutral gas, the number of parameters is larger because it is necessary to take into account such factors as the threshold ionization energy, the energy dependence of the ionization cross section, and the complicated interrelationship between the transverse distributions of the plasma density and plasma-producing microwave fields (see the above brief discussion). These factors substantially complicate the task of providing a self-consistent description of the BPI under BPD conditions. It is, however, very important to have such a description, because the design of plasma-filled microwave devices in which the plasma is produced exclusively by the beam turns out to be considerably simpler. This problem will be discussed in a future paper.

In the experiments under discussion, a beam was injected into a neutral gas whose pressure was varied over a wide range. It was only over small portions at the ends of this range that the BPD did not occur. Consequently, these are the only portions over which the microwave ponderomotive force can be regarded as a single mechanism for the plasma nonlinearity. Over a wide pressure range, both of the mechanisms—the microwave ponderomotive force and microwave discharge—operate simultaneously. Nevertheless, the effects predicted theoretically, namely, a strong low-frequency self-modulation of the plasma density and wave amplitude, the generation of large-amplitude ion acoustic waves, and a decrease in the power of the excited wave with increasing gas density, were observed experimentally over the entire pressure range. This allows us to suggest that the microwave ponderomotive force is the dominant mechanism for the onset of low-frequency plasma density oscillations even under the BPD conditions.

As for the much faster variations in the plasma density and the amplitude of the excited waves (the peaks), their nature is governed by processes other than those described above. A description of these processes is beyond the scope of the theory proposed here. One possible mechanism for the onset of the peaks is associated with the radial plasma motion accompanied by the perturbations of the guiding longitudinal magnetic field. The perturbations may be driven by the microwave ponderomotive force or the rapid increase in the plasma density during the onset of a microwave discharge. The characteristic time scale on which the magnetic field perturbations are generated is determined by the magnetosonic speed, which is significantly higher than the speed of the ion acoustic waves considered in our study. Thus, in a system with the above parameters, the time the magnetosonic wave takes to cross the plasma is several tenths of a microsecond, while the characteristic time scale on which the peaks develop is about a microsecond. However, this coincidence between the characteristic time scales is still insufficient to precisely attribute the onset of the peaks to the transverse plasma motion.

Finally, we have determined and investigated the mechanism for the onset of a low-frequency self-modulation of the plasma density and the amplitude of a beam-generated wave. The results of our study will help to develop methods for suppressing the associated beam–plasma instability. This problem is extremely important for advancing plasma microwave electronics.

ACKNOWLEDGMENTS

This work was supported in part by the Ukrainian Center for Science and Technology (project no. 277) and the Center for Absorption in Science, Ministry of Immigrant Absorption, State of Israel.

REFERENCES

1. Yu. V. Tkach, Ya. B. Fainberg, I. I. Magda, *et al.*, Fiz. Plazmy **1**, 81 (1975) [Sov. J. Plasma Phys. **1**, 43 (1975)].

2. M. V. Kuzelev, F. Kh. Mukhametzyanov, M. S. Rabinovich, *et al.*, Zh. Éksp. Teor. Fiz. **83**, 1358 (1982) [Sov. Phys. JETP **56**, 780 (1982)].
3. Y. Carmel, K. Minami, R. A. Kehs, *et al.*, Phys. Rev. Lett. **62**, 2389 (1989).
4. Yu. P. Bliokh, E. A. Kornilov, L. A. Mitin, and Ya. B. Fainberg, Fiz. Plazmy **20**, 767 (1994) [Plasma Phys. Rep. **20**, 690 (1994)].
5. M. A. Zavjalov, L. A. Mitin, and V. I. Perevodchikov, IEEE Trans. Plasma Sci. **22**, 600 (1994).
6. V. S. Antipov, A. N. Antonov, V. A. Balakirev, *et al.*, in *Proceedings of the 12th International Conference on High-Power Particle Beams, Haifa, 1998*, Vol. II, p. 699.
7. A. N. Antonov, Yu. P. Bliokh, E. A. Kornilov, *et al.*, Fiz. Plazmy **26**, 1097 (2000) [Plasma Phys. Rep. **26**, 1027 (2000)].
8. A. N. Antonov, Yu. P. Bliokh, E. A. Kornilov, *et al.*, Fiz. Plazmy **27**, 268 (2001) [Plasma Phys. Rep. **27**, 251 (2001)].
9. M. A. Miller, Izv. Vyssh. Uchebn. Zaved., Radiofiz. **1** (3), 110 (1958).
10. Yu. P. Bliokh, M. G. Lyubarsky, I. N. Onishchenko, *et al.*, Dokl. Akad. Nauk Ukr. SSR, Ser. A, No. 11, 55 (1990).
11. Yu. P. Bliokh, M. G. Lyubarsky, I. N. Onishchenko, *et al.*, Fiz. Plazmy **20**, 757 (1994) [Plasma Phys. Rep. **20**, 681 (1994)].
12. N. S. Ginzburg and S. P. Kuznetsov, in *Relativistic High-Frequency Electronics* (Inst. Prikl. Fiz. Akad. Nauk SSSR, Gorki, 1981), p. 101.
13. Yu. P. Bliokh, Ya. B. Fainberg, M. G. Lyubarsky, *et al.*, Phys. Plasmas **5**, 4061 (1998).
14. Yu. P. Bliokh, M. G. Lyubarsky, G. S. Nusinovich, and V. O. Podobinsky, Izv. Vyssh. Uchebn. Zaved., Prikl. Nelineinaya Dinamika **7** (2–3), 56 (1999).
15. I. V. Loshkov, Fiz. Plazmy **3**, 577 (1977) [Sov. J. Plasma Phys. **3**, 326 (1977)].
16. Yu. P. Bliokh, A. V. Borodkin, M. G. Lyubarsky, *et al.*, Izv. Vyssh. Uchebn. Zaved., Prikl. Nelineinaya Dinamika **1** (1–2), 34 (1993).
17. G. B. Whitham, Proc. R. Soc. London A **299** (1456), 6 (1967).
18. I. N. Onishchenko, A. R. Linetskiĭ, N. G. Matsiborko, *et al.*, Pis'ma Zh. Éksp. Teor. Fiz. **12** (8), 407 (1970) [JETP Lett. **12**, 281 (1970)].
19. V. B. Krasovitskiĭ and L. A. Mitin, Fiz. Plazmy **23**, 230 (1997) [Plasma Phys. Rep. **23**, 209 (1997)].
20. K. Yu. Bliokh, Radiofiz. Radioastron. **3** (1), 49 (1998).
21. V. L., Ginzburg, *The Propagation of Electromagnetic Waves in Plasmas* (Nauka, Moscow, 1967; Pergamon Press, Oxford, 1970).
22. K. Yu. Bliokh, Yu. P. Bliokh, M. G. Lyubarsky, and V. O. Podobinsky, Izv. Vyssh. Uchebn. Zaved., Prikladnaya Nelineĭnaya Dinamika **7** (1), 29 (1999).

Translated by O.E. Khadin

Plasma Physics Reports, Vol. 29, No. 4, 2003, pp. 328–345. Translated from Fizika Plazmy, Vol. 29, No. 4, 2003, pp. 357–375.

PLASMA INSTABILITY

Long-Wavelength Instability of Periodic Flows and Helicon Waves in Electron Magnetohydrodynamics

V. P. Lakhin* and V. D. Levchenko**

**Nuclear Fusion Institute, Russian Research Centre Kurchatov Institute, pl. Kurchatova 1, Moscow, 123182 Russia*

***Keldysh Institute of Applied Mathematics, Russian Academy of Sciences, Miusskaya pl. 4, Moscow, 125047 Russia*

Received August 20, 2002

Abstract—The stability of periodic flows and helicon waves against large-scale perturbations is investigated analytically in resistive electron magnetohydrodynamics by the method of two-scale expansions. It is shown that long-wavelength perturbations of a Kolmogorov-type flow are destabilized by the effect of negative resistivity. The destabilization of long-wavelength perturbations of a Beltrami-type helical flow and helicon waves is related to the microhelicity of the primary flow (wave). The instability of long-wavelength perturbations of an anisotropic helical flow is found to result from both the effect of negative resistivity and the effect associated with the microhelical nature of the flow. The criteria for the onset of the corresponding instabilities are derived. Numerical simulations are carried out based on nonlinear electron magnetohydrodynamic equations with initial conditions corresponding to the analytic formulation of the problem. The results of simulations on the whole confirm analytical results in the parameter range in which the latter are applicable and, in addition, extend the stability analysis to the parameter ranges that are beyond the scope of analytic approximations. *© 2003 MAIK "Nauka/Interperiodica".*

1. INTRODUCTION

It is well known that periodic flows in a viscous fluid can be unstable against long-wavelength perturbations. The simplest example is a two-dimensional Kolmogorov flow in a viscous incompressible fluid [1–5]. It was shown that, at a certain critical velocity, the Kolmogorov flow becomes unstable against long-wavelength perturbations. The instability mechanism is the effect of the negative viscosity on long-wavelength perturbations due to a small-scale periodic flow. A similar instability occurs for Rossby waves (a sort of wave motion widely encountered in the atmosphere and the oceans) and for drift waves in a magnetized plasma [6]. The resemblance is so close that even the instability criteria for a sinusoidal drift wave (a Rossby wave) and for a sinusoidal Kolmogorov flow, both of which are sustained by a steady external source, are the same: the instability occurs under the condition $Re > \sqrt{2}$, where Re is the Reynolds number of a periodic flow (wave).

Another example of an unstable hydrodynamic flow is a three-dimensional Beltrami helical flow [4, 7, 8]. It was shown that the dispersion relation for long-wavelength perturbations of a Beltrami flow is similar to that for the perturbations of a Kolmogorov flow. Being unstable, the periodic flows and waves mentioned above can give rise to large-scale coherent structures, which attract interest because of their possible roles in various physical phenomena, such as enhanced transport (in comparison with the molecular transport) in fluids, anomalous transport of particles and energy in a plasma, and self-organization processes. A weakly nonlinear stage of the evolution of the instability-driven large-scale perturbations of a Kolmogorov flow was studied both analytically and by numerical modeling in [9, 10]. The same investigations for drift waves were carried out in [6]. In particular, these three papers demonstrated that dissipative solitons and zonal dissipative structures can in fact form.

In the present paper, the stability of periodic flows and helicon waves (helicons) against long-wavelength perturbations is studied within the framework of dissipative electron magnetohydrodynamics (EMHD). The EMHD equations describe small-scale ($l < c/\omega_{pi}$) phenomena on time scales $1/\omega_{Be} < t < 1/\omega_{Bi}$, where ω_{pi} is the ion Langmuir frequency and ω_{Be} and ω_{Bi} are the electron and ion gyrofrequencies, respectively. Such phenomena play important roles in systems with intense drift electron motion across the magnetic field, e.g., in Z-pinches, erosive plasma switches, laser-produced coronas [11], and possibly in tokamaks during strong electron cyclotron resonance heating [12]. The EMHD equations are also used to describe an electron–hole plasma in an uncompensated semiconductor in a magnetic field [13].

Assuming that a continuously operating external source (or certain primary instabilities) gives rise to a periodic flow (a helicon) whose amplitude is maintained constant by the source, we investigate the stability of the flow (helicon) against large-scale perturbations (secondary instabilities). Following the cited papers, we analyze the stability of periodic solutions to the EMHD equations by the method of two-scale expansions, which is justified provided that the charac-

1063-780X/03/2904-0328$24.00 © 2003 MAIK "Nauka/Interperiodica"

teristic spatial scales of the main periodic flow (helicon) are small in comparison with the wavelength of the perturbations.

Also, we present the results of solving the nonlinear EMHD equations numerically with the initial parameter values corresponding to the instability region obtained analytically. The numerical solutions, on the one hand, may serve to justify analytical results and, on the other, make it possible to draw conclusions about the stability of the modes in the parameter ranges that are beyond the scope of analytic approximations.

Our paper is organized as follows. In Section 2, we introduce the EMHD equations, briefly discuss the range of their applicability, and describe the method for solving them numerically. In Section 3, we analyze the stability of steady-state periodic EMHD flows. We separately consider three types of flows: a Kolmogorov-like flow, a Beltrami-type helical flow, and a flow that will be referred to as an anisotropic helical flow. Also, for each of the flows, we present the results of numerical simulations of the corresponding instabilities. In Section 4, we give a detailed analysis of the stability of a helicon against large-scale perturbations. Finally, in Section 5, we summarize the results obtained and make final remarks.

2. BASIC EMHD EQUATIONS AND THE METHOD FOR SOLVING THEM NUMERICALLY

On the spatial and time scales mentioned in the introduction, the electrons can be described in the hydrodynamic approximation, while the ions can be treated as an immobile background. It is well known that, when the background plasma is homogeneous (n_0 = const), the plasma perturbations are quasineutral (i.e., the electron density remains unperturbed), and the finite electron Larmor radius effects are negligible, the EMHD equations have the form (see, e.g., [14, 15])

$$\frac{\partial}{\partial t}\nabla\times\left(m_e\mathbf{v}_e-\frac{e}{c}\mathbf{A}\right) = \nabla\times\left[\mathbf{v}_e\times\left(\nabla\times\left(m_e\mathbf{v}_e-\frac{e}{c}\mathbf{A}\right)\right)\right]+\frac{e}{\sigma}\nabla\times\mathbf{j}, \tag{1}$$

where $\mathbf{A}$ is the vector potential, $\nabla\times\mathbf{A}=\mathbf{B}$, and $\sigma = e^2n_0\tau_e/m_e$ is the plasma conductivity. In the limiting case of a plasma with infinite conductivity, Eq. (1) implies that the curl of the generalized momentum is frozen in the electron fluid. Taking into account the fact that, in our problem, the electric current is carried by the electrons and neglecting the displacement current (i.e., setting $\nabla\times\mathbf{B}=(4\pi/c)\mathbf{j}$ in Maxwell's equation), we obtain

$$\mathbf{v}_e = -\mathbf{j}/en_0 = -c\nabla\times\mathbf{B}/4\pi en_0. \tag{2}$$

As a result, in the simplest case described above, the EMHD equations reduce to the following evolutionary equation for the magnetic field:

$$\frac{\partial}{\partial t}\left(\mathbf{B}-\frac{c^2}{\omega_{pe}^2}\nabla^2\mathbf{B}\right) = \frac{c}{4\pi en_0}\nabla\times\left[\left(\mathbf{B}-\frac{c^2}{\omega_{pe}^2}\nabla^2\mathbf{B}\right)\times(\nabla\times\mathbf{B})\right]+\frac{c^2}{4\pi\sigma}\nabla^2\mathbf{B}. \tag{3}$$

To simplify further calculations, we rewrite Eq. (3) in dimensionless form and supplement its right-hand side with an external source term:

$$\frac{\partial}{\partial t}(\mathbf{B}-d_e^2\nabla^2\mathbf{B}) = \nabla\times[(\mathbf{B}-d_e^2\nabla^2\mathbf{B})\times(\nabla\times\mathbf{B})]+\nu\nabla^2\mathbf{B}+\mathbf{f}. \tag{4}$$

Here, the spatial variables are normalized to the quantity $l=\lambda/2\pi\equiv 1/k_0$, where λ is the wavelength of the primary periodic flow (helicon); the time is normalized to the so-called helicon time $t_0=\omega_{Be}^{-1}(l\omega_{pe}/c)^2$, which can be interpreted as the characteristic inverse helicon frequency; the magnetic field is normalized to the characteristic flow field in the case of a periodic flow or to the external magnetic field in the case of helicons; $d_e = c/\omega_{pe}l$ is the normalized electron collisionless skin depth; and $\nu = 1/\omega_{Be}\tau_e$. It is worth noting that, in the case of a periodic flow, the quantity $1/\nu\equiv Re_m$ is the characteristic magnetic Reynolds number, which serves as a measure of the ratio of the nonlinear term to the resistive term in Eq. (3). As we have already stated, in further analysis, the role of the external source term $\mathbf{f}$ in Eq. (4) is to keep the amplitude of the primary periodic flow (helicon) constant; the explicit form of the source term in different cases will be discussed below.

For a plasma with infinite conductivity ($\sigma\longrightarrow\infty$) in a constant external magnetic field $\mathbf{B}_0=B_0\mathbf{e}_z$, Eq. (3) admits solutions describing nontrivial linear waves called helicons (also known as whistlers). The well-known dispersion relation for helicons has the form

$$\omega = \pm\frac{\omega_{Be}kk_zc^2}{\omega_{pe}^2(1+k^2c^2/\omega_{pe}^2)}, \tag{5}$$

where $\mathbf{k}$ is the wave vector of the helicon and ω is its frequency. In Section 4, we discuss helicons in more detail.

In the next sections, Eq. (4) is used as a basic equation for analytic investigations of the stability of periodic EMHD flows (helicons) against long-wavelength perturbations by the method of multiscale expansions. In order to illustrate the correctness of the analytic approximations chosen for our analysis and to generalize the results obtained theoretically to the parameter ranges that are beyond the scope of the approximations,

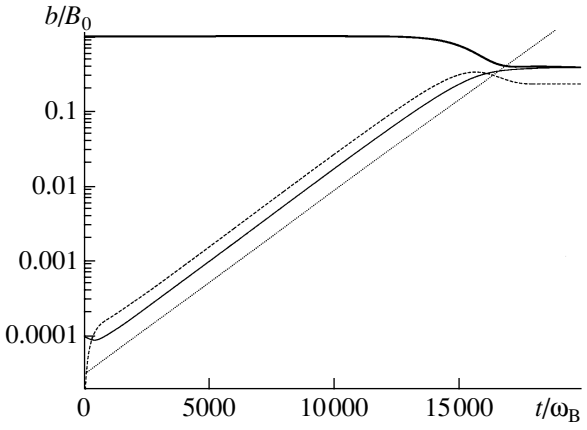

Fig. 1. Time evolution of the amplitudes of the chosen modes: **k** (heavy line), **q** (light line), **k** + **q** (dashed line). The exponential growth of the mode with the amplitude **q** is shown by the dotted line.

we also present the results of solving Eq. (4) numerically. In numerical simulations, Eq. (4), which is regarded as an evolutionary equation for the function

$$\mathbf{F} = \mathbf{B} - d_e^2 \nabla^2 \mathbf{B}, \tag{6}$$

was integrated layer by layer in time with a time step Δ^t by the fourth-order Runge–Kutta method. The right-hand side of Eq. (4) was approximated using centered finite-difference operators of second-order accuracy in space on shifted numerical grids. The magnetic field **B**, which is implicitly contained in Eq. (6), was calculated from the Fourier transform of this equation.

Our simulations were aimed at investigating the stability of the chosen mode (with the wave vector **q**) of long-wavelength perturbations in the presence of a short-wavelength periodic flow (with the wave vector **k**) sustained by an external source. That is why the boundary conditions were chosen to be periodic in each of the three coordinate directions in the three-dimensional spatial region $L^x \times L^y \times L^z$ under consideration. The sizes L^x, L^y, and L^z were chosen to be equal to an integral number of wavelengths (usually, one wavelength) of the mode in question. The grid was uniform in each of the coordinates, the number of mesh points being 32 or 64 per wavelength. The total number of the mesh points of the grid was from thirty-two thousand to one million, and the total number of time steps was from one to ten thousand.

The initial conditions for the magnetic field **B** and the source term **f** were chosen to be consistent with the steady-state flow under study. In addition, the total magnetic field at the initial time was assumed to be a superposition of the field $\mathbf{B}^0$ of a steady-state flow and a small long-wavelength solenoidal (i.e., satisfying the condition $\nabla \cdot \mathbf{b} = 0$ ($\mathbf{q} \cdot \mathbf{b} = 0$)) perturbation **b** with the amplitude $b \le 10^{-4} B^0$.

In each run, the amplitudes of the chosen modes, namely, **k**, **q**, and $\mathbf{k} \pm \mathbf{q}$, were calculated at each time step and were stored for further analysis. The representative time evolutions of the amplitudes are shown in Fig. 1. When the mode amplitude **q** was found to increase exponentially with time, we calculated the instability growth rate γ from the linear (on a logarithmic scale) portion of the corresponding curve. After performing a series of simulations for different parameter values, we could determine how the growth rate so obtained depends on the parameters of interest to us.

It should be noted that the remaining harmonics of the magnetic field **B** that conform to the above periodic boundary conditions (i.e., the field harmonics such that the period of the system is exactly equal to an integer number of their wavelengths) evolve self-consistently in accordance with nonlinear equation (4). However, the initial amplitudes of these harmonics are about the round-off errors in computations ($b/B_0 \sim 10^{-16}$) and usually increase insignificantly in the course of a run. On the other hand, in some cases (see Section 3.2), the growth rate of the chosen mode (that with the wave vector **q**) may be lower than the growth rates of the multiple modes. In this case, it becomes more difficult to progress into the parameter range in which the analytic approximations are certainly applicable. In these cases, we restrict ourselves to considering the boundary range of the parameters.

In other respects, the formulation of the numerical problem corresponds as closely as possible to that of the analytical problem, thereby making it possible to compare numerical and analytical results. Moreover, since the procedure for integrating Eq. (4) numerically was developed without making any additional simplifying assumptions, the scope of an analysis of the parameter ranges in which long-wavelength modes are unstable can be extended to the parameter ranges in which the analytic approximations fail.

3. STABILITY OF STEADY-STATE PERIODIC FLOWS

In this Section, we analyze the stability of the three different types of steady-state electron flows mentioned in the introduction, namely, a Kolmogorov-type flow, a Beltrami-type helical flow, and an anisotropic helical flow. In this section, the magnetic field is assumed to be normalized to the magnetic field of the flow.

3.1. Kolmogorov-type Flow

The flow, which is similar to the Kolmogorov flow (see, e.g., [4]),

$$\mathbf{B}^0 = \cos x \mathbf{e}_z, \quad \mathbf{v}_e \propto \nabla \times \mathbf{B}^0 = \sin x \mathbf{e}_y, \tag{7}$$

is an exact stationary solution to Eq. (4) if the external source exactly counterbalances the resistive dissipation of the flow and is described by the term

$$\mathbf{f} = -\nu\nabla^2\mathbf{B}^0 = \nu\cos x\,\mathbf{e}_z. \tag{8}$$

As is the case with a Kolmogorov flow in incompressible hydrodynamics, the electron flow under discussion is two-dimensional: its velocity is directed along the *y*-axis and its amplitude depends solely on the *x* coordinate. In order to consider infinitesimal perturbations of solution (7), we set

$$\mathbf{B} = \mathbf{B}^0 + \mathbf{b}, \quad |\mathbf{b}| \ll |\mathbf{B}^0|. \tag{9}$$

Then, we linearize Eq. (4) with respect to **b** and obtain

$$\begin{aligned}\frac{\partial}{\partial t}(\mathbf{b} - d_e^2\nabla^2\mathbf{b}) &= \nu\nabla^2\mathbf{b} + \sin x\frac{\partial}{\partial y}(\mathbf{b} - d_e^2\nabla^2\mathbf{b})\\ &\quad - \cos x(b_x - d_e^2\nabla^2 b_x)\mathbf{e}_y\\ &\quad - (1 + d_e^2)\left\{\sin x(\mathbf{e}_x\cdot[\nabla\times\mathbf{b}])\mathbf{e}_z + \cos x\frac{\partial}{\partial z}\nabla\times\mathbf{b}\right\}.\end{aligned} \tag{10}$$

We seek solutions to Eq. (10) in two cases: when ν is on the order of unity (a small magnetic Reynolds number, $Re_m \simeq 1$) and for $\nu \ll 1$ (a large but finite magnetic Reynolds number, $Re_m \gg 1$).

3.1.1. The case of a small magnetic reynolds number. We assume that the perturbations occur on a spatial scale $O(\epsilon^{-1})$ and a time scale $O(\epsilon^{-2})$, where $\epsilon \ll 1$ is a small parameter. Under this assumption, which is justified by the results obtained below, Eq. (10) can be solved by applying the formalism of multiscale expansions; in the case at hand, this is a two-scale expansion in the fast variable *x* and the slow variables

$$T = \epsilon^2 t, \quad Y = \epsilon y, \quad Z = \epsilon z. \tag{11}$$

We are interested in the solution that is a periodic function of *x* and depends on the slow variables:

$$\mathbf{b} = \mathbf{b}(x, Y, Z, T) = \mathbf{b}(x + 2\pi, Y, Z, T). \tag{12}$$

In the new variables, the components of Eq. (10) have the form

$$\begin{aligned}\epsilon^2\frac{\partial}{\partial T}\left(b_x - d_e^2\frac{\partial^2 b_x}{\partial x^2} - \epsilon^2 d_e^2\nabla_s^2 b_x\right) &= \nu\left(\frac{\partial^2 b_x}{\partial x^2} + \epsilon^2\nabla_s^2 b_x\right)\\ &\quad + \epsilon\sin x\frac{\partial}{\partial Y}\left(b_x - d_e^2\frac{\partial^2 b_x}{\partial x^2} - \epsilon^2 d_e^2\nabla_s^2 b_x\right)\\ &\quad - \epsilon^2\cos x(1 + d_e^2)\frac{\partial}{\partial Z}\left(\frac{\partial b_z}{\partial Y} - \frac{\partial b_y}{\partial Z}\right),\end{aligned} \tag{13}$$

$$\begin{aligned}\epsilon^2\frac{\partial}{\partial T}\left(b_y - d_e^2\frac{\partial^2 b_y}{\partial x^2} - \epsilon^2 d_e^2\nabla_s^2 b_y\right) &= \nu\left(\frac{\partial^2 b_y}{\partial x^2} + \epsilon^2\nabla_s^2 b_y\right)\\ &\quad + \epsilon\sin x\frac{\partial}{\partial Y}\left(b_y - d_e^2\frac{\partial^2 b_y}{\partial x^2} - \epsilon^2 d_e^2\nabla_s^2 b_y\right)\\ &\quad - \cos x\left(b_x - d_e^2\frac{\partial^2 b_x}{\partial x^2} - \epsilon^2 d_e^2\nabla_s^2 b_x\right)\\ &\quad - \epsilon\cos x(1 + d_e^2)\frac{\partial}{\partial Z}\left(\epsilon\frac{\partial b_x}{\partial Z} - \frac{\partial b_z}{\partial x}\right),\end{aligned} \tag{14}$$

$$\begin{aligned}\epsilon^2\frac{\partial}{\partial T}\left(b_z - d_e^2\frac{\partial^2 b_z}{\partial x^2} - \epsilon^2 d_e^2\nabla_s^2 b_z\right) &= \nu\left(\frac{\partial^2 b_z}{\partial x^2} + \epsilon^2\nabla_s^2 b_z\right)\\ &\quad + \epsilon\sin x\frac{\partial}{\partial Y}\left(b_z - d_e^2\frac{\partial^2 b_z}{\partial x^2} - \epsilon^2 d_e^2\nabla_s^2 b_z\right)\\ &\quad - \epsilon(1 + d_e^2)\left\{\sin x\left(\frac{\partial b_z}{\partial Y} - \frac{\partial b_y}{\partial Z}\right) + \cos x\frac{\partial}{\partial Z}\left(\frac{\partial b_y}{\partial x} - \epsilon\frac{\partial b_x}{\partial Y}\right)\right\},\end{aligned} \tag{15}$$

where $\nabla_s^2 \equiv \partial^2/\partial Y^2 + \partial^2/\partial Z^2$. For further analysis, it is expedient to average Eqs. (13)–(15) over the period of the fast variable *x*. Introducing the definition

$$\langle\ldots\rangle = \frac{1}{2\pi}\int_0^{2\pi}(\ldots)dx, \tag{16}$$

we arrive at the equations

$$\begin{aligned}\epsilon^2\frac{\partial}{\partial T}(\langle b_x\rangle - \epsilon^2 d_e^2\nabla_s^2\langle b_x\rangle) &= \epsilon^2\nu\nabla_s^2\langle b_x\rangle + \epsilon\{1 + d_e^2 - \epsilon^2 d_e^2\nabla_s^2\}\frac{\partial}{\partial Y}\langle b_x\sin x\rangle\\ &\quad - \epsilon^2(1 + d_e^2)\frac{\partial}{\partial Z}\left\{\frac{\partial}{\partial Y}\langle b_z\cos x\rangle - \frac{\partial}{\partial Z}\langle b_y\cos x\rangle\right\},\end{aligned} \tag{17}$$

$$\begin{aligned}\epsilon^2\frac{\partial}{\partial T}(\langle b_y\rangle - \epsilon^2 d_e^2\nabla_s^2\langle b_y\rangle) &= \epsilon^2\nu\nabla_s^2\langle b_y\rangle\\ &\quad + \{1 + d_e^2 - \epsilon^2 d_e^2\nabla_s^2\}\left\{\epsilon\frac{\partial}{\partial Y}\langle b_y\sin x\rangle - \langle b_x\cos x\rangle\right\}\\ &\quad - \epsilon(1 + d_e^2)\frac{\partial}{\partial Z}\left\{\epsilon\frac{\partial}{\partial Z}\langle b_x\cos x\rangle - \langle b_z\sin x\rangle\right\},\end{aligned} \tag{18}$$

$$\begin{aligned}\epsilon^2\frac{\partial}{\partial T}(\langle b_z\rangle - \epsilon^2 d_e^2\nabla_s^2\langle b_z\rangle) &= \epsilon^2\nu\nabla_s^2\langle b_z\rangle\\ &\quad - \epsilon^3 d_e^2\frac{\partial}{\partial Y}\nabla_s^2\langle b_z\sin x\rangle + \epsilon^2(1 + d_e^2)\frac{\partial^2}{\partial Y\partial Z}\langle b_x\cos x\rangle.\end{aligned} \tag{19}$$

To within terms of the corresponding order in an expansion in the small parameter ϵ, these equations ensure that Eqs. (13)–(15) have solutions in the class of functions periodic in x. Equation (18) can be further simplified by using the equalities

$$\langle b_x \cos x\rangle - \epsilon\frac{\partial}{\partial Y}\langle b_y \sin x\rangle - \epsilon\frac{\partial}{\partial Z}\langle b_z \sin x\rangle = 0, \quad (20)$$

$$\langle b_x \sin x\rangle + \epsilon\frac{\partial}{\partial Y}\langle b_y \cos x\rangle + \epsilon\frac{\partial}{\partial Z}\langle b_z \cos x\rangle = 0, \quad (21)$$

which are obtained by multiplying the equation $\nabla \cdot \mathbf{b} = 0$ by $\sin x$ and $\cos x$, respectively, and by integrating the resulting equations over the period of the fast variable x. Substituting Eq. (20) into Eq. (18) reduces the latter to a form similar to that of Eq. (19):

$$\epsilon^2\frac{\partial}{\partial T}(\langle b_y\rangle - \epsilon^2 d_e^2 \nabla_s^2\langle b_y\rangle) = \epsilon^2\nu\nabla_s^2\langle b_y\rangle + \epsilon^3 d_e^2\frac{\partial}{\partial Z}\nabla_s^2\langle b_z \sin x\rangle - \epsilon^2(1+d_e^2)\frac{\partial^2}{\partial Z^2}\langle b_x \cos x\rangle. \quad (22)$$

A direct averaging of the equation $\nabla \cdot \mathbf{b} = 0$ yields the following useful equation:

$$\epsilon\frac{\partial\langle b_y\rangle}{\partial Y} + \epsilon\frac{\partial\langle b_z\rangle}{\partial Z} = 0, \quad (23)$$

which will be often employed in further analysis and, in this section, will allow us to check the consistency of final averaged equations (19) and (22) with the condition that the averaged magnetic field of the perturbations is incompressible.

We look for a solution to Eqs. (13)–(15) in the form of an asymptotic expansion in powers of the small parameter ϵ:

$$\mathbf{b} = \mathbf{b}^{(0)} + \epsilon\mathbf{b}^{(1)} + \epsilon^2\mathbf{b}^{(2)} + \ldots. \quad (24)$$

We assume that the parameter ν is finite ($\nu \simeq 1$). Also, in this and subsequent sections, we restrict our analysis to perturbations occurring on a characteristic spatial scale larger than the electron collisionless skin depth, $d_e^2|\nabla_s^2| \simeq 1$. Then, to zeroth order in the parameter ϵ, we obtain

$$\nu\frac{\partial^2 b_x^{(0)}}{\partial x^2} = \nu\frac{\partial^2 b_z^{(0)}}{\partial x^2} = 0,$$
$$\nu\frac{\partial^2 b_x^{(0)}}{\partial x^2} - \cos x\left(b_x^{(0)} - d_e^2\frac{\partial^2 b_x^{(0)}}{\partial x^2}\right) = 0. \quad (25)$$

Solving Eq. (25) yields

$$b_x^{(0)} = b_{sx}^{(0)}, \quad b_y^{(0)} = b_{sy}^{(0)} - \frac{1}{\nu}b_{sx}^{(0)}\cos x, \quad b_z^{(0)} = b_{sz}^{(0)}, \quad (26)$$

where $\mathbf{b}_s^{(0)}$ is an arbitrary function of the slow variables, $\mathbf{b}_s^{(0)} = \mathbf{b}_s^{(0)}(Y, Z, T)$. From Eqs. (17), (19), and (22), it is seen that, among the terms on their right-hand sides that describe the interaction of a long-wavelength perturbation with the initial periodic flow, only the terms in Eq. (17) make a nonzero contribution on the order of ϵ^2. Substituting solution (26) into Eqs. (17), (19), and (22) yields the equations

$$\frac{\partial b_{sx}^{(0)}}{\partial T} = \nu\nabla_s^2 b_{sx}^{(0)} - \frac{1}{2\nu}(1+d_e^2)\left(\frac{\partial^2}{\partial Z^2} - \frac{\partial^2}{\partial Y^2}\right)b_{sx}^{(0)},$$
$$\frac{\partial b_{sy}^{(0)}}{\partial T} = \nu\nabla_s^2 b_{sy}^{(0)}, \quad \frac{\partial b_{sz}^{(0)}}{\partial T} = \nu\nabla_s^2 b_{sz}^{(0)}, \quad (27)$$

which are seen to justify assumption (11). Also, Eqs. (20) and (26) imply that nonzero contributions of the interaction of the perturbation with a periodic flow to the evolutionary equation for the averaged components $\langle b_y\rangle$ and $\langle b_z\rangle$ of the long-wavelength magnetic field are on the order of $O(\epsilon^4)$ and that the corresponding terms reflect the effect of viscosity on these components. Equations (27) show that, under certain conditions, the x component of the long-wavelength field becomes unstable because of the interaction with the primary flow. Specifically, setting $b_{sx}^{(0)} \sim \exp(\gamma t + i(q_y Y + q_z Z))$ provides the dispersion relation

$$\gamma = \frac{1}{2\nu}(1+d_e^2)(q_z^2 - q_y^2) - \nu q^2, \quad (28)$$

where $q = \sqrt{q_y^2 + q_z^2}$. This asymptotic dispersion relation is qualitatively analogous to the dispersion relation of the long-wavelength perturbations of a Kolmogorov flow with a finite Reynolds number [1–3]. According to Eq. (28), the most unstable perturbations are those with $q_y = 0$, i.e., perturbations whose wave vector is perpendicular to the propagation direction of the primary flow ($\mathbf{q} \perp \mathbf{v}_e$) and parallel to the magnetic field produced by the flow ($\mathbf{q} \parallel \mathbf{B}^0 \parallel \mathbf{e}_z$). Such perturbations become unstable when the magnetic Reynolds number Re_m becomes larger than a certain critical value:

$$Re_m \equiv 1/\nu > Re_m^{\mathrm{cr}} = \sqrt{\frac{2}{1+d_e^2}}. \quad (29)$$

The instability at hand belongs to a class of instabilities associated with the effect of negative dissipation. The instability mechanism is the effect of the negative resistivity due to the interaction of the perturbation with the primary flow and is described by the second term on the right-hand side of Eq. (27) for $b_{sx}^{(0)}$. The physical explanation of the phenomenon is that, as a result of the interaction, the flow energy cascades toward large scales (an inverse cascade). The remaining y and z com-

ponents of the magnetic field of the perturbation are damped by the plasma resistivity. An analogous effect was recently revealed in [16], where the spontaneous amplification of long-wavelength perturbations by small-scale turbulence was investigated in a 2.5-dimensional collisionless EMHD model. In that paper, it was shown that the effect of negative resistivity takes place when the equipartition of energy among the magnetic field components is absent and the effect is thus governed by the anisotropy of the small-scale EMHD turbulence.

3.1.2. The case of a large magnetic reynolds number. Here, we consider small (but finite) values of ν, $\nu \ll 1$. We introduce a new ordering among the slow variables,

$$t = \nu^3 T, \quad y = \nu^2 Y, \quad z = \nu^2 Z, \tag{30}$$

and solve Eq. (10) by applying the above procedure. As a result, we arrive at the solution

$$b_x^{(0)} = 0, \quad b_x^{(1)} = b_{sx}^{(1)}, \quad b_z^{(0)} = b_{sz}^{(0)}, \quad b_y^{(0)} = b_{sy}^{(0)} - b_{sx}^{(1)} \cos x, \tag{31}$$

where $b_{sx}^{(1)}$, $b_{sy}^{(0)}$, and $b_{sz}^{(0)}$ are functions of the slow variables only. Averaging Eq. (10) over the period of the primary flow yields the following evolutionary equations for these functions:

$$\frac{\partial b_{sx}^{(1)}}{\partial T} = \frac{1}{2}(1 + d_e^2)\left(\frac{\partial^2}{\partial Y^2} - \frac{\partial^2}{\partial Z^2}\right) b_{sx}^{(1)}, \quad \frac{\partial b_{sy}^{(0)}}{\partial T} = O(\nu^2), \quad \frac{\partial b_{sz}^{(0)}}{\partial T} = O(\nu^2). \tag{32}$$

Equations (32) imply that, in contrast to the case of a small magnetic Reynolds number, the x component of the long-wavelength magnetic field enters only in the first order in the expansion parameter. The equations also show that, on the one hand, the functions $b_{sy}^{(0)}$ and $b_{sz}^{(0)}$ remain constant on the time scale $1/\nu^3$ (actually, they are weakly damped on the time scale $1/\nu^5$ because of the plasma resistivity) and, on the other hand, the evolution of the function $b_{sx}^{(1)}$ is analogous to that of $b_{sx}^{(0)}$ in the case of a small magnetic Reynolds number, with the only difference being that, for large magnetic Reynolds numbers, the effect of collisional plasma resistivity is negligible (as small as ν^2 in comparison with the effect due to the interaction of long-wavelength perturbations with the flow). Consequently, the stability analysis carried out in the previous section remains, on the whole, valid. This analysis shows that perturbations with $q_z > q_y$ are unstable and that the instability growth rate is proportional to the magnetic Reynolds number; i.e., it exceeds the growth rate obtained for small magnetic Reynolds numbers in the previous section:

$$\gamma = \frac{1}{2\nu}(1 + d_e^2)(q_z^2 - q_y^2). \tag{33}$$

In deriving Eqs. (32), we used the relationship of the slow variables to the initial variables [see Eq. (30)].

The results of numerical modeling of the stability of a Kolmogorov-type periodic EMHD flow for large magnetic Reynolds numbers are illustrated in Figs. 2–4.

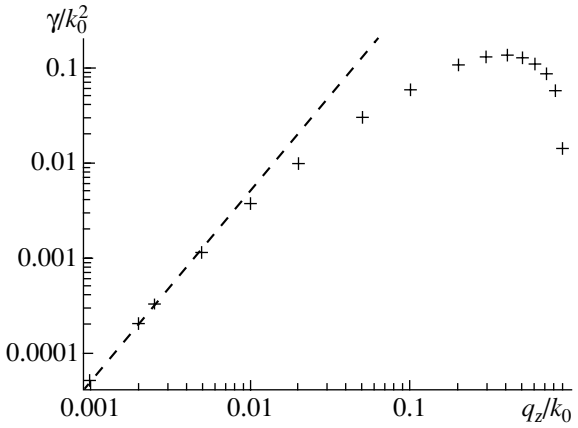

Fig. 2. Growth rate vs. q_z for $d_e = \pi$, $\nu = 0.1$, and $q_y/q_z = 0.01$ in the case of a Kolmogorov-type flow. In this and the next two figures, the crosses present numerical results and the dashed line refer to asymptotic formula (28). In the parameter range of validity of the analytic approximation ($q_z/k_0 < \nu^2$), the numerical and analytical results coincide. At $q_z \approx 0.4k_0$, the growth rate is seen to be maximum, and at $q_z \approx k_0$, the flow becomes stable.

3.2. Beltrami-type Helical Flow

The EMHD equations have another stationary solution that is analogous to a three-dimensional Beltrami flow in incompressible hydrodynamics (see, e.g., [4]):

$$\mathbf{B}^0 = \mathbf{e}_y \sin x + \mathbf{e}_z \cos x. \tag{34}$$

In order for the amplitude of such a flow to be kept constant, the resistive dissipation in Eq. (4) should be balanced by an external source, which, in the case at hand, is described by the equation

$$\mathbf{f} = -\nu \nabla^2 \mathbf{B}^0 = \nu(\mathbf{e}_y \sin x + \mathbf{e}_z \cos x). \tag{35}$$

A flow corresponding to solution (34) is, in essence, a limiting case of helicons with zero frequency and with $k_z = 0$ (see Section 4). The magnetic field of the flow is similar in structure to the helicon magnetic field. Such a flow belongs to the class of force-free equilibrium flows, because it obeys the equation $\nabla \times \mathbf{B}^0 = \mathbf{B}^0$, and is a helical one, because it has a nonzero microhelicity, $\mathbf{B}^0 \cdot (\nabla \times \mathbf{B}^0) = 1$.

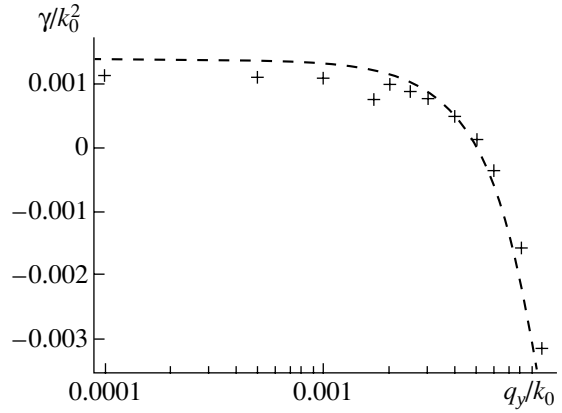

Fig. 3. Growth rate vs. q_y for $d_e = \pi$, $\nu = 0.1$, and $q_z = 0.05$. In accordance with formula (28), referring to the dashed curve, the fastest growing mode is that whose wave vector is parallel to the magnetic field of the flow ($q_y = 0$). As the angle between the wave vector and the magnetic field increases, the mode becomes stable.

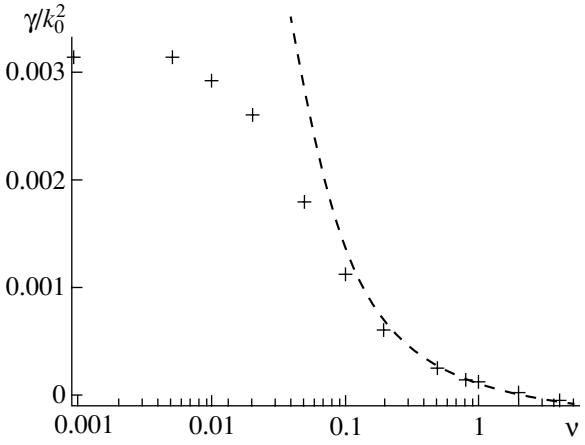

Fig. 4. Growth rate vs. the viscosity ν for $d_e = \pi$, $q_z/k_0 = 0.05$, and $q_y/k_0 = 0.0005$. The flow becomes stable when criterion (29) fails to hold.

As in the previous section, we consider infinitesimal perturbations of a helical flow and use representation (9) for the total magnetic field. Taking into account solution (34), we can write the linearized evolutionary equation for **b** in the form

$$\frac{\partial}{\partial t}(\mathbf{b} - d_e^2\nabla^2\mathbf{b}) = \nabla\times[\mathbf{B}^0\times\{(1+d_e^2)\nabla\times\mathbf{b} - \mathbf{b} + d_e^2\nabla^2\mathbf{b}\}] + \nu\nabla^2\mathbf{b}. \quad (36)$$

We assume that the magnetic Reynolds number Re_m is large (i.e., ν is a small parameter) and adopt the parameter ordering such that $(|\partial/\partial y|, |\partial/\partial z|) \simeq \nu^2$ and $|\partial/\partial t| \simeq \nu^5$. We introduce slow variables similar to variables (11) and (30),

$$Y = \nu^2 y, \quad Z = \nu^2 z, \quad T = \nu^5 t, \quad (37)$$

and seek a solution to Eq. (36) in the form of an asymptotic expansion that is analogous to expansion (24) and in which the role of the small parameter is played by ν (i.e., $\epsilon = \nu$). The perturbations of interest are assumed to be periodic in the variable x and to satisfy condition (12).

Under these assumptions, the components of Eq. (36) in Cartesian coordinates have the form

$$\nu^5\frac{\partial}{\partial T}(\hat{M}b_x - \nu^4 d_e^2\nabla_s^2 b_x) = \nu\left(\frac{\partial^2 b_x}{\partial x^2} + \nu^4\nabla_s^2 b_x\right) + \nu^2\hat{L}\left\{\hat{M}b_x - \nu^4 d_e^2\nabla_s^2 b_x - \nu^2(1+d_e^2)\left(\frac{\partial b_z}{\partial Y} - \frac{\partial b_y}{\partial Z}\right)\right\}, \quad (38)$$

$$\nu^5\frac{\partial}{\partial T}(\hat{M}b_y - \nu^4 d_e^2\nabla_s^2 b_y) = \nu\left(\frac{\partial^2 b_y}{\partial x^2} + \nu^4\nabla_s^2 b_y\right) + \nu^2\hat{L}\left\{\hat{M}b_y - \nu^4 d_e^2\nabla_s^2 b_y + (1+d_e^2)\left(\frac{\partial b_z}{\partial x} - \nu^2\frac{\partial b_x}{\partial Z}\right)\right\} - \cos x\left\{\hat{M}b_x - \nu^4 d_e^2\nabla_s^2 b_x - \nu^2(1+d_e^2)\left(\frac{\partial b_z}{\partial Y} - \frac{\partial b_y}{\partial Z}\right)\right\}, \quad (39)$$

$$\nu^5\frac{\partial}{\partial T}(\hat{M}b_z - \nu^4 d_e^2\nabla_s^2 b_z) = \nu\left(\frac{\partial^2 b_z}{\partial x^2} + \nu^4\nabla_s^2 b_z\right) + \nu^2\hat{L}\left\{\hat{M}b_z - \nu^4 d_e^2\nabla_s^2 b_z + (1+d_e^2)\left(\nu^2\frac{\partial b_x}{\partial Y} - \frac{\partial b_y}{\partial x}\right)\right\} + \sin x\left\{\hat{M}b_x - \nu^4 d_e^2\nabla_s^2 b_x - \nu^2(1+d_e^2)\left(\frac{\partial b_z}{\partial Y} - \frac{\partial b_y}{\partial Z}\right)\right\}, \quad (40)$$

where the operators $\hat{M}$ and $\hat{L}$ are defined as

$$\hat{M} = 1 - d_e^2\frac{\partial^2}{\partial x^2}, \quad \hat{L} = \sin x\frac{\partial}{\partial Y} + \cos x\frac{\partial}{\partial Z}. \quad (41)$$

The only modification to be made in Eqs. (20), (21), and (23) is the replacement $\epsilon \longrightarrow \nu^2$. In further calculations, instead of Eq. (38), it is convenient to use the incompressibility condition for the magnetic field, $\nabla\cdot\mathbf{b} = 0$, which can be rewritten as

$$\frac{\partial b_x}{\partial x} + \nu^2\frac{\partial b_y}{\partial Y} + \nu^2\frac{\partial b_z}{\partial Z} = 0. \quad (42)$$

We average Eqs. (38)–(40) over the period of the fast variable x to obtain the following equations, which will serve as the basis to investigate the stability of the long-wavelength perturbations of a helical flow:

$$\begin{aligned}
&\nu^5\frac{\partial}{\partial T}(\langle b_x\rangle - \nu^4 d_e^2\nabla_s^2\langle b_x\rangle) = \nu^5\nabla_s^2\langle b_x\rangle + \nu^4(1+d_e^2)\\
&\times\left\{\left(\frac{\partial^2}{\partial Z^2}-\frac{\partial^2}{\partial Y^2}\right)(\langle b_y\cos x\rangle + \langle b_z\sin x\rangle)\right.\\
&\left.+\,2\frac{\partial^2}{\partial Y\partial Z}(\langle b_y\sin x\rangle - \langle b_z\cos x\rangle)\right\}\\
&+\nu^8 d_e^2\nabla_s^2\left\{\frac{\partial^2}{\partial Y^2}\langle b_y\cos x\rangle - \frac{\partial^2}{\partial Z^2}\langle b_z\sin x\rangle\right.\\
&\left.+\,\frac{\partial^2}{\partial Y\partial Z}(\langle b_z\cos x\rangle - \langle b_y\sin x\rangle)\right\},
\end{aligned} \tag{43}$$

$$\begin{aligned}
&\nu^5\frac{\partial}{\partial T}(\langle b_y\rangle - \nu^4 d_e^2\nabla_s^2\langle b_y\rangle) = \nu^5\nabla_s^2\langle b_y\rangle\\
&+\nu^6(1+d_e^2)\frac{\partial}{\partial Z}\left\{\frac{\partial^2}{\partial Y^2}\langle b_y\cos x\rangle - \frac{\partial^2}{\partial Z^2}\langle b_z\sin x\rangle\right.\\
&\left.+\,\frac{\partial^2}{\partial Y\partial Z}(\langle b_z\cos x\rangle - \langle b_y\sin x\rangle)\right\}\\
&+\nu^6 d_e^2\frac{\partial}{\partial Z}\nabla_s^2\{\langle b_z\sin x\rangle - \langle b_y\cos x\rangle\},
\end{aligned} \tag{44}$$

$$\begin{aligned}
&\nu^5\frac{\partial}{\partial T}(\langle b_z\rangle - \nu^4 d_e^2\nabla_s^2\langle b_z\rangle) = \nu^5\nabla_s^2\langle b_z\rangle\\
&-\nu^6(1+d_e^2)\frac{\partial}{\partial Z}\left\{\frac{\partial^2}{\partial Y^2}\langle b_y\cos x\rangle - \frac{\partial^2}{\partial Z^2}\langle b_z\sin x\rangle\right.\\
&\left.+\,\frac{\partial^2}{\partial Y\partial Z}(\langle b_z\cos x\rangle - \langle b_y\sin x\rangle)\right\}\\
&-\nu^6 d_e^2\frac{\partial}{\partial Y}\nabla_s^2\{\langle b_z\sin x\rangle - \langle b_y\cos x\rangle\}.
\end{aligned} \tag{45}$$

To zeroth order in the parameter ν, Eqs. (39), (40), and (42) yield

$$\hat{M}b_x^{(0)} \equiv \left(1 - d_e^2\frac{\partial^2}{\partial x^2}\right)b_x^{(0)} = 0, \quad \frac{\partial b_x^{(0)}}{\partial x} = 0. \tag{46}$$

As a result, we get $b_x^{(0)} = 0$. To first order in ν, we find

$$\begin{aligned}
&-\hat{M}b_x^{(1)}\cos x + \frac{\partial^2 b_y^{(0)}}{\partial x^2} = 0, \quad \frac{\partial b_x^{(1)}}{\partial x} = 0,\\
&\hat{M}b_x^{(1)}\sin x + \frac{\partial^2 b_z^{(0)}}{\partial x^2} = 0.
\end{aligned} \tag{47}$$

The solution to Eqs. (47) has the form

$$\begin{aligned}
&b_x^{(1)} = b_{sx}^{(1)}(Y, Z, T),\\
&b_y^{(0)} = -b_{sx}^{(1)}\cos x, \quad b_z^{(0)} = b_{sx}^{(1)}\sin x.
\end{aligned} \tag{48}$$

In solution (48), the functions $b_y^{(0)}$ and $b_z^{(0)}$ should be supplemented with arbitrary x-independent functions. However, we choose the arbitrary functions to be zero, because additional analysis shows that, for the ordering assumed in this section, the long-wavelength fields in question are damped on a time scale of $1/\nu^3$ by the plasma resistivity ν.

In Eqs. (39), (40), and (42), the terms on the order of ν^2 satisfy the set of equations

$$\begin{aligned}
&\frac{\partial^2 b_y^{(1)}}{\partial x^2} - \cos x\left\{\hat{M}b_x^{(2)} - (1+d_e^2)\left(\frac{\partial b_z^{(0)}}{\partial Y} - \frac{\partial b_y^{(0)}}{\partial Z}\right)\right\}\\
&+\hat{L}\left\{\hat{M}b_y^{(0)} + (1+d_e^2)\frac{\partial b_z^{(0)}}{\partial x}\right\} = 0,\\
&\frac{\partial^2 b_z^{(1)}}{\partial x^2} + \sin x\left\{\hat{M}b_x^{(2)} - (1+d_e^2)\left(\frac{\partial b_z^{(0)}}{\partial Y} - \frac{\partial b_y^{(0)}}{\partial Z}\right)\right\}\\
&+\hat{L}\left\{\hat{M}b_z^{(0)} - (1+d_e^2)\frac{\partial b_y^{(0)}}{\partial x}\right\} = 0,\\
&\frac{\partial b_x^{(2)}}{\partial x} + \frac{\partial b_y^{(0)}}{\partial Y} + \frac{\partial b_z^{(0)}}{\partial Z} = 0.
\end{aligned} \tag{49}$$

Substituting first-order solution (48) into these equations, we derive their second-order solution in the form

$$\begin{aligned}
&b_x^{(2)} = b_{sx}^{(2)}(Y, Z, T) + \sin x\frac{\partial b_{sx}^{(1)}}{\partial Y} + \cos x\frac{\partial b_{sx}^{(1)}}{\partial Z},\\
&b_y^{(1)} = b_{sy}^{(1)}(Y, Z, T) - b_{sx}^{(2)}\cos x,\\
&b_z^{(1)} = b_{sz}^{(1)}(Y, Z, T) + b_{sx}^{(2)}\sin x.
\end{aligned} \tag{50}$$

To third order in ν, Eqs. (39), (40), and (42) become

$$\frac{\partial^2 b_y^{(2)}}{\partial x^2} - \cos x\left\{\hat{M}b_x^{(3)} - (1+d_e^2)\left(\frac{\partial b_z^{(1)}}{\partial Y} - \frac{\partial b_y^{(1)}}{\partial Z}\right)\right\}$$

$$+\hat{L}\left\{\hat{M}b_y^{(1)} + (1+d_e^2)\frac{\partial b_z^{(1)}}{\partial x}\right\} = 0,$$

$$\frac{\partial^2 b_z^{(2)}}{\partial x^2} + \sin x\left\{\hat{M}b_x^{(3)} - (1+d_e^2)\left(\frac{\partial b_z^{(1)}}{\partial Y} - \frac{\partial b_y^{(1)}}{\partial Z}\right)\right\} \quad (51)$$

$$+\hat{L}\left\{\hat{M}b_z^{(1)} - (1+d_e^2)\frac{\partial b_y^{(1)}}{\partial x}\right\} = 0,$$

$$\frac{\partial b_x^{(3)}}{\partial x} + \frac{\partial b_y^{(1)}}{\partial Y} + \frac{\partial b_z^{(1)}}{\partial Z} = 0.$$

The solution to Eqs. (51) can be found by using solution (50):

$$b_x^{(3)} = b_{sx}^{(3)}(Y, Z, T) + \sin x\frac{\partial b_{sx}^{(2)}}{\partial Y} + \cos x\frac{\partial b_{sx}^{(2)}}{\partial Z},$$

$$b_y^{(2)} = b_{sy}^{(2)}(Y, Z, T) + \sin x\frac{\partial b_{sy}^{(1)}}{\partial Y}$$

$$+\cos x\left\{(1+d_e^2)\frac{\partial b_{sz}^{(1)}}{\partial Y} - d_e^2\frac{\partial b_{sy}^{(1)}}{\partial Z} - b_{sx}^{(3)}\right\}, \quad (52)$$

$$b_z^{(2)} = b_{sz}^{(2)}(Y, Z, T) + \cos x\frac{\partial b_{sz}^{(1)}}{\partial Z}$$

$$+\sin x\left\{(1+d_e^2)\frac{\partial b_{sy}^{(1)}}{\partial Z} - d_e^2\frac{\partial b_{sz}^{(1)}}{\partial Y} + b_{sx}^{(3)}\right\}.$$

In addition, to third order in ν, Eq. (23) with the replacement of ϵ by ν^2 gives

$$\frac{\partial b_{sy}^{(1)}}{\partial Y} + \frac{\partial b_{sz}^{(1)}}{\partial Z} = 0. \quad (53)$$

Substituting solution (48), (50), and (52) into Eqs. (43)–(45) averaged over the period of the fast variable x, in the sixth order in ν we obtain the equations

$$\frac{\partial b_{sx}^{(1)}}{\partial T} = \frac{1}{2}(1+d_e^2)\nabla_s^2\left(\frac{\partial b_{sy}^{(1)}}{\partial Z} - \frac{\partial b_{sz}^{(1)}}{\partial Y}\right) + \nabla_s^2 b_{sx}^{(1)},$$

$$\frac{\partial b_{sy}^{(1)}}{\partial T} = -\frac{1}{2}(1-d_e^2)\nabla_s^2\frac{\partial b_{sx}^{(1)}}{\partial Z} + \nabla_s^2 b_{sy}^{(1)}, \quad (54)$$

$$\frac{\partial b_{sz}^{(1)}}{\partial T} = \frac{1}{2}(1-d_e^2)\nabla_s^2\frac{\partial b_{sx}^{(1)}}{\partial Y} + \nabla_s^2 b_{sz}^{(1)}.$$

First, we should note that the effects produced by the interaction of a long-wavelength perturbation with the primary flow are proportional to the microhelicity of the flow, $\mathbf{B}^0 \cdot (\nabla \times \mathbf{B}^0)$, a fact that is not obvious from Eqs. (54) because, under the above normalization conditions, the microhelicity is equal to unity. The results obtained in the next section provide clear evidence in support of this conclusion. In the limit $d_e \longrightarrow 0$, which corresponds to the wavelengths of a helical flow for which the effects of electron inertia are negligible, the effect of a helical flow on the long-wavelength perturbation is proportional to $\nabla_s^2(\nabla \times \mathbf{b}_s^{(1)})$ (we assume here that the long-wavelength perturbation is independent of x). In this case, averaged equations (54) are similar in form to the equations for the averaged magnetic field that were derived in [17] in studying the effect of small-scale helical EMHD turbulence on long-wavelength perturbations. This effect may be called an α-like effect, in analogy to the effect of a random velocity field with a nonzero average helicity—one that is well known in turbulent MHD dynamo theory [18]. From Eqs. (54), we can see that, in the case of a smaller-scale flow, the effects of electron inertia modify the final results in such a way that the primary flow has different effects on the component $b_{sx}^{(1)}$, which is parallel to the wave vector of the flow, and on the components perpendicular to the wave vector. Hence, in the case at hand, we may speak of an anisotropic α-like effect. In investigating the influence of collisionless EMHD turbulence on long-wavelength perturbations in a recent paper [19], it was found that, when the effects of electron inertia are taken into account, the results obtained in [17] are modified in an analogous way.

Using Eq. (53) and introducing the flux function ϕ_s through the relationships

$$b_{sy}^{(1)} = \frac{\partial \phi_s}{\partial Z}, \quad b_{sz}^{(1)} = -\frac{\partial \phi_s}{\partial Y}, \quad (55)$$

allow us to reduce the set of three equations (54) to the following two equations:

$$\frac{\partial b_{sx}^{(1)}}{\partial T} = \frac{1}{2}(1+d_e^2)\nabla_s^4\phi + \nabla_s^2 b_{sx}^{(1)},$$
$$\frac{\partial \phi_s}{\partial T} = -\frac{1}{2}(1-d_e^2)\nabla_s^2 b_{sx}^{(1)} + \nabla_s^2\phi_s. \quad (56)$$

Looking for a solution to Eqs. (56) in the form $(b_{sx}^{(1)}, \phi_s) \sim \exp(\gamma T + i(q_y Y + q_z Z))$, we arrive at the asymptotic dispersion relation

$$(\gamma + q^2)^2 = \frac{1}{4}(1-d_e^4)q^6, \quad q^2 \equiv q_y^2 + q_z^2. \quad (57)$$

Recalling definitions (37) of the slow variables Y, Z, and T, we see that, in order to go back to the initial variables and perturbations, which are proportional to $\exp(\gamma t + i(q_y y + q_z z))$, it is necessary to make the replacements $\gamma \longrightarrow \gamma/\nu^5$ and $\mathbf{q} \longrightarrow \mathbf{q}/\nu^2$. As a result, we obtain

$$(\gamma + \nu q^2)^2 = \frac{1}{4\nu^2}(1 - d_e^4)q^6. \quad (58)$$

For $d_e < 1$, the roots of Eq. (58) are real,

$$\gamma = -\nu q^2 \pm \frac{1}{2\nu} q^3 \sqrt{1 - d_e^4}, \quad (59)$$

and perturbations with $q > 2\nu^2/\sqrt{1 - d_e^4}$ are aperiodically unstable. On the other hand, for $d_e > 1$, the right-hand side of Eq. (58) is negative; hence, because of the interaction with the flow, the frequency of a long-wavelength perturbation acquires a nonzero real part, $\mathrm{Im}\gamma \neq 0$ (i.e., $\mathrm{Re}\,\omega \neq 0$). However, such a perturbation is damped by the plasma resistivity. Hence, we can conclude that a helical flow occurring on a spatial scale smaller than the electron collisionless skin depth, $l < c/\omega_{pe}$, is stable against long-wavelength perturbations.

Numerical results on the stability of a Beltrami-type helical flow are illustrated in Figs. 5–7.

3.3. Anisotropic Helical Flow

In addition to the solution describing a helical flow, which was considered in the previous section, Eq. (4) has the solution that describes a so-called anisotropic helical flow:

$$\mathbf{B}^0 = \mathbf{e}_y \sin x \cos\alpha + \mathbf{e}_z \cos x \sin\alpha,$$
$$\mathbf{v} \propto \mathbf{e}_y \sin x \sin\alpha + \mathbf{e}_z \cos x \cos\alpha. \quad (60)$$

Here, the magnetic field is normalized to $B_0 = \sqrt{(B_y^0)^2 + (B_z^0)^2}$, where B_y^0 and B_z^0 are the magnetic field amplitudes along the y- and z-axes; i.e., $\sin\alpha = B_y^0/B_0$ and $\cos\alpha = B_z^0/B_0$. Solution (60) is a stationary solution to Eq. (4) if the external source term has the form

$$\mathbf{f} = \nu\mathbf{B}^0 = \nu(\mathbf{e}_y \sin x \cos\alpha + \mathbf{e}_z \cos x \sin\alpha). \quad (61)$$

On the one hand, the flow in question has a nonzero microhelicity, $\mathbf{B}^0 \cdot (\nabla \times \mathbf{B}^0) = (1/2)\sin 2\alpha$. On the other hand, it is anisotropic in the yz plane in the sense that $(B_y^0)^2 - (B_z^0)^2 \propto \cos 2\alpha \neq 0$. That is why we call this flow an anisotropic helical flow. In contrast to the helical flow analyzed in the previous section, solution (60) does not belong to a class of solutions corresponding to force-free equilibrium flows and satisfies the equation

$$[(\mathbf{B}^0 - d_e^2 \nabla^2 \mathbf{B}^0) \times (\nabla \times \mathbf{B}^0)] = (1 + d_e^2)\nabla \frac{(\mathbf{B}^0)^2}{2}. \quad (62)$$

We consider the stability of an anisotropic helical flow against small long-wavelength perturbations in two cases: $|\cos 2\alpha| \simeq \nu^2 \ll 1$ (small anisotropy) and $|\cos 2\alpha| \simeq 1$ (large anisotropy).

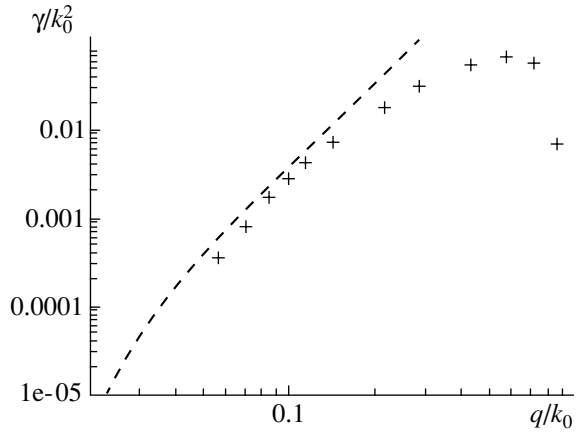

Fig. 5. Growth rate vs. the absolute value of the wave vector q for $d_e = 0.1$ and $\nu = 0.1$ in the case of a Beltrami flow. In this figure and the next two figures, the crosses present numerical results and the dashed line refer to asymptotic formula (59). The flow is seen to become stable both at small ($q/k_0 < 0.01$) and large ($q/k_0 > 0.8$) absolute values of the wave vector.

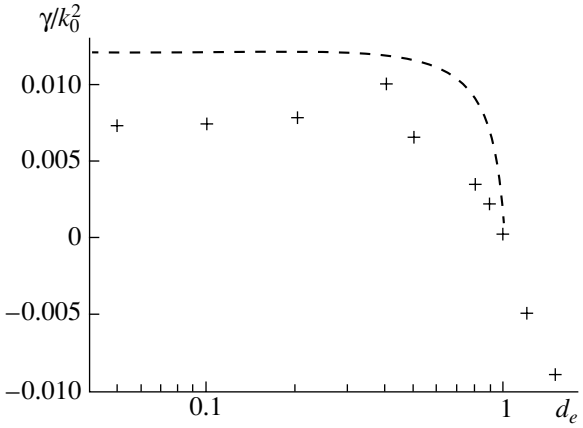

Fig. 6. Growth rate vs. d_e for $\nu = 0.1$ and $q/k_0 = 0.1\sqrt{2}$. In accordance with formula (59), referring to the dashed curve, the stability boundary is seen to be at $d_e \approx 1$.

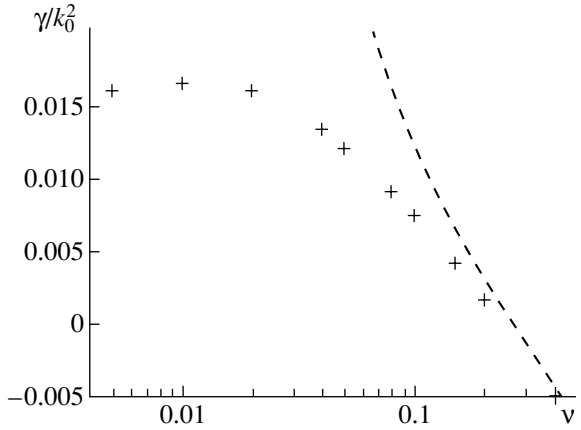

Fig. 7. Growth rate vs. ν for $d_e = 0.1$ and $q/k_0 = 0.1\sqrt{2}$ in the case of a Beltrami flow.

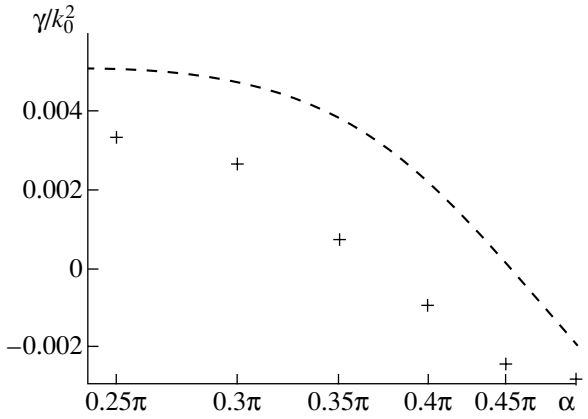

Fig. 8. Growth rate vs. the degree of anisotropy α of an anisotropic helical flow for ν = 0.1, d_e = 0.1, and q_y/k_0 = q_z/k_0 = 0.1. The crosses present numerical results, and the dashed curve refers to asymptotic formula (65). In the limit of small anisotropy (α ⟶ π/4), the flow becomes a Beltrami-type flow.

3.3.1. The case of a small anisotropy. Here, we adopt the same parameter ordering as in the previous section, namely, ordering (37). Applying the above asymptotic procedure, we take into account the anisotropy effect to obtain the following modification of Eqs. (54) in sixth order in the parameter ν:

$$\frac{\partial b_{sx}^{(1)}}{\partial T} = \nabla_s^2 b_{sx}^{(1)} + \frac{\cos 2\alpha}{2\nu^2}(1+d_e^2)\left(\frac{\partial^2}{\partial Y^2} - \frac{\partial^2}{\partial Z^2}\right) b_{sx}^{(1)} + \frac{\sin 2\alpha}{4}(1+d_e^2)\nabla_s^2\left(\frac{\partial b_{sy}^{(1)}}{\partial Z} - \frac{\partial b_{sz}^{(1)}}{\partial Y}\right),$$
$$\frac{\partial b_{sy}^{(1)}}{\partial T} = \nabla_s^2 b_{sy}^{(1)} - \frac{\sin 2\alpha}{4}(1-d_e^2)\nabla_s^2 \frac{\partial b_{sx}^{(1)}}{\partial Z}, \qquad (63)$$
$$\frac{\partial b_{sz}^{(1)}}{\partial T} = \nabla_s^2 b_{sz}^{(1)} + \frac{\sin 2\alpha}{4}(1-d_e^2)\nabla_s^2 \frac{\partial b_{sx}^{(1)}}{\partial Y},$$

where the components $b_{sy}^{(1)}$ and $b_{sz}^{(1)}$ satisfy Eq. (53). Hence, the primary anisotropic helical flow results in two effects in the equations for long-wavelength perturbations. On the one hand, the flow produces an α-like effect, which is proportional to the flow microhelicity (1/2)sin2α (cf. the result obtained in the previous section), as is the case with a Beltrami isotropic helical flow, and, on the other, it contributes a resistive term to the evolutionary equation for the field component $b_{sx}^{(1)}$. By analogy with the previous section, we introduce the flux function ϕ_s to reduce the set of equations (63) to two equations:

$$\frac{\partial b_{sx}^{(1)}}{\partial T} = \nabla_s^2 b_{sx}^{(1)} + \frac{\cos 2\alpha}{2\nu^2}(1+d_e^2)\left(\frac{\partial^2}{\partial Y^2} - \frac{\partial^2}{\partial Z^2}\right) b_{sx}^{(1)} + \frac{\sin 2\alpha}{4}(1+d_e^2)\nabla_s^4\phi, \qquad (64)$$
$$\frac{\partial \phi_s}{\partial T} = \nabla_s^2\phi_s - \frac{\sin 2\alpha}{4}(1-d_e^2)\nabla_s^2 b_{sx}^{(1)}.$$

Equations (64) yield the asymptotic dispersion relation

$$\gamma = -q^2 + \frac{\cos 2\alpha}{4\nu^2}(1+d_e^2)(q_y^2 - q_z^2) \pm \frac{1}{4}\sqrt{\frac{\cos^2 2\alpha}{\nu^4}(1+d_e^2)^2(q_y^2-q_z^2)^2 + \sin^2 2\alpha(1-d_e^4)q^6}. \qquad (65)$$

For cos2α > 0 (i.e., when the field amplitude in the *y* direction is larger than that in the *z* direction), the perturbation with $q_z = 0$ and $q_y = q$ is most unstable. For cos2α < 0, the most unstable perturbation is that with $q_y = 0$ and $q_z = q$. In both cases, the frequency of the perturbation acquires a nonzero real part (i.e., Imγ ≠ 0) due to the microhelical nature of the flow, provided that the inequalities $d_e > 1$ and

$$q > \frac{|\cot 2\alpha|(1+d_e^2)}{\nu^2\sqrt{d_e^4 - 1}} \qquad (66)$$

are satisfied. The instability criterion derived from dispersion relation (65) can be written as

$$\frac{|\cos 2\alpha|(1+d_e^2)}{2\nu^2} + \frac{\sin^2 2\alpha}{16}(1-d_e^4)q^2 > 1. \qquad (67)$$

Numerical results reflecting the dependence of the growth rate of the perturbation of a weakly anisotropic helical flow on the degree to which it is anisotropic are presented in Fig. 8.

3.3.2. The case of a large anisotropy. In the case of a strongly anisotropic flow, |cos2α| ≃ 1, the most destabilizing factor is anisotropy, while the effect of the microhelicity of the flow is negligible; in this case, the stability analysis is analogous to that carried out in Section 3.1.

For ν ≃ 1 (the case of small values of the magnetic Reynolds number), we use ordering (11). Applying the above method of two-scale expansions, we obtain the following evolutionary equation for the *x* component of the magnetic field of long-wavelength perturbations:

$$\frac{\partial b_{sx}^{(0)}}{\partial T} = \nu\nabla_s^2 b_{sx}^{(0)} + \frac{\cos 2\alpha}{2\nu}(1+d_e^2)\left(\frac{\partial^2}{\partial Y^2} - \frac{\partial^2}{\partial Z^2}\right) b_{sx}^{(0)}. \qquad (68)$$

According to Eqs. (27), the *y* and *z* components of the magnetic field of the perturbations are damped by the plasma resistivity. The *x* component of the magnetic

field of long-wavelength perturbations is unstable under the condition

$$\frac{\cos 2\alpha}{2\nu^2}(1 + d_e^2)\frac{q_z^2 - q_y^2}{q^2} > 1. \quad (69)$$

In the case $\cos 2\alpha > 0$, the most unstable perturbations are those with $q_y = 0$ and $q_z = q$; in the opposite case, these are the perturbations with $q_z = 0$ and $q_y = q$. Consequently, we can say that the wave vector of the most unstable perturbation is directed along the axis along which the amplitude of the magnetic field of the primary flow is the largest. In both cases, the growth rate of the most unstable perturbation is

$$\gamma = \left[\frac{|\cos 2\alpha|}{2\nu}(1 + d_e^2) - \nu\right]q^2. \quad (70)$$

For $\nu \ll 1$, we adopt ordering (30). Accordingly, we arrive at the same results as that obtained in Section 3.1, namely, that the x component of the long-wavelength magnetic field enters only at the first order in ν and its evolution is described by the equation

$$\frac{\partial b_{sx}^{(1)}}{\partial T} = \frac{\cos 2\alpha}{2}(1 + d_e^2)\left(\frac{\partial^2}{\partial Y^2} - \frac{\partial^2}{\partial Z^2}\right)b_{sx}^{(1)}. \quad (71)$$

Consequently, the above stability analysis remains valid and we again see that the instability growth rate is proportional to the magnetic Reynolds number $Re_m = 1/\nu$. As in the previous case, the x and y components of the long-wavelength magnetic field are damped by the plasma resistivity.

Hence, the stability of a strongly anisotropic flow is determined by the anisotropy of the flow. In this case, one can use the stability criteria obtained in Section 3.1 for a Kolmogorov-type flow, with the corresponding replacements $1 \longrightarrow \cos 2\alpha$.

Numerical results on a strongly anisotropic helical flow are shown in Fig. 9.

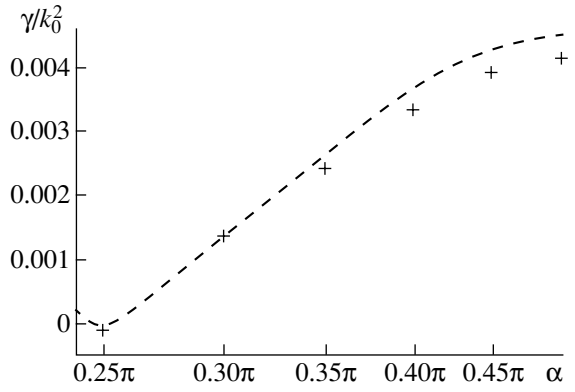

Fig. 9. Growth rate vs. α for $\nu = 0.1$, $d_e = 0.1$, $q_y = 0.01q_z$, and $q_z/k_0 = 0.3$. The crosses present numerical results and the dashed curve refers to asymptotic formula (70). In the limit of large anisotropy ($\alpha \longrightarrow \pi/2$), the flow becomes a Kolmogorov-type flow.

4. STABILITY OF A HELICON

As was noted in Section 2, the EMHD equations for a plasma in an external magnetic field have solutions describing linear waves with a nonzero frequency, which are called helicons. We assume that the external magnetic field B_0 is constant and uniform and is directed along the z-axis. We also normalize the magnetic field and the spatial variables to B_0 and $l = 1/k$ (where k is wavenumber of a helicon). In this case, EMHD equations (4) have the solution

$$\hat{\mathbf{B}}^0 = \mathbf{e}_z + \mathbf{B}^0,$$
$$\mathbf{B}^0 = C_0(-k_z\mathbf{e}_x\cos\psi + \mathbf{e}_y\sin\psi + k_x\mathbf{e}_z\cos\psi), \quad (72)$$

where

$$\psi = k_x x + k_z z - \omega(\mathbf{k})t,$$
$$k = \sqrt{k_x^2 + k_z^2} \equiv 1, \quad \omega(\mathbf{k}) = \frac{k_z}{1 + d_e^2}. \quad (73)$$

The first term in the expression for $\hat{\mathbf{B}}^0$ accounts for the external magnetic field, and the second term describes the magnetic field of a helicon. The solution described by formulas (72) and (73) is a stationary one (i.e., the wave amplitude C_0 is time independent) provided that the source term on the right-hand side of Eq. (4) has the form $\mathbf{f} = \nu\mathbf{B}^0$, in which case the source exactly counterbalances the resistive dissipation of a helicon. The solution corresponds to a helicon whose frequency is described by dispersion relation (5) with the plus sign. Since the helicon described by solution (72) satisfies the relationship $\nabla \times \mathbf{B}^0 = \mathbf{B}^0$, it belongs to the class of force-free equilibrium solutions and, consequently, being a solution to the linearized EMHD equations, it also satisfies nonlinear equation (4)—a fact that is well known in the theory (see, e.g., [15]). As has been mentioned in Section 3, the helicon frequency in the limit $k_z = 0$ is equal to zero; as a result, the helicon converts into the steady-state helical flow described by solution (34). The helicons have a nonzero microhelicity, $\mathbf{B}^0 \cdot (\nabla \times \mathbf{B}^0) = (\mathbf{B}^0)^2 = C_0^2$, as is the case with a helical flow.

Let us consider the stability of a helicon described by solution (72) against long-wavelength perturbations. The corresponding linearized equation for the perturbations of the helicon is a slight modification of Eq. (36):

$$\frac{\partial}{\partial t}(\mathbf{b} - d_e^2\nabla^2\mathbf{b}) + \frac{\partial}{\partial z}\nabla \times \mathbf{b}$$
$$= \nabla \times [\mathbf{B}^0 \times \{(1 + d_e^2)\nabla \times \mathbf{b} - \mathbf{b} + d_e^2\nabla^2\mathbf{b}\}] + \nu\nabla^2\mathbf{b}. \quad (74)$$

To simplify further calculations, it is convenient to introduce the new variables $\mathbf{h}$ and $\bar{\mathbf{r}}$:

$$h_x = k_x b_x + k_z b_z, \quad h_y = b_y, \quad h_z = k_x b_z - k_z b_x,$$
$$\bar{x} = k_x x + k_z z, \quad \bar{y} = y, \quad \bar{z} = k_x z - k_z x. \tag{75}$$

We assume that the magnetic Reynolds number is large (i.e., ν is a small parameter) and adopt a parameter ordering such that $|\partial/\partial\bar{x}| \simeq 1$ and $(|\partial/\partial\bar{y}|, |\partial/\partial\bar{z}|) \simeq \nu^2$. We also set $k_x \simeq k_z \simeq 1$ and $d_e \simeq 1$. The problem at hand has three time scales: (i) the time that is inversely proportional to the frequency of the primary helicon, $\omega(\mathbf{k})^{-1} \simeq 1$; (ii) the time scale of the secondary long-wavelength helicon, T; and (iii) the dissipative time of the secondary helicon, τ, which is determined by the effect of the plasma resistivity ν and that of the primary helicon on the secondary helicon. This is confirmed by the results that will be discussed below. By analogy with variables (11), we introduce the slow variables

$$Y = \nu^2\bar{y}, \quad Z = \nu^2\bar{z}, \quad T = \nu^4 t, \quad \tau = \nu^5 t. \tag{76}$$

We look for a solution to Eq. (36) in the form of an asymptotic expansion in powers of the small parameter ν:

$$\mathbf{h} = \mathbf{h}^{(0)} + \nu\mathbf{h}^{(1)} + \nu^2\mathbf{h}^{(2)} + \ldots. \tag{77}$$

We assume that the perturbations depend on $\psi = \bar{x} - \omega(\mathbf{k})t$, Y, Z, T, and τ and are periodic in ψ; i.e., $\mathbf{h}(\psi + 2\pi) = \mathbf{h}(\psi)$. In the new variables, the components of Eq. (74) in Cartesian coordinates are similar in form to Eqs. (38)–(40):

$$\left(-\frac{k_z}{1+d_e^2}\frac{\partial}{\partial\psi} + \nu^4\frac{\partial}{\partial T} + \nu^5\frac{\partial}{\partial\tau}\right)(\hat{M}h_x - \nu^4 d_e^2\nabla_s^2 h_x)$$
$$+ \nu^2\left(k_z\frac{\partial}{\partial\psi} + \nu^2 k_x\frac{\partial}{\partial Z}\right)\left(\frac{\partial h_z}{\partial Y} - \frac{\partial h_y}{\partial Z}\right)$$
$$= \nu\left(\frac{\partial^2 h_x}{\partial\psi^2} + \nu^4\nabla_s^2 h_x\right) + \nu^2 C_0\hat{L}\left\{\hat{M}h_x\right.$$
$$\left. - \nu^4 d_e^2\nabla_s^2 h_x + \nu^2(1+d_e^2)\left(\frac{\partial h_y}{\partial Z} - \frac{\partial h_z}{\partial Y}\right)\right\}, \tag{78}$$

$$\left(-\frac{k_z}{1+d_e^2}\frac{\partial}{\partial\psi} + \nu^4\frac{\partial}{\partial T} + \nu^5\frac{\partial}{\partial\tau}\right)(\hat{M}h_y - \nu^4 d_e^2\nabla_s^2 h_y)$$
$$+ \left(k_z\frac{\partial}{\partial\psi} + \nu^2 k_x\frac{\partial}{\partial Z}\right)\left(\nu^2\frac{\partial h_x}{\partial Z} - \frac{\partial h_z}{\partial\psi}\right)$$
$$= \nu\left(\frac{\partial^2 h_y}{\partial\psi^2} + \nu^4\nabla_s^2 h_y\right) + \nu^2 C_0\hat{L}\left\{\hat{M}h_y\right.$$
$$\left. - \nu^4 d_e^2\nabla_s^2 h_y + (1+d_e^2)\left(\frac{\partial h_z}{\partial\psi} - \nu^2\frac{\partial h_x}{\partial Z}\right)\right\}$$
$$- C_0\cos\psi\left\{\hat{M}h_x - \nu^4 d_e^2\nabla_s^2 h_x - \nu^2(1+d_e^2)\left(\frac{\partial h_z}{\partial Y} - \frac{\partial h_y}{\partial Z}\right)\right\}, \tag{79}$$

$$\left(-\frac{k_z}{1+d_e^2}\frac{\partial}{\partial\psi} + \nu^4\frac{\partial}{\partial T} + \nu^5\frac{\partial}{\partial\tau}\right)(\hat{M}h_z - \nu^4 d_e^2\nabla_s^2 h_z)$$
$$+ \left(k_z\frac{\partial}{\partial\psi} + \nu^2 k_x\frac{\partial}{\partial Z}\right)\left(\frac{\partial h_y}{\partial\psi} - \nu^2\frac{\partial h_x}{\partial Y}\right)$$
$$= \nu\left(\frac{\partial^2 h_z}{\partial\psi^2} + \nu^4\nabla_s^2 h_z\right) + \nu^2 C_0\hat{L}\left\{\hat{M}h_z\right. \tag{80}$$
$$\left. - \nu^4 d_e^2\nabla_s^2 h_z + (1+d_e^2)\left(\nu^2\frac{\partial h_x}{\partial Y} - \frac{\partial h_y}{\partial\psi}\right)\right\}$$
$$+ C_0\sin\psi\left\{\hat{M}h_x - \nu^4 d_e^2\nabla_s^2 h_x - \nu^2(1+d_e^2)\left(\frac{\partial h_z}{\partial Y} - \frac{\partial h_y}{\partial Z}\right)\right\},$$

where the operators $\hat{M}$ and $\hat{L}$ are given by formulas (41) with the replacement of x by ψ. In the new variables, the equation $\nabla\cdot\mathbf{b} = 0$ becomes

$$\frac{\partial h_x}{\partial\psi} + \nu^2\frac{\partial h_y}{\partial Y} + \nu^2\frac{\partial h_z}{\partial Z} = 0. \tag{81}$$

Averaging Eqs. (78)–(80) over the period of ψ, we obtain the following equations for the components of the magnetic field of long-wavelength perturbations:

$$\left(\nu^4\frac{\partial}{\partial T} + \nu^5\frac{\partial}{\partial\tau}\right)(\langle h_x\rangle - \nu^4 d_e^2\nabla_s^2\langle h_x\rangle)$$
$$+ \nu^4 k_x\frac{\partial}{\partial Z}\left(\frac{\partial h_z}{\partial Y} - \frac{\partial h_y}{\partial Z}\right) = \nu^5\nabla_s^2\langle h_x\rangle$$
$$+ \nu^4 C_0(1+d_e^2)\left\{\left(\frac{\partial^2}{\partial Z^2} - \frac{\partial^2}{\partial Y^2}\right)(\langle h_y\cos\psi\rangle + \langle h_z\sin\psi\rangle)\right.$$
$$\left. + 2\frac{\partial^2}{\partial Y\partial Z}(\langle h_y\sin\psi\rangle - \langle h_z\cos\psi\rangle)\right\} \tag{82}$$
$$+ \nu^8 d_e^2 C_0\nabla_s^2\left\{\frac{\partial^2}{\partial Y^2}\langle h_y\cos\psi\rangle - \frac{\partial^2}{\partial Z^2}\langle h_z\sin\psi\rangle\right.$$
$$\left. + \frac{\partial^2}{\partial Y\partial Z}(\langle h_z\cos\psi\rangle - \langle h_y\sin\psi\rangle)\right\},$$

$$\left(\nu^4\frac{\partial}{\partial T}+\nu^5\frac{\partial}{\partial\tau}\right)(\langle h_y\rangle-\nu^4 d_e^2\nabla_s^2\langle h_y\rangle)$$

$$+\nu^4 k_x\frac{\partial^2\langle h_x\rangle}{\partial Z^2}=\nu^5\nabla_s^2\langle h_y\rangle+\nu^6 C_0(1+d_e^2)\frac{\partial}{\partial Z}$$

$$\times\left\{\frac{\partial^2}{\partial Y^2}\langle h_y\cos\psi\rangle-\frac{\partial^2}{\partial Z^2}\langle h_z\sin\psi\rangle\right.\quad(83)$$

$$\left.+\frac{\partial^2}{\partial Y\partial Z}(\langle h_z\cos\psi\rangle-\langle h_y\sin\psi\rangle)\right\}$$

$$+\nu^6 d_e^2 C_0\frac{\partial}{\partial Z}\nabla_s^2\{\langle h_z\sin\psi\rangle-\langle h_y\cos\psi\rangle\},$$

$$\left(\nu^4\frac{\partial}{\partial T}+\nu^5\frac{\partial}{\partial\tau}\right)(\langle h_z\rangle-\nu^4 d_e^2\nabla_s^2\langle h_z\rangle)$$

$$-\nu^4 k_x\frac{\partial^2\langle h_x\rangle}{\partial Z^2}=\nu^5\nabla_s^2\langle h_z\rangle-\nu^6 C_0(1+d_e^2)\frac{\partial}{\partial Z}$$

$$\times\left\{\frac{\partial^2}{\partial Y^2}\langle h_y\cos\psi\rangle-\frac{\partial^2}{\partial Z^2}\langle h_z\sin\psi\rangle\right.\quad(84)$$

$$\left.+\frac{\partial^2}{\partial Y\partial Z}(\langle h_z\cos\psi\rangle-\langle h_y\sin\psi\rangle)\right\}$$

$$-\nu^6 d_e^2 C_0\frac{\partial}{\partial Y}\nabla_s^2\{\langle h_z\sin\psi\rangle-\langle h_y\cos\psi\rangle\},$$

where the averaging operation $\langle\ldots\rangle$ is given by formula (16) with the replacement of x by ψ.

We also average Eq. (81) with weighting functions of 1, $\sin\psi$, and $\cos\psi$. As a result, we obtain the equations

$$\nu^2\frac{\partial\langle h_y\rangle}{\partial Y}+\nu^2\frac{\partial\langle h_z\rangle}{\partial Z}=0,\quad(85)$$

$$\langle h_x\cos\psi\rangle-\nu^2\frac{\partial}{\partial Y}\langle h_y\sin\psi\rangle-\nu^2\frac{\partial}{\partial Z}\langle h_z\sin\psi\rangle=0,\quad(86)$$

$$\langle h_x\sin\psi\rangle+\nu^2\frac{\partial}{\partial Y}\langle h_y\cos\psi\rangle+\nu^2\frac{\partial}{\partial Z}\langle h_z\cos\psi\rangle=0.\quad(87)$$

We seek a solution to Eqs. (79)–(81) in the form of expansion (77) and require that the equations be satisfied through all orders in ν. Then, to zeroth order in ν, we get

$$\frac{k_z}{1+d_e^2}\frac{\partial}{\partial\psi}\hat{M}h_y^{(0)}+k_z\frac{\partial^2 h_z^{(0)}}{\partial\psi^2}=C_0\cos\psi\hat{M}h_x^{(0)},$$

$$-\frac{k_z}{1+d_e^2}\frac{\partial}{\partial\psi}\hat{M}h_z^{(0)}+k_z\frac{\partial^2 h_y^{(0)}}{\partial\psi^2}=C_0\sin\psi\hat{M}h_x^{(0)},\quad(88)$$

$$\frac{\partial h_x^{(0)}}{\partial\psi}=0.$$

The last of these equations gives $h_x^{(0)}=h_{sx}^{(0)}(Y,Z,T,\tau)$. To solve the remaining two equations, we multiply them by $\cos\psi$ and $\sin\psi$, respectively, and average over the period of ψ. This yields

$$\begin{aligned}k_z\langle h_y^{(0)}\sin\psi\rangle-k_z\langle h_z^{(0)}\cos\psi\rangle&=\frac{1}{2}C_0 h_{sx}^{(0)},\\ k_z\langle h_z^{(0)}\cos\psi\rangle-k_z\langle h_y^{(0)}\sin\psi\rangle&=\frac{1}{2}C_0 h_{sx}^{(0)}.\end{aligned}\quad(89)$$

Adding together these two equations results in $h_{sx}^{(0)}=0$, in which case the equations give

$$\langle h_y^{(0)}\sin\psi\rangle=\langle h_z^{(0)}\cos\psi\rangle.\quad(90)$$

Further, multiplying the first and second of Eqs. (88) by $\sin\psi$ and $\cos\psi$, respectively, and averaging over the period of ψ, we arrive at the equation

$$\langle h_y^{(0)}\cos\psi\rangle+\langle h_z^{(0)}\sin\psi\rangle=0.\quad(91)$$

Equations (90) and (91) hold if we set

$$\begin{aligned}h_y^{(0)}&=A_s^{(0)}\sin\psi-B_s^{(0)}\cos\psi,\\ h_z^{(0)}&=A_s^{(0)}\cos\psi+B_s^{(0)}\sin\psi,\end{aligned}\quad(92)$$

where the functions $A_s^{(0)}$ and $B_s^{(0)}$ depend only on the slow variables and are to be determined from the equations of the next order in ν.

In the first order in ν, the equations have the form

$$\frac{k_z}{1+d_e^2}\frac{\partial}{\partial\psi}\hat{M}h_y^{(1)}+k_z\frac{\partial^2 h_z^{(1)}}{\partial\psi^2}=C_0\cos\psi\hat{M}h_x^{(1)}-\frac{\partial^2 h_y^{(0)}}{\partial\psi^2},$$

$$-\frac{k_z}{1+d_e^2}\frac{\partial}{\partial\psi}\hat{M}h_z^{(1)}+k_z\frac{\partial^2 h_y^{(1)}}{\partial\psi^2}=C_0\sin\psi\hat{M}h_x^{(1)}-\frac{\partial^2 h_z^{(0)}}{\partial\psi^2},\quad(93)$$

$$\frac{\partial h_x^{(1)}}{\partial\psi}=0.$$

The last of these equations gives

$$h_x^{(1)}=h_{sx}^{(1)}(Y,Z,T,\tau).\quad(94)$$

Solving the remaining two equations in accordance with the procedure for finding a solution to the zero-order equations results in

$$A_s^{(0)} = 0, \quad B_s^{(0)} = C_0 h_{sx}^{(1)}. \tag{95}$$

Then, we have

$$h_y^{(0)} = -C_0 h_{sx}^{(1)} \cos\psi, \quad h_z^{(0)} = C_0 h_{sx}^{(1)} \sin\psi. \tag{96}$$

The functions $h_y^{(1)}$ and $h_z^{(1)}$ satisfy Eqs. (90) and (91) with the replacement of the superscript 0 by the superscript 1. Consequently, the first-order equations have the solution

$$\begin{aligned} h_y^{(1)} &= h_{sy}^{(1)} + A_s^{(1)} \sin\psi - B_s^{(1)} \cos\psi, \\ h_z^{(1)} &= h_{sz}^{(1)} + A_s^{(1)} \cos\psi + B_s^{(1)} \sin\psi, \end{aligned} \tag{97}$$

where the functions $h_{sy}^{(1)}$, $h_{sz}^{(1)}$, $A_s^{(1)}$, and $B_s^{(1)}$ depend only on the slow variables and are determined from the equations of higher orders in ν.

To second order in ν, Eqs. (79)–(81) yield

$$\begin{aligned} &\frac{k_z}{1+d_e^2}\frac{\partial}{\partial\psi}\hat{M}h_y^{(2)} + k_z\frac{\partial^2 h_z^{(2)}}{\partial\psi^2} = -k_x\frac{\partial^2 h_z^{(0)}}{\partial\psi\partial Z} - \frac{\partial^2 h_y^{(1)}}{\partial\psi^2} \\ &+ C_0\cos\psi\left[\hat{M}h_x^{(2)} - (1+d_e^2)\left(\frac{\partial h_z^{(0)}}{\partial Y} - \frac{\partial h_y^{(0)}}{\partial Z}\right)\right] \\ &- C_0\hat{L}\left[\hat{M}h_y^{(0)} + (1+d_e^2)\frac{\partial h_z^{(0)}}{\partial\psi}\right], \\ &-\frac{k_z}{1+d_e^2}\frac{\partial}{\partial\psi}\hat{M}h_z^{(2)} + k_z\frac{\partial^2 h_y^{(2)}}{\partial\psi^2} = -k_x\frac{\partial^2 h_y^{(0)}}{\partial\psi\partial Z} - \frac{\partial^2 h_z^{(1)}}{\partial\psi^2} \\ &+ C_0\sin\psi\left[\hat{M}h_x^{(2)} - (1+d_e^2)\left(\frac{\partial h_z^{(0)}}{\partial Y} - \frac{\partial h_y^{(0)}}{\partial Z}\right)\right] \\ &+ C_0\hat{L}\left[\hat{M}h_z^{(0)} - (1+d_e^2)\frac{\partial h_y^{(0)}}{\partial\psi}\right], \\ &\frac{\partial h_x^{(2)}}{\partial\psi} - C_0\frac{\partial h_{sx}^{(1)}}{\partial Y}\cos\psi + C_0\frac{\partial h_{sx}^{(1)}}{\partial Z}\sin\psi = 0. \end{aligned} \tag{98}$$

Integrating the last of these equations, we find

$$h_x^{(2)} = h_{sx}^{(2)} + C_0\left(\frac{\partial h_{sx}^{(1)}}{\partial Y}\sin\psi + \frac{\partial h_{sx}^{(1)}}{\partial Z}\cos\psi\right), \tag{99}$$

where $h_{sx}^{(2)} = h_{sx}^{(2)}(Y, Z, T, \tau)$. Solving the remaining two equations by the above procedure, we obtain

$$A_s^{(1)} = 0, \quad B_s^{(1)} = C_0\left(h_{sx}^{(2)} - k_x\frac{\partial h_{sx}^{(1)}}{\partial Z}\right), \tag{100}$$

which yields

$$\begin{aligned} h_y^{(1)} &= h_{sy}^{(1)} - C_0\left[h_{sx}^{(2)} - k_x\frac{\partial h_{sx}^{(1)}}{\partial Z}\right]\cos\psi, \\ h_z^{(1)} &= h_{sz}^{(1)} + C_0\left[h_{sx}^{(2)} - k_x\frac{\partial h_{sx}^{(1)}}{\partial Z}\right]\sin\psi. \end{aligned} \tag{101}$$

Applying the same solution procedure as that used in the three lowest orders, we arrive at

$$\begin{aligned} h_y^{(2)} &= h_{sy}^{(2)} + A_s^{(2)} \sin\psi - B_s^{(2)} \cos\psi, \\ h_z^{(2)} &= h_{sz}^{(2)} + A_s^{(2)} \cos\psi + B_s^{(2)} \sin\psi, \end{aligned} \tag{102}$$

where the functions $h_{sy}^{(2)}$, $h_{sz}^{(2)}$, $A_s^{(2)}$, and $B_s^{(2)}$ depend only on the slow variables.

In order to capture any significant effect of the primary helicon in Eqs. (82)–(84) for long-wavelength perturbations, we need to determine the functions $A_s^{(2)}$ and $B_s^{(2)}$. This can be done by solving the equations in the third order in ν:

$$\begin{aligned} &\frac{k_z}{1+d_e^2}\frac{\partial}{\partial\psi}\hat{M}h_y^{(3)} + k_z\frac{\partial^2 h_z^{(3)}}{\partial\psi^2} = -k_x\frac{\partial^2 h_z^{(1)}}{\partial\psi\partial Z} - \frac{\partial^2 h_y^{(2)}}{\partial\psi^2} \\ &+ C_0\cos\psi\left[\hat{M}h_x^{(3)} - (1+d_e^2)\left(\frac{\partial h_z^{(1)}}{\partial Y} - \frac{\partial h_y^{(1)}}{\partial Z}\right)\right] \\ &- C_0\hat{L}\left[\hat{M}h_y^{(1)} + (1+d_e^2)\frac{\partial h_z^{(1)}}{\partial\psi}\right], \\ &-\frac{k_z}{1+d_e^2}\frac{\partial}{\partial\psi}\hat{M}h_z^{(3)} + k_z\frac{\partial^2 h_y^{(3)}}{\partial\psi^2} = -k_x\frac{\partial^2 h_y^{(1)}}{\partial\psi\partial Z} - \frac{\partial^2 h_z^{(2)}}{\partial\psi^2} \\ &+ C_0\sin\psi\left[\hat{M}h_x^{(3)} - (1+d_e^2)\left(\frac{\partial h_z^{(1)}}{\partial Y} - \frac{\partial h_y^{(1)}}{\partial Z}\right)\right] \\ &+ C_0\hat{L}\left[\hat{M}h_z^{(1)} - (1+d_e^2)\frac{\partial h_y^{(1)}}{\partial\psi}\right], \\ &\frac{\partial h_x^{(3)}}{\partial\psi} + \frac{\partial h_{sy}^{(1)}}{\partial Y} - C_0\left(\frac{\partial h_{sx}^{(2)}}{\partial Y} - k_x\frac{\partial^2 h_{sx}^{(1)}}{\partial Y\partial Z}\right)\cos\psi \\ &+ \frac{\partial h_{sz}^{(1)}}{\partial Z} + C_0\left(\frac{\partial h_{sx}^{(2)}}{\partial Z} - k_x\frac{\partial^2 h_{sx}^{(1)}}{\partial Z^2}\right)\sin\psi = 0. \end{aligned} \tag{103}$$

The solution to the last equation has the form

$$h_x^{(3)} = h_{sx}^{(3)} + C_0\left[\left(\frac{\partial h_{sx}^{(2)}}{\partial Y} - k_x\frac{\partial^2 h_{sx}^{(1)}}{\partial Y\partial Z}\right)\sin\psi + \left(\frac{\partial h_{sx}^{(2)}}{\partial Z} - k_x\frac{\partial^2 h_{sx}^{(1)}}{\partial Z^2}\right)\cos\psi\right], \quad (104)$$

where $h_{sx}^{(3)} = h_{sx}^{(3)}(Y, Z, T, \tau)$. Substituting solutions (101), (102), and (104) into the first two of Eqs. (103) and using the above standard procedure yields

$$A_s^{(2)} = 0,$$
$$B_s^{(2)} = C_0\left[h_{sx}^{(3)} - \left(\frac{1}{2} + d_e^2\right)\left(\frac{\partial h_{sz}^{(1)}}{\partial Y} - \frac{\partial h_{sy}^{(1)}}{\partial Z}\right) - k_x\left(\frac{\partial h_{sx}^{(2)}}{\partial Z} - k_x\frac{\partial^2 h_{sx}^{(1)}}{\partial Z^2}\right)\right]. \quad (105)$$

In deriving expressions (105), we took into account the equations

$$\frac{\partial h_{sy}^{(j)}}{\partial Y} + \frac{\partial h_{sz}^{(j)}}{\partial Z} = 0, \quad j = (1, 2, \ldots), \quad (106)$$

which follow from Eq. (85).

We substitute Eqs. (94), (99), (101), (102), and (105) into Eqs. (82)–(84) and average the corresponding terms on the right-hand sides of the resulting equations. Then, to fifth order in ν, we obtain

$$\frac{\partial h_{sx}^{(1)}}{\partial T} + k_x\frac{\partial}{\partial Z}\left(\frac{\partial h_{sz}^{(1)}}{\partial Y} - \frac{\partial h_{sy}^{(1)}}{\partial Z}\right) = 0,$$
$$\frac{\partial h_{sy}^{(1)}}{\partial T} + k_x\frac{\partial^2 h_{sx}^{(1)}}{\partial Z^2} = 0, \quad \frac{\partial h_{sz}^{(1)}}{\partial T} - k_x\frac{\partial^2 h_{sx}^{(1)}}{\partial Y\partial Z} = 0. \quad (107)$$

As will be shown below, these equations describe a long-wavelength helicon. In the next (sixth) order in ν, the averaged equations describe the evolution of the long-wavelength field $\mathbf{h}_s^{(1)}$ on the dissipative time scale and have the form

$$\frac{\partial h_{sx}^{(1)}}{\partial\tau} + \frac{\partial h_{sx}^{(2)}}{\partial T} + k_x\frac{\partial}{\partial Z}\left(\frac{\partial h_{sz}^{(2)}}{\partial Y} - \frac{\partial h_{sy}^{(2)}}{\partial Z}\right) = \nabla_s^2 h_{sx}^{(1)},$$
$$\frac{\partial h_{sy}^{(1)}}{\partial\tau} + \frac{\partial h_{sy}^{(2)}}{\partial T} + k_x\frac{\partial^2 h_{sx}^{(2)}}{\partial Z^2} = \nabla_s^2 h_{sy}^{(1)} - \frac{1}{2}C_0^2(1 - d_e^2)\nabla_s^2\frac{\partial h_{sx}^{(1)}}{\partial Z},$$
$$\frac{\partial h_{sz}^{(1)}}{\partial\tau} + \frac{\partial h_{sz}^{(2)}}{\partial T} - k_x\frac{\partial^2 h_{sx}^{(2)}}{\partial Y\partial Z} = \nabla_s^2 h_{sz}^{(1)} + \frac{1}{2}C_0^2(1 - d_e^2)\nabla_s^2\frac{\partial h_{sx}^{(1)}}{\partial Y}. \quad (108)$$

The main difference between these averaged equations and the equations for the helical flow considered in the previous section is that the nonlinear effect of the primary helicon on the x component of the long-wavelength field $\mathbf{h}_s^{(1)}$ (i.e., on the component of the magnetic field $\mathbf{b}_s^{(1)}$ of the long-wavelength perturbation that is parallel to the wave vector of the primary helicon) does not appear in the averaged equations. Hence, we can conclude that the components of the long-wavelength field are coupled to each other only because of the presence of an external magnetic field.

Further analysis of the equations obtained can be simplified by taking into account Eq. (106) and introducing the flux functions $\phi_s^{(j)}$ ($j = 1, 2$) such that $h_{sy}^{(j)} = \partial\phi_s^{(j)}/\partial Z$ and $h_{sz}^{(j)} = -\partial\phi_s^{(j)}/\partial Y$. In this way, Eqs. (107) and (108) reduce to

$$\frac{\partial h_{sx}^{(1)}}{\partial T} - k_x\nabla_s^2\frac{\partial\phi_s^{(1)}}{\partial Z} = 0, \quad \frac{\partial\phi_s^{(1)}}{\partial T} + k_x\frac{\partial h_{sx}^{(1)}}{\partial Z} = 0, \quad (109)$$

$$\frac{\partial h_{sx}^{(1)}}{\partial\tau} + \frac{\partial h_{sx}^{(2)}}{\partial T} - k_x\nabla_s^2\frac{\partial\phi_s^{(2)}}{\partial Z} = \nabla_s^2 h_{sx}^{(1)},$$
$$\frac{\partial\phi_s^{(1)}}{\partial\tau} + \frac{\partial\phi_s^{(2)}}{\partial T} + k_x\frac{\partial h_{sx}^{(2)}}{\partial Z} = \nabla_s^2\phi_s^{(1)} - \frac{1}{2}C_0^2(1 - d_e^2)\nabla_s^2 h_{sx}^{(1)}. \quad (110)$$

We look for a solution to Eqs. (109) and (110) in the form of

$$(\phi_s^{(j)}, h_{sx}^{(j)}) \sim \exp(-i\omega T + \gamma\tau + iq_y Y + iq_z Z), \quad j = (1, 2). \quad (111)$$

Then, from Eq. (109), we obtain

$$\omega = \pm k_x q_z q, \quad \phi_s^{(1)} = \pm h_{sx}^{(1)}/q, \quad q = \sqrt{q_y^2 + q_z^2}. \quad (112)$$

Recalling definitions (75) and (76), we find that, in the coordinate system $(\bar{x}\bar{y}\bar{z})$, the vector $\mathbf{q}$ has, by virtue of representations (111), only two components, q_y and q_z, while, in the initial coordinate system (xyz), it has all three components, $\mathbf{q} = (-k_z q_z, q_y, k_x q_z)$. Note that we assumed that $\mathbf{k}\cdot\mathbf{q} = 0$, i.e., that the wave vector of the long-wavelength perturbation is perpendicular to the wave vector of the primary helicon. By what has been said above, we have $\mathbf{q}\cdot\mathbf{e}_z = k_x q_z$; hence, dispersion relation (112) describes a long-wavelength helicon [cf. dispersion relation (112) versus dispersion relations (5) and (73), in view of $qd_e \ll 1$]. The plus and minus signs in dispersion relation (112) correspond to helicons propagating in opposite directions.

Combining Eqs. (110) and substituting Eqs. (112) yield the following expression for the growth (damp-

ing) rate of the long-wavelength helicons described by dispersion relation (112):

$$\gamma = -q^2 \pm \frac{1}{4}C_0^2(1-d_e^2)q^3, \qquad (113)$$

where the sign should be taken to be the same as that in dispersion relation (112). Expression (113) implies that, regardless of the value of d_e ($d_e > 1$ or $d_e < 1$), one of the two long-wavelength helicons corresponding to the plus or minus sign in dispersion relation (112) is unstable under the condition

$$\frac{1}{4}C_0^2|1-d_e^2|q > 1. \qquad (114)$$

If we go back to the initial variables (prior to introducing the ordering) and consider perturbations of the form $\sim\exp(-i\omega t + iq_y\bar{y} + iq_z\bar{z})$, then, recalling the ordering used above, we can combine dispersion relation (112) and expression (113) into the following asymptotic dispersion relation:

$$\omega = \pm\left[k_x q_z q + \frac{1}{4}i\frac{C_0^2}{\nu}(1-d_e^2)q^3\right] - i\nu q^2, \qquad (115)$$

in which it is assumed that $q \simeq \nu^2$ and $\omega \simeq \nu^4$. Accordingly, the instability criterion for the helicon takes the form

$$C_0^2|1-d_e^2|q/4\nu^2 > 1. \qquad (116)$$

This criterion shows that the instability has a threshold in q.

5. DISCUSSION OF THE RESULTS AND CONCLUSIONS

The stability of several types of steady-state periodic flows against long-wavelength perturbations has been investigated by solving the resistive EMHD equations under the assumption that the resistive damping of the primary flow is balanced by an energy supply from a special constant external source. In particular, it is shown that long-wavelength perturbations of the Kolmogorov-type flow are unstable when the magnetic Reynolds number of the flow exceeds a critical value, $Re_m > Re_m^{cr} = \sqrt{2/(1+d_e^2)}$. This criterion is qualitatively identical to the instability criteria for a Kolmogorov flow in incompressible hydrodynamics and for drift waves (Rossby waves) [1, 4, 6]. The most unstable perturbations are those with $q_y = 0$, i.e., with a wave vector perpendicular to the velocity vector $\mathbf{v}_e$ of the primary flow, in which case the only growing component of the long-wavelength magnetic field is the component directed along the wave vector of the primary flow. In the equation for this magnetic field component, the instability mechanism is the effect of negative resistivity due to the primary periodic flow. The results obtained numerically agree well with analytical results in the parameter range in which the latter are applicable. Beyond the scope of analytic approximations, the perturbations become stable when the perturbation wavenumbers are comparable with the wavenumber of the flow, $q \simeq k_0$.

In the case of a helical flow (similar to a Beltrami flow), it has been found that, for $d_e < 1$, the primary flow has a destabilizing effect on the long-wavelength perturbations. This effect is proportional to the microhelicity of the flow, $\mathbf{B}^0 \cdot (\nabla \times \mathbf{B}^0)$. However, the asymptotic dispersion relation obtained above differs significantly from that for the Beltrami flow in hydrodynamics. The effect produced by microhelicity is proportional to q^3, and the instability criterion not only includes the amplitude of the primary flow but also sets an instability threshold from below on the perturbation wavenumber; specifically, perturbations with $1 \gg q > 2\nu^2/\sqrt{1-d_e^4}$ are growing. In the opposite case $d_e > 1$, a helical flow is stable against long-wavelength perturbations. Numerical analysis of the problem shows that, along with the instability threshold from below on q (which agrees with the predictions of analytic theory), there is the instability threshold from above, $q \le k_0$ (for perturbation wavenumbers comparable with the wavenumber of the flow). In addition, numerical simulations provide clear evidence that, for long-wavelength perturbations, there exists a stability boundary in terms of the quantity d_e; specifically, for $d_e \ge 1$, the perturbations of a helical flow become stable, which agrees with the theory developed here.

It is shown that, in the case of an anisotropic helical flow, the primary flow leads to the effect of negative resistivity (because of the anisotropy of the magnetic field) and to the effect associated with the microhelicity of the flow in the equations for long-wavelength perturbations. When the magnetic Reynolds number is large and the anisotropy is small, $|(B_y^0)^2 - (B_z^0)^2| \simeq Re_m^{-2} \ll 1$, these effects are of comparable importance. When the anisotropy $|(B_y^0)^2 - (B_z^0)^2|$ is large, it plays a dominant role and the stability criterion for an anisotropic helical flow is analogous to that for a Kolmogorov-type flow. Numerical calculations of the growth rate of the perturbation as a function of the degree of anisotropy of the flow are in good agreement with the expressions obtained analytically.

The EMHD equations for a plasma in an external magnetic field have solutions describing running waves with a nonzero frequency and nonzero microhelicity, which are called helicons. Assuming that the amplitude of the helicon is kept constant by an external source, we have shown that the effect of a primary small-scale helicon on a secondary long-wavelength helicon is analogous to the effect of a helical flow on long-wavelength perturbations and is proportional to the microhelicity of the primary helicon. It has been found that, in contrast

to the case of a steady-state helical flow, the only magnetic field components of a long-wavelength helicon that are affected by the microhelical nature of the helicon are those perpendicular to the wave vector of the primary helicon. Because of this effect, which is destabilizing regardless of the value of d_e, the primary helicon is unstable against long-wavelength helicons with $1 > q \geq 4\nu^2/C_0^2|1 - d_e^2| = 4/Re_m^2|1 - d_e^2|$.

Hence, we can conclude that periodic flows described by the corresponding solutions to the EMHD equations tend to become unstable against long-wavelength perturbations, which indicates cascading of the energy toward large scales (an inverse cascade). This conclusion agrees with the results of [16, 17, 19], where it was shown that, in electron magnetohydrodynamics, large-scale perturbations can be generated by small-scale turbulence, as well as with the numerical results of [20] and analytic estimates of [21], which show the possible existence of inverse cascades in two-dimensional electron magnetohydrodynamics. Accordingly, we can suggest that small-scale electron motions initiated, e.g., by electron cyclotron resonance heating or the effect of laser radiation may influence long-scale phenomena in a plasma. However, this suggestion requires more detailed analysis, which should involve not only electron but also ion dynamics.

All of the results obtained here are valid for a plasma with a finite (although high) conductivity and, unlike in incompressible hydrodynamics, it seems to be impossible (at least at present) to generalize them to the case of infinite plasma conductivity in ideal electron magnetohydrodynamics.

ACKNOWLEDGMENTS

We would like to thank Prof. T.J. Schep for fruitful discussions. This work was supported in part by the Netherlands Organization for Scientific Research (NWO), project no. 047.009.007. V.P. Lakhin is grateful to the Council on the Grants of the President of the Russian Federation and the Council of the Federal Program "Government Support of the Leading Scientific Schools" (project no. 00-15-96526). The work of V.D. Levchenko was supported in part by the Russian Foundation for Promotion of Science.

REFERENCES

1. L. D. Meshalkin and Ya. G. Sinai, Prikl. Mat. Mekh. **25**, 1700 (1961).
2. J. S. A. Green, J. Fluid Mech. **62**, 273 (1974).
3. G. Sivashinsky and V. Yakhot, Phys. Fluids **28**, 1040 (1985).
4. A. Libin, G. Sivashinsky, and E. Levich, Phys. Fluids **30**, 2984 (1987).
5. B. Dubrulle and U. Frisch, Phys. Rev. A **43**, 5355 (1991).
6. A. V. Tur, A. V. Chechkin, and V. V. Yanovsky, Phys. Fluids B **4**, 3513 (1992).
7. B. J. Bayly and V. Yakhot, Phys. Rev. A **34**, 381 (1986).
8. H. K. Moffat, J. Fluid Mech. **166**, 359 (1986).
9. A. A. Nepomnyashchiĭ, Prikl. Mat. Mekh. **40**, 886 (1976).
10. G. Sivashinsky, Physica D (Amsterdam) **17**, 243 (1985).
11. A. A. Chernov and V. V. Yan'kov, Fiz. Plazmy **8**, 931 (1982) [Sov. J. Plasma Phys. **8**, 522 (1982)].
12. B. N. Kuvshinov, T. J. Schep, M. Berning, and E. Westerhof, Phys. Lett. A **241**, 287 (1998).
13. V. M. Yakovenko, Zh. Éksp. Teor. Fiz. **57**, 556 (1969) [Sov. Phys. JETP **30**, 315 (1970)].
14. A. S. Kingsep, K. V. Chukbar, and V. V. Yan'kov, in *Reviews of Plasma Physics*, Ed. by B. B. Kadomtsev (Énergoizdat, Moscow, 1987; Consultants Bureau, New York, 1990), Vol. 16.
15. M. B. Isichenko and A. M. Marnachev, Zh. Éksp. Teor. Fiz. **93**, 1244 (1987) [Sov. Phys. JETP **66**, 702 (1987)].
16. V. P. Lakhin and S. S. Moiseev, Phys. Lett. A **263**, 386 (1999).
17. S. I. Vainshtein, Ya. B. Zel'dovich, and A. A. Ruzmaikin, *Turbulent Dynamo in Astrophysics* (Nauka, Moscow, 1980), p. 208.
18. M. Steenbeck, F. Krause, and K.-H. Rädler, Z. Naturforsch. **21A**, 369 (1966).
19. V. P. Lakhin, S. S. Moiseev, and T. J. Schep, Phys. Chem. Earth **25**, 769 (2000).
20. D. Biskamp, E. Schwarz, A. Zeiler, *et al.*, Phys. Plasmas **6**, 751 (1999).
21. E. Westerhof, B. N. Kuvshinov, V. P. Lakhin, *et al.*, in *Proceedings of the 26th EPS Conference on Controlled Fusion and Plasma Physics, Maastricht, 1999*, ECA **23J**, p. 29.

Translated by I.A. Kalabalyk

Plasma Physics Reports, Vol. 29, No. 4, 2003, pp. 346–354. Translated from Fizika Plazmy, Vol. 29, No. 4, 2003, pp. 376–384.

LOW-TEMPERATURE PLASMA

Theory of the Acoustic Instability and Behavior of the Phase Velocity of Acoustic Waves in a Weakly Ionized Plasma

O. S. Torosyan and A. R. Mkrtchyan

Institute of Applied Problems of Physics, National Academy of Sciences of Armenia, Nersesyan str. 25, Yerevan, 375014 Armenia

Received May 15, 2002; in final form, August 29, 2002

Abstract—The amplification of acoustic waves due to the transfer of thermal energy from electrons to the neutral component of a glow discharge plasma is studied theoretically. It is shown that, in order for acoustic instability (sound amplification) to occur, the amount of energy transferred should exceed the threshold energy, which depends on the plasma parameters and the acoustic wave frequency. The energy balance equation for an electron gas in the positive column of a glow discharge is analyzed for conditions typical of experiments in which acoustic wave amplification has been observed. Based on this analysis, one can affirm that, first, the energy transferred to neutral gas in elastic electron–atom collisions is substantially lower than the threshold energy for acoustic wave amplification and, second, that the energy transferred from electrons to neutral gas in inelastic collisions is much higher than that transferred in elastic collisions and thus may exceed the threshold energy. It is also shown that, for amplification to occur, there should exist some heat dissipation mechanism more efficient than gas heat conduction. It is suggested that this may be convective radial mixing within a positive column due to acoustic streaming in the field of an acoustic wave. The features of the phase velocity of sound waves in the presence of acoustic instability are investigated. © *2003 MAIK "Nauka/Interperiodica"*.

1. INTRODUCTION

It is well known that acoustic waves in a weakly ionized plasma may become unstable under conditions in which the electron temperature is higher than that of the neutral particles ($T_e \gg T$) [1–5]. On the other hand, the experimental values of the amplification factor for acoustic waves in an atomic gas-discharge plasma are known to differ greatly from those predicted theoretically on the basis of the dispersion relations derived in [1–5]; specifically, they are much larger than the theoretical ones (see [6–12]). Moreover, in our earlier paper [11], it was shown that, when all the possible mechanisms for the dissipation of the acoustic wave energy are taken into account, the theories constructed in [1–5] fail to explain the experimentally observed amplification of acoustic waves in the positive column of a glow discharge [6–12] because the damping of waves always prevails over their growth, which makes the wave amplification impossible. That is why, in [11], an attempt was made to clarify the reasons for such a large discrepancy between the theoretical and experiments results. First, it was shown that the energy transferred to a neutral gas from the hotter electrons in elastic electron–atom collisions (in [1–5], this energy transfer was regarded to be an energy source for acoustic instability, i.e., sound amplification) was not enough to ensure that the value of the theoretical amplification factor coincide in order of magnitude with the measured values. Second, it was found that the thermal energy transfer to neutral gas in inelastic collisions of the second kind (superelastic collisions) between excited atoms and atoms in the ground state could far exceed the energy transfer in elastic electron–atom collisions. However, in [11], it was also shown that the high specific power of heat release in a neutral gas was still not enough to provide acoustic wave amplification because, in this case, the amplification was prevented by strong gas heating. In view of this fact, in [11], we suggested the existence of a heat dissipation mechanism that is more efficient than atomic heat conduction and impedes strong gas heating, thus providing the possibility of acoustic wave amplification in plasma. In our opinion, the convective mixing of a plasma in the radial direction due to acoustic streaming arising under the action of an acoustic wave [13] may serve as such an additional strong mechanism. In the present paper, a simplifying assumption is made that the radial heat flux to the tube wall due to this heat dissipation mechanism ("acoustic" heat conduction) is proportional to the difference between the mean gas temperature and the temperature of the wall. It is shown that the allowance for both heat dissipation mechanisms (the conventional one and acoustic heat conduction) may provide thermal conditions in the positive column of a glow discharge under which the theoretical values of the amplification factor coincide with the experimental ones. In this case, the acoustic thermal conductivity should be higher than the conventional one by one order of magnitude. Based on the results obtained, a conclusion is drawn that, in a weakly ionized plasma with $T_e \gg T$, an acoustic wave can be amplified when two conditions are simultaneously satisfied: the heat release in the neutral plasma component

1063-780X/03/2904-0346$24.00

is sufficiently large and an efficient heat dissipation mechanism preventing strong gas heating is present.

Here, we also study the behavior of the phase velocity of acoustic waves under the conditions of acoustic instability in a weakly ionized plasma. The analysis is carried out based on the dispersion relation derived in [11]. However, in contrast to [11], the equilibrium gas temperature is described by the equation for heat balance in a cylindrical discharge tube with allowance for heat dissipation due to both the conventional and acoustic heat conduction. It is shown that, under acoustic instability, the phase velocity of acoustic waves increases with increasing specific power of heat release (discharge current density) in the neutral plasma component because of the following two effects: (i) the equilibrium gas temperature increases and (ii) an acoustic wave perturbs both the density of the neutral gas and the electron density, thereby modulating the heat exchange between the electrons and neutral gas in such a way that both the intensity of the wave and its phase velocity increase. Note that Ishida and Idehara [14] attempted to experimentally reveal how the electron energy transfer to neutral gas affects the phase velocity of sound waves. The results obtained in our study may help to explain why their attempt was unsuccessful. This effect manifests itself only under the conditions of acoustic instability for low-frequency sound waves (see below). When the conditions in a gas-discharge plasma permit sound amplification, the phase velocity of the waves can become higher than the adiabatic sound velocity (see below), which is determined by the equilibrium gas temperature. The experiments reported in [14] were carried out at a very high frequency (17 kHz), at which sound waves cannot be amplified and the effect in question does not come into play. It is precisely for this reason that the experiments of [14] failed to reveal the influence of the electron energy transfer on the sound velocity in a weakly ionized plasma.

2. DISPERSION RELATION

We start with the following dispersion relation for a plane acoustic wave propagating along the axis of a discharge tube [11]:

$$K^4 + (A + iB)K^2 + A_1 + iB_1 = 0, \tag{1}$$

where K is the wavenumber and the coefficients A, B, A_1, and B_1 are related to the plasma parameters by [11]

$$A = -\frac{\overline{\nabla^2 T}}{\bar{T}} + \frac{2Q}{a(\bar{T})^2} + \left[\frac{b}{a(\bar{T})^2} - \frac{m_n}{k_B\bar{T}}\right]\omega^2, \tag{2}$$

$$B = -\frac{5}{2}\frac{k_B N_n}{a\bar{T}}\omega, \tag{3}$$

$$A_1 = \frac{m_n\overline{\nabla^2 T}}{k_B(\bar{T})^2}\omega^2 - \frac{3}{2}\frac{m_n b}{a k_B(\bar{T})^3}\omega^4, \tag{4}$$

$$B_1 = \frac{3}{2}\frac{m_n N_n}{a(\bar{T})^2}\omega^3. \tag{5}$$

Here, the equilibrium (in the absence of acoustic perturbations) temperature T of the neutral gas depends only on the distance r from the symmetry axis of the tube by virtue of the cylindrical symmetry of the tube and because the length of the positive column is assumed to be much larger than its radius. The equation for determining the temperature T will be given below. The averaged values $\bar{T}$ and $\overline{\nabla^2 T}$ are defined as

$$\bar{T} = \frac{2}{R_0^2}\int_0^{R_0} rT(r)dr, \tag{6}$$

$$\overline{\nabla^2 T} = \frac{2}{R_0^2}\int_0^{R_0} r\nabla^2 T(r)dr, \tag{7}$$

where R_0 is the tube radius and ∇^2 is the Laplace operator. Also, in formulas (2)–(5), Q is the specific power of heat release in a neutral gas, the quantity a is related to the thermal conductivity $\chi(T)$ by $\chi(T) = aT$, $b = (4/3)\eta + \xi$, η and ξ are the first and second viscosity coefficients, m_n is the mass of a gas atom, k_B is Boltzmann's constant, ω is the frequency of acoustic waves, and N_n is the density of neutral atoms.

We assume that the frequency ω in dispersion relation (1) is real and investigate the imaginary and real parts of the wavenumber K, which determine the attenuation (or amplification) factors of the wave and its phase velocity. In this case, in the positive column of a gas-discharge plasma, there may exist two different waves that propagate in each direction along the tube axis and correspond to two solutions K^2 of biquadratic equation (1). The acoustic wave is described by the solution [11]

$$K = \frac{1}{2}\left[\sqrt{-(A + iB) + 2\sqrt{A_1 + iB_1}}\right. \\ \left. - \sqrt{-(A + iB) - 2\sqrt{A_1 + iB_1}}\right]. \tag{8}$$

3. EQUILIBRIUM TEMPERATURE OF THE NEUTRAL GAS

The equilibrium gas temperature $T(r)$ is determined from the following time-independent heat balance equation for the gas component of the positive column in a cylindrical discharge tube:

$$\frac{1}{r}\frac{d}{dr}\left(\chi(T)r\frac{dT}{dr}\right) + Q - L = 0; \tag{9}$$

where L is the heat dissipation power per unit plasma volume due to the radial gas mixing by an acoustic streaming induced by a sound wave. The radial heat transfer by such mixing in the discharge tube can be defined as the product

$$q = \alpha(\bar{T} - T_w). \quad (10)$$

Here, q is the density of the heat flux to the tube wall; α is the so-called acoustic heat transfer coefficient; and T_w is the wall temperature, which is assumed to be equal to the temperature of the surrounding medium. Using definition (10), we can calculate the rate of energy loss through the tube wall due to acoustic heat transfer. Dividing the rate so obtained by the tube volume, we arrive at the expression for L:

$$L = \frac{2\alpha}{R_0}(\bar{T} - T_w). \quad (11)$$

Note that dispersion relation (1), coefficients (2)–(5), and Eq. (9) were derived under the assumption that the wavelength of the sound wave was larger than the discharge tube radius and smaller than the tube length; hence, in the expressions for coefficients (2)–(5) in dispersion relation (1), we can average the temperature over the tube cross section. Moreover, since, in this case, the acoustic perturbation of $\bar{T}$ is equal to zero, the perturbation of L is also equal to zero. Consequently, the allowance for the acoustic heat removal does not change the form of dispersion relation (1) and coefficients (2)–(5). However, this heat dissipation will affect the propagation of acoustic waves in the discharge tube, because L enters Eq. (9) for the equilibrium temperature T, through which, according to formulas (6) and (7), the quantities $\bar{T}$ and $\overline{\nabla^2 T}$ are determined. Note that Eq. (9) can also be obtained as a zero-order approximation in the linearization of the general nonlinear heat balance equation for a neutral gas in acoustic perturbations.

Assuming that the intensity of the internal heat sources (current density) is distributed uniformly over the cross section of the tube (i.e., that Q is independent of r) and taking into account the above expressions for $\chi(T)$ and L, we readily find the solution to Eq. (9) that is finite at $r = 0$ and satisfies the condition $T = T_0$ at $r = R_0$:

$$T(r) = \sqrt{T_0^2 + \frac{1}{2a}\left[Q - \frac{2\alpha(\bar{T} - T_w)}{R_0}\right](R_0^2 - r^2)}. \quad (12)$$

Note that this radial temperature profile depends on the mean value $\bar{T}$, which, in turn, is determined in terms of the temperature $T(r)$ by means of relationship (6). In order to determine $\bar{T}$, we multiply solution (12) by r and integrate it over dr from 0 to R_0. Taking into account relationship (6) and performing simple manipulations, we arrive at the following algebraic equation for $\bar{T}$:

$$\bar{T} = \frac{2}{3R_0^2(K_1 - K_2\bar{T})}\{[T_0^2 + R_0^2(K_1 - K_2\bar{T})]^{3/2} - T_0^3\}, \quad (13)$$

where

$$K_1 = \frac{Q}{2a} + K_2 T_w, \quad (14)$$

$$K_2 = \frac{\alpha}{aR_0}. \quad (15)$$

The quantity $\overline{\nabla^2 T}$ in coefficients (2)–(5) can easily be calculated using formulas (7) and (12). Performing the corresponding manipulations yields

$$\overline{\nabla^2 T} = -\frac{2}{T_0}(K_1 - K_2\bar{T}). \quad (16)$$

Having solved Eq. (13) numerically with respect to $\bar{T}$ and having found $\overline{\nabla^2 T}$ from expression (16), we can use coefficients (2)–(5) to investigate the imaginary and real parts of the wavenumber K from formula (8) in terms of the plasma parameters. To do this, we introduce the notation $V_f = \omega/\mathrm{Re}K$ and $\beta = -\mathrm{Im}K$, where V_f is the wave phase velocity and β is the amplification or attenuation factor (plus or minus, respectively). If an acoustic wave propagating in the positive direction of the Z-axis (the symmetry axis of the tube); i.e., its spatial dependence is described by the function $\exp(ikz)$, then the positive values $\beta > 0$ correspond to amplification and the negative values $\beta < 0$ correspond to attenuation.

Then, we denote by C_S the adiabatic acoustic velocity, $C_S^2 = (\partial p/\partial\rho)_S = \gamma(\partial p/\partial\rho)_T$, where γ is the ratio of the specific heat capacities, $\gamma = C_P/C_V$. For an ideal gas, we have $C_S^2 = \gamma k_B T/m_n$. Numerical calculations for argon give the following expression for C_S:

$$C_S = 18.63\sqrt{\bar{T}}\ \mathrm{m/s}, \quad (17)$$

where $\bar{T}$ is in kelvin.

It should be noted that, in dispersion relation (1) with coefficients (2)–(5), all of the mechanisms for the dissipation of the energy of acoustic waves are take into account, except for the collisional mechanism and wave absorption at the tube wall. For the above values of the plasma parameters, the collisional damping of acoustic waves is far weaker than that due to the presence of the tube wall [2]. Hence, collisional attenuation can be neglected and, accordance to [1], the coefficient β_1 of acoustic wave absorption at the wall ($R_0 = 2$ cm) in the case of argon can be written as

$$\beta_1 = 0.21\mathrm{Re}K\sqrt{\frac{\bar{T}}{\omega}}\ \mathrm{m}^{-1}, \quad (18)$$

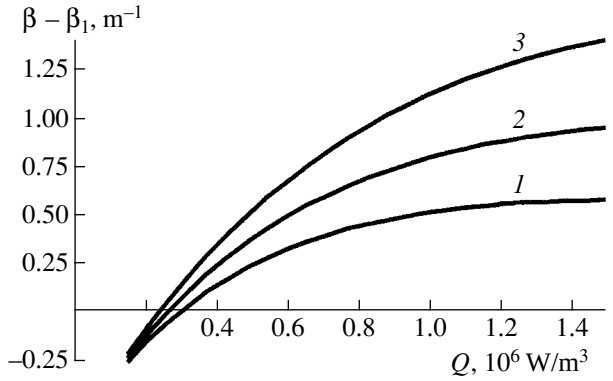

Fig. 1. Amplification factor $\beta - \beta_1$ vs. Q for α = (*1*) 40, (*2*) 60, and (*3*) 100 W/(m^2 K). The remaining parameters are $\omega/2\pi$ = 500 Hz, $N_e = 10^{10}$ cm^{-3}, $N_n = 10^{17}$ cm^{-3}, R_0 = 2 cm, T_e = 2 eV, and T_w = 300 K.

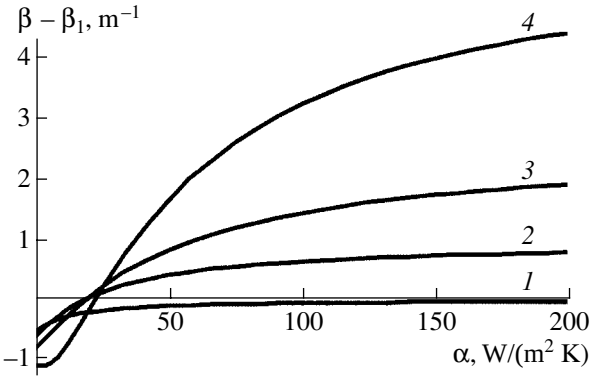

Fig. 2. Amplification factor $\beta - \beta_1$ vs. α for Q = (*1*) 2×10^5, (*2*) 5.5×10^5, and (*3*, *4*) 1.5×10^6 W/m^3. The remaining parameters are the same as in Fig. 1, except for the T_w value for curve *4* (T_w = 77 K).

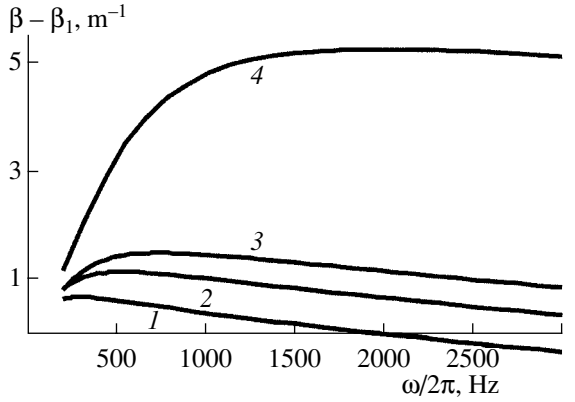

Fig. 3. Amplification factor $\beta - \beta_1$ vs. frequency for Q = (*1*) 5.5×10^5, (*2*) 10^6, and (*3*, *4*) 1.5×10^6 W/m^3. The other parameters are α = 100 W/(m^2 K) and T_w = (*1*, *2*, *3*) 300 and (*4*) 77 K. The remaining parameters are the same as in Fig. 1.

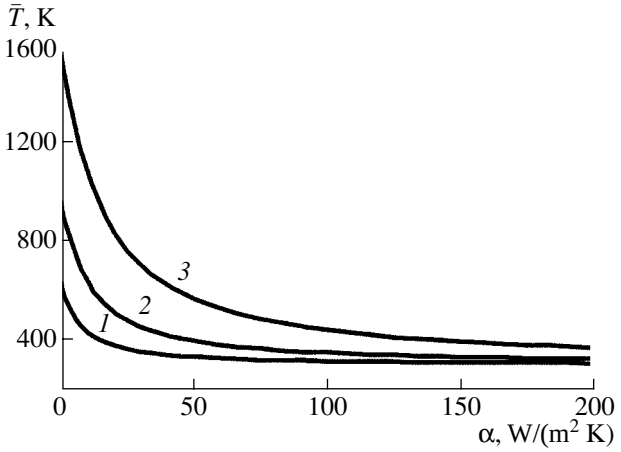

Fig. 4. Mean temperature of the neutral gas vs. α for Q = (*1*) 2×10^5, (*2*) 5.5×10^5, and (*3*) 1.5×10^6 W/m^3. The remaining parameters are the same as in Fig. 1.

where ω is in rad/s and $\bar{T}$ is in kelvin. When the absorption of acoustic waves at the wall of the gas-discharge tube is taken into account, the amplification of the wave corresponds to the condition $\beta - \beta_1 > 0$. Finally, we note that, in our numerical calculations, we set $T_0 = T_w$.

4. RESULTS AND DISCUSSION

4.1. Amplification Factor for Acoustic Waves

Figures 1–3 show the amplification factor $\beta - \beta_1$ calculated using formulas (8) and (18) as a function of the specific power Q of heat release in a neutral gas, the acoustic heat transfer coefficient α, and the frequency ω of acoustic waves for an argon gas-discharge plasma. It is seen that there are thresholds in terms of Q (Fig. 1) and α (Fig. 2) for an acoustic wave to be amplified (i.e., for the quantity $\beta - \beta_1$ to be positive). The thresholds should in principle depend on the plasma parameters. According to Fig. 1, the threshold value of Q is weakly dependent on α, whereas the threshold value of α is almost independent of Q (see Fig. 2, curves *2*, *3*). Curves *4* in Figs. 2 and 3 refer to the case in which the wall of the discharge tube is at the temperature of liquid nitrogen. In this case, the amplification factor $\beta - \beta_1$ is seen to be substantially larger, which agrees with the data obtained by Hasegawa [7] in his experiments on the amplification of acoustic waves in a discharge tube immersed in liquid nitrogen. A comparison of Fig. 4, which illustrates how the temperature $\bar{T}$ depends on α for different powers Q deposited in the discharge, with

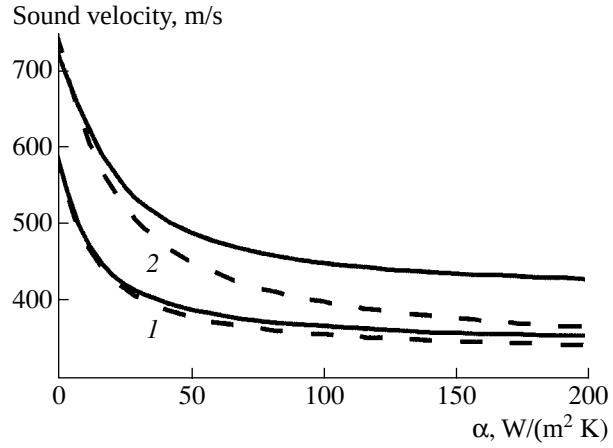

Fig. 5. Phase velocity V_f (solid curves) and adiabatic velocity C_s (dashed curves) of sound waves as functions of α for Q = (*1*) 5.5×10^5 and (*2*) 1.5×10^6 W/m^3. The remaining parameters are the same as in Fig. 1.

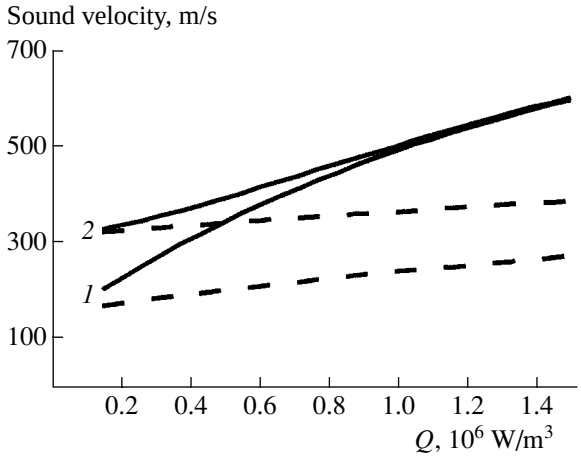

Fig. 6. Phase velocity V_f (solid curves) and adiabatic velocity C_S (dashed curves) of sound waves as functions of Q for different temperatures of the discharge tube wall, T_w = (*1*) 77 and (*2*) 300 K. The other parameters are $\omega/2\pi$ = 200 Hz and α = 100 W/(m^2 K). The remaining parameters are the same as in Fig. 1.

Figs. 1 and 2 shows that the thermal regime of the positive discharge column plays an important role in the acoustic wave amplification. In fact, according to Fig. 2, sound waves cannot be amplified at small α values even when the Q values are fairly large. This is related to the fact that strong heating of the gas at small α values (Fig. 4) prevents the wave amplification. Consequently, we can conclude that acoustic instability (sound amplification) cannot occur in a gas-discharge plasma without efficient heat exchange with the surrounding medium, because the heat dissipation due to conventional heat conduction is not enough to provide cooling of the gas needed for the onset of instability. It should be stressed that an increase in $\beta - \beta_1$ with α (Fig. 2) is caused by cooling the gas (Fig. 4). Therefore, for a given Q value, the larger the value of α (the smaller the value of $\bar{T}$), the larger the amplification factor $\beta - \beta_1$ (Fig. 1). This allows us to conclude that cooling the gas promotes the onset of acoustic instability in a weakly ionized plasma. This conclusion is also supported by Figs. 2 and 3, in which curves *4* show that, in a tube immersed in liquid nitrogen, the amplification factor $\beta - \beta_1$ is considerably larger. Note that the quantity $\chi_{acoust} = \alpha(R/2)$ can be regarded as the acoustic thermal conductivity of a gas in a discharge tube. Then, using the threshold α value for acoustic wave amplification ($\approx$20 W/(m^2 K), see Fig. 2), we find that the threshold acoustic thermal conductivity at R_0 = 2 cm is approximately equal to $\chi_{acoust} \approx 0.2$ W/(m K). This value exceeds the conventional thermal conductivity of argon at the above temperatures by a factor of about 5–7. Hence, it is evident that acoustic heat conduction plays a greater role in the cooling of the positive column of a glow discharge than does conventional heat conduction.

4.2. Sound Velocity

Figures 5–7 show the phase and adiabatic velocities of sound waves, calculated as functions of α, Q, and ω by using formulas (8) and (17) in the case of a weakly ionized argon plasma. It is noteworthy that the phase velocity of sound waves is higher than the adiabatic velocity. According to Fig. 7, this is true only for low-frequency (up to 1–1.5 kHz) sound waves. Also, the higher the energy deposition in the neutral gas and the lower the mean gas temperature, the larger the difference between the phase and adiabatic velocities (Figs. 5, 6). Actually, this indicates that the difference

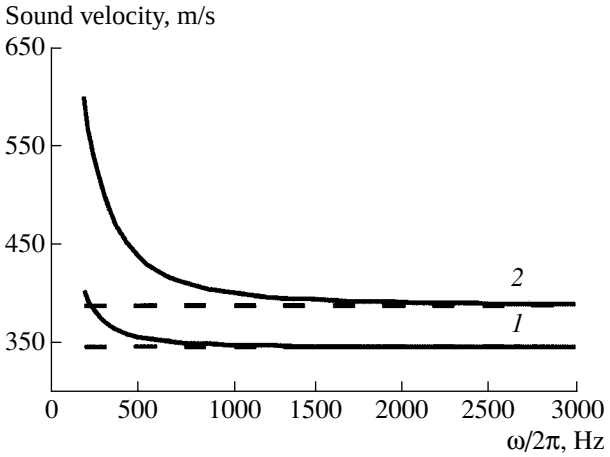

Fig. 7. Phase velocity V_f (solid curves) and adiabatic velocity C_S (dashed curves) of sound waves as functions of frequency for Q = (*1*) 5.5×10^5 and (*2*) 1.5×10^6 W/m^3. The other parameters are α = 100 W/(m^2 K) and T_w = 300 K. The remaining parameters are the same as in Fig. 1.

between the phase and adiabatic velocities of sound waves in the positive column of a discharge increases with the amplification factor $\beta - \beta_1$. Hence, we can conclude that this difference is due to the fact that the acoustic wave modulates the energy exchange between the hot electrons and the cold neutral gas in the discharge; this leads to acoustic instability (sound amplification) and an increase in the wave phase velocity. As a result, in a weakly ionized plasma at a proper modulation of the energy transfer from electrons to neutral particles by the acoustic wave, the intensity and phase velocity of sound waves increase. We note, however, that the phase velocity of the acoustic wave can also be weakly perturbed by electrons at small α values (Fig. 5), i.e., in the absence of acoustic wave amplification (Fig. 2). To summarize, we can state that the change in the phase velocity of acoustic waves with changing α and Q (see Figs. 5, 6) stems from two causes: first, the perturbation of acoustic waves by electrons, and, second, the change in the equilibrium temperature of the neutral gas with changing α and Q. The frequency dispersion of the phase velocity of acoustic waves (Fig. 7) is attributed exclusively to the effect of the electrons.

4.3. Energy Source for Acoustic Instability

In the theory of acoustic wave amplification [1–4], the energy source that drives the acoustic instability in a weakly ionized atomic plasma is the energy transferred from electrons to neutral atoms in elastic electron–atom collisions. However, it is easy to see that this energy is much lower than the threshold energy (Fig. 1) for acoustic wave amplification in a plasma. In fact, the rate of the thermal energy transfer from electrons to neutral atoms in elastic electron–atom collisions in a unit of plasma volume is described by the equation [15]

$$Q_e = \frac{3m_e}{m_n} N_e \nu_{en} k_B (T_e - T). \tag{19}$$

Here, m_e is the mass of an electron, N_e and T_e are the electron density and electron temperature, and the electron–atom collision frequency ν_{en} is expressed in terms of the momentum transfer cross section $\langle \sigma_{en}^d \rangle$ as

$$\nu_{en} = \frac{4}{3} N_n \left(\frac{8k_B T_e}{\pi m_e} \right)^{1/2} \langle \sigma_{en}^d \rangle. \tag{20}$$

Estimating the rate Q_e from values of the plasma parameters typical of the positive column of an argon glow discharge in the Hasegawa experiments [7], namely, $N_e = 10^9$–10^{10} cm^{-3}, $N_n \approx 10^{17}$ cm^{-3}, $T_e = 2$–3 eV, and $T \approx 0.035$ eV, we obtain $Q_e \approx 1.7 \times 10^2$–$2.5 \times 10^3$ W/m^3. According to Fig. 1, the threshold value is nearly $Q \approx 3 \times 10^5$ W/m^3; i.e., Q_e is two to three orders of magnitude lower than the threshold energy for the amplification of acoustic waves in a weakly ionized plasma. Therefore, the thermal energy transfer from electrons to neutral atoms in elastic collisions cannot serve as an energy source for acoustic instability in such a plasma and it is necessary to look for some other, more efficient mechanism for energy transfer from electrons to neutral atoms. We suggest that this mechanism may be attributed to inelastic collisions in which the electron energy is transferred to the translational degrees of freedom of neutral atoms. In a weakly ionized atomic gas-discharge plasma, there are three types of inelastic collisions in which a part of the thermal energy spent by the electron gas on the excitation and ionization of atoms is converted into the kinetic energy of atoms. The first energy-transfer mechanism is related to superelastic collisions between excited atoms or between excited atoms and atoms in the ground state. This mechanism is a two-step process involving successive electron–atom and atom–atom inelastic collisions:

$$A_p + e \longrightarrow A_m + e, \quad m = k, k_1, \ldots, \tag{21a}$$

$$A_k + A_{k_1} \longrightarrow A_{k'} + A_{k_1'}, \tag{21b}$$

where the subscripts p, m, k, … denote excited electronic states with energies E_p, E_m, E_k, … relative to the ground electronic state of a neutral atom. In this case, the energies of the electronic states should be such that $E_p < E_m$ and $E_k + E_{k_1} > E_{k'} + E_{k_1'}$. Note that the state p, either one of the two states k and k_1, and the states k' and k_1' can be the ground states.

The second energy-transfer mechanism is a two-step process related to three-body recombination reactions involving neutral atoms:

$$A_p + e \longrightarrow A^+ + e + e, \tag{22a}$$

$$A^+ + e + A \longrightarrow A_m + A, \tag{22b}$$

where the states p and m can also be the ground atomic states.

Finally, the third energy-transfer mechanism is a three-step process related to dissociative recombination reactions:

$$A_p + e \longrightarrow A^+ + e + e, \tag{23a}$$

$$A^+ + 2A \longrightarrow A_2^+ + A, \tag{23b}$$

$$A_2^+ + e \longrightarrow A_m + A. \tag{23c}$$

When the gas density is sufficiently high, mechanism (23) can make an appreciable contribution to the heat transfer from electrons to neutral atoms, because, in this case, the conversion of atomic ions into molecular ions in reaction (23b) is fairly efficient. In the case under study, namely, the acoustic wave amplification in the positive column of a conventional glow discharge, the gas density is low and, hence, mechanism (23) can be neglected. The calculation of the thermal energy transferred to neutral atoms by mechanisms (21) and (22) runs into serious difficulties because the effective

cross sections for numerous elementary events in collisional processes (21) and (22) are not known with certainty. Therefore, in order to estimate the amount of thermal energy transferred to neutral gas in inelastic processes (21b) and (22b), we will briefly analyze the electron energy balance in a weakly ionized atomic gas-discharge plasma.

The electron energy balance in a unit volume of a gas-discharge plasma with the current density J is described by the equation

$$\frac{d}{dt}\left(\frac{3}{2}N_e k_B T_e\right) = \frac{J^2}{\sigma} - \sum_i Q_i. \quad (24)$$

Here, $\sum_i Q_i$ is the total electron energy loss in elastic and inelastic collisions; J^2/σ is the rate of Joule heating of the electrons; and σ is the electrical conductivity of a weakly ionized plasma,

$$\sigma = \frac{N_e e^2}{m_e \nu_{en}}. \quad (25)$$

Taking into account the main electron energy loss in a steady state, we obtain from Eq. (24) the equation

$$\frac{J^2}{\sigma} = Q_e + Q_n + Q_R + Q_d. \quad (26)$$

Here, Q_e is given by Eqs. (19) and (20); Q_n is the thermal energy transferred to neutral gas in processes (21) and (22); the term Q_R describes the plasma energy losses due to emission in a set of atomic spectral lines and recombination continua, as well as bremsstrahlung caused by electron–ion collisions (in a weakly ionized plasma, the energy loss by bremsstrahlung is very small and does not play a role); and Q_d is the electron energy loss related to the ambipolar diffusion of charged particles toward the plasma boundary. Note that, since the gas temperature T is low and $T_e \gg T$, the atoms are excited and ionized primarily in collisions with electrons. In this case, the energy lost by the electrons is partially regained by them in the deexcitation processes and three-body recombination reactions, is partially converted into the energy of the neutral gas (Q_n), and is partially lost in the above radiative processes (Q_R). Consequently, we may assume that a low-temperature plasma emits energy at the expense of the electrons. That is why we have introduced the term Q_R into Eq. (26).

The rate of electron energy loss in a unit volume of plasma due to ambipolar diffusion and the subsequent recombination of electrons and ions on the tube wall was calculated by Gordiets *et al.* [16] under the assumption that each species of charged particles obey a Maxwellian velocity distribution. Using the results obtained in that paper and taking into account the condition $T_e \gg T_i$, we can represent Q_d as

$$Q_d \approx \frac{9(k_B T_e)^2 N_e}{m_i \nu_{in} R_0^2}\left(1 + \frac{1}{3}\ln\frac{T_e m_i}{T_i m_e}\right), \quad (27)$$

where m_i is the mass of an ion ($m_i = m_n$), T_i is the ion temperature, and ν_{in} is the ion–atom collision frequency. Further, we will assume that the temperatures of the heavy particles of different species are the same ($T_i = T$). The collision frequency ν_{in} can be estimated from a formula analogous to formula (20):

$$\nu_{in} = \frac{4}{3}N_n\left(\frac{8k_B T_i}{\pi m_{in}}\right)^{1/2}\langle\sigma_{in}^d\rangle, \quad (28)$$

where m_{in} is the reduced mass and $\langle\sigma_{in}^d\rangle$ is the momentum transfer cross section for elastic collisions of ions with neutral particles. Using Eq. (19) and representations (25) and (27), we can write

$$\Delta_e \equiv Q_e/\left(\frac{J^2}{\sigma}\right) \approx \frac{3N_e^2 e^2 k_B(T_e - T)}{m_n J^2}, \quad (29)$$

$$\Delta_d \equiv Q_d/\left(\frac{J^2}{\sigma}\right) \approx \frac{9(k_B T_e)^2 N_e^2 e^2}{m_e m_i \nu_{en}\nu_{in} R_0^2 J^2}\left(1 + \frac{1}{3}\ln\frac{T_e m_i}{T_i m_e}\right). \quad (30)$$

Let us now estimate the quantities Δ_e and Δ_d for the above parameters of the positive plasma column of a glow discharge in argon. We set $R_0 = 2$ cm and assume that the electrons and ions collide with neutral atoms as if they were all solid spheres. In this case, $\langle\sigma_{en}^d\rangle$ and $\langle\sigma_{in}^d\rangle$ coincide with the total collision cross sections and are equal to πd_{12}^2, where $d_{12} = (d_1 + d_2)/2$, with d_1 and d_2 being the diameters of the colliding particles [17]. We thus can assume that $\langle\sigma_{en}^d\rangle \approx 10^{-15}$ cm^2 and $\langle\sigma_{in}^d\rangle \approx 4 \times 10^{-15}$ cm^2. Then, we set the discharge current equal to $I = 0.1$ A ($J = I/\pi R_0^2$) and evaluate ν_{en} and ν_{in} from formulas (20) and (28), respectively. As a result, we obtain from Eqs. (29) and (30) $\Delta_e \approx 6 \times 10^{-5}$–$9 \times 10^{-3}$ and $\Delta_d \approx 3 \times 10^{-6}$–$6 \times 10^{-4}$. Hence, we have $\Delta_e \ll 1$ and $\Delta_d \ll 1$, which enables us to neglect the first and last terms on the right-hand side of Eq. (26). As for the radiative loss term Q_R, its calculation is a fairly difficult task. However, the results of the experimental studies of the dependence of the phase velocity of acoustic waves on the discharge current for the above plasma parameters [7] show that almost all of the power transferred from the electric field J^2/σ to electrons goes into the heating of the neutral gas. Therefore, the radiative loss term Q_R should also be small in comparison with J^2/σ. Accordingly, omitting the term Q_R in

Eq. (26) or setting $Q_R \sim Q_n$, we obtain $Q_n \sim J^2/\sigma$, which yields the following estimate for Q_n/Q_e:

$$\frac{Q_n}{Q_e} \sim \frac{1}{\Delta_e} \approx 1.1 \times 10^2 – 1.7 \times 10^4.$$

Hence, we have $Q_n/Q_e \gg 1$, which indicates that the thermal energy transfer from electrons to neutral gas in inelastic collisional processes (21) and (22) prevails over the energy transfer to neutral gas in elastic electron–atom collisions. We thus can conclude that the role of the energy source for acoustic instability is played by inelastic processes (21) and (22) rather than by elastic electron–atom collisions, as was previously thought. This conclusion is not surprising, because, according to [18], inelastic processes in, e.g., an argon plasma begin to compete with radiative and elastic processes at electron temperatures of $T_e > 1$ eV, which agrees well with the data obtained by Hasegawa [7], who observed that sound waves in a gas-discharge plasma were amplified at an electron temperature of about $T_e = 2$–3 eV.

It is noteworthy that the effect of the transfer of electron energy to neutral atoms on the acoustic wave propagation depends not only on the amount of the energy transferred but also on the time scale on which the transfer process occurs. In particular, for two-step process (21), the characteristic times of inelastic collisions (21a) and (21b) should be much shorter than the acoustic wave period. For this to hold, it is sufficient that the following condition be satisfied: $\omega/2\pi \ll \tau^{-1}$, where τ is the characteristic time of inelastic processes (21b). The reason is that these processes certainly occur on much longer time scales than inelastic collisions (21a) because the latter have large cross sections and because the mean electron thermal velocity is much higher than the velocities of the atoms.

Let us estimate the characteristic time scale of inelastic processes (21b). For simplicity, we only consider the deexcitation of the kth state of an excited atom in collisions with atoms in the ground state (transition $k \longrightarrow k'$ such that $E_{k'} < E_k$). In order of magnitude, we have $\tau^{-1} \sim \sigma_{kk'} \bar{v} N_0$, where $\sigma_{kk'}$ is the cross section for transition $k \longrightarrow k'$, $\bar{v}$ is the mean thermal velocity of an excited atom with respect to an atom in the ground state, and N_0 is the density of unexcited atoms. Assuming that the particles obey a Maxwellian distribution over v with the temperature $T = 0.035$ eV and that the reduced mass of the particles is $m_n/2$ (where m_n is the mass of an atom), we find that $\bar{v} \approx 7 \times 10^4$ cm/s for argon. Then, assuming that the characteristic cross section for the transition in question is $\sigma_{kk'} \sim 10^{-16}$ cm^2 [19] and setting $N_0 \approx N_n \approx 10^{17}$ cm^{-3}, we obtain the following estimate for τ^{-1}: $\tau^{-1} \sim 7 \times 10^5$ s^{-1}. We thus arrive at the condition $\omega/2\pi \ll 7 \times 10^5$ Hz, which holds for conventional sound waves regardless of their frequency.

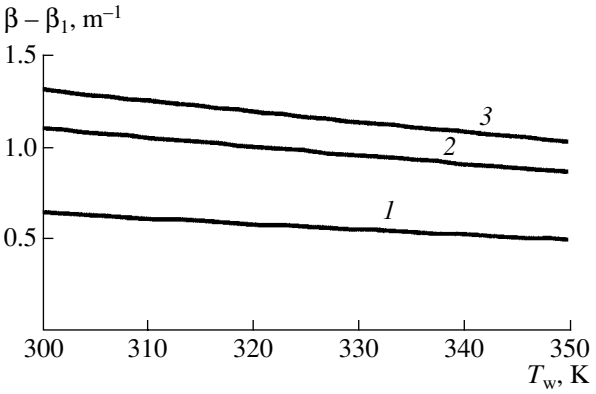

Fig. 8. Amplification factor $\beta - \beta_1$ vs. temperature T_w of the discharge tube wall for $\omega/2\pi = 500$ Hz and $\alpha =$ (*1*) 50, (*2*) 100, and (*3*) 150 W/(m^2 K). The remaining parameters are the same as in Fig. 1.

5. CONCLUSION

The main result of out theoretical study (within its range of applicability) is that the energy source for acoustic instability (sound amplification) in the positive plasma column of a glow discharge is the energy transfer from electrons to neutral gas in two-step (electron–atom and atom–atom) inelastic collisional processes (21) and (22). This result eliminates the difficulties associated with the fact that the energy transferred to the neutral gas in elastic electron–atom collisions is too low to provide acoustic wave amplification in a weakly ionized plasma. We have found that, even when the energy transferred to the neutral gas exceeds the threshold energy for acoustic wave amplification, the waves will not necessarily be amplified. The reason is a strong heating of the neutral gas, because conventional heat conduction cannot provide cooling of the gas required for the onset of instability. For this reason, we have suggested that steady-state acoustic streaming induced in the field of a sound wave gives rise to gas mixing in the radial direction, thereby cooling the gas. We have shown that this cooling mechanism should be five to seven times more efficient than cooling of the gas by conventional heat conduction. We have also shown that the propagation of low-frequency (up to 1.0–1.5 kHz) sound waves through a weakly ionized plasma should be dispersive. This phenomenon, as well as acoustic wave amplification, results from the effect of the electron gas on the wave propagation in a weakly ionized plasma.

In conclusion, we emphasize that heat conduction equation (9) was solved under the assumption that the temperature of the tube wall is equal to the temperature of the surrounding medium. However, experimental investigations are usually carried out under conditions of free heat exchange between the tube and the surrounding medium. Consequently, a more rigorous analysis requires the use of free boundary conditions to

solve the heat conduction equation and thereby determine the wall temperature. Our preliminary calculations show that the wall temperature can be higher than the temperature of the surrounding medium by no more than 50°. However, it is seen from Fig. 8 that, with such a change in the wall temperature, the amplification factor changes only slightly; hence, the results obtained will remain qualitatively the same.

Based on the results of [20], we have also estimated the radial acoustic streaming velocity for the above conditions in the positive plasma column of a glow discharge in argon. Because of the low frequencies of acoustic waves, a comparatively large kinematic viscosity of the gas, and the small radius of the discharge tube, this velocity turned out to be high enough for the acoustic thermal conductivity (which is proportional to the acoustic streaming velocity) to be about one order of magnitude higher than the conventional thermal conductivity of the gas. A more detailed analysis of the propagation of acoustic waves in a weakly ionized gas-discharge plasma on the basis of the heat conduction equation with allowance for free boundary conditions and with the explicit introduction of the radial acoustic streaming velocity will be given in a separate paper.

REFERENCES

1. U. Ingard, Phys. Rev. **145**, 41 (1966).
2. U. Ingard and M. Schulz, Phys. Rev. **158**, 106 (1967).
3. L. D. Tsendin, Zh. Tekh. Fiz. **35**, 1972 (1965) [Sov. Phys. Tech. Phys. **10**, 1514 (1966)].
4. M. Schulz and U. Ingard, Phys. Fluids **12**, 1237 (1969).
5. L. Aubrecht, Phys. Lett. A **27A**, 526 (1968).
6. M. Fitaire and T. D. Mantei, Phys. Fluids **15**, 464 (1972).
7. M. Hasegawa, J. Phys. Soc. Jpn. **37**, 193 (1974).
8. A. F. Pal' and A. S. Serev, *2nd All-Union Seminar on the Interaction of Acoustic Waves with Plasma, Erevan, 1991,* Abstracts of Papers, p. 6.
9. I. P. Zavershinskiĭ, E. Ya. Kogan, and N. E. Molevich, Akust. Zh. **38**, 702 (1992) [Sov. Phys. Acoust. **38**, 387 (1992)].
10. N. L. Aleksandrov, A. P. Napartovich, and A. F. Pal', Fiz. Plazmy **16**, 862 (1990) [Sov. J. Plasma Phys. **16**, 502 (1990)].
11. A. R. Mkrtchyan and O. S. Torosyan, Akust. Zh. **45**, 633 (1999) [Acoust. Phys. **45**, 562 (1999)].
12. A. R. Mkrtchyan and O. S. Torosyan, in *Proceedings of the XIII International Conference on Gas Discharges and Their Applications, Glasgow, 2000*, Vol. 2, p. 969.
13. G. A. Galechyan, Usp. Fiz. Nauk **165**, 1357 (1995) [Phys. Usp. **38**, 1309 (1995)].
14. Y. Ishida and T. Idehara, J. Phys. Soc. Jpn. **35**, 1747 (1973).
15. S. J. Bauer, *Physics of Planetary Ionospheres* (Springer-Verlag, Heidelberg, 1973; Mir, Moscow, 1976).
16. B. F. Gordiets, L. I. Gudzenko, and L. A. Shelepin, Zh. Tekh. Fiz. **36**, 1622 (1966) [Sov. Phys. Tech. Phys. **11**, 1208 (1967)].
17. G. A. Bird, *Molecular Gas Dynamics* (Clarendon, Oxford, 1976; Mir, Moscow, 1981).
18. L. M. Biberman, V. S. Vorob'ev, and I. T. Yakubov, *Kinetics of Nonequilibrium Low-Temperature Plasmas* (Nauka, Moscow, 1982; Consultants Bureau, New York, 1987).
19. L. I. Gudzenko and S. I. Yakovlenko, *Plasma Lasers* (Atomizdat, Moscow, 1978).
20. Q. Qi, R. E. Johnson, and J. G. Harris, J. Acoust. Soc. Am. **97**, 1499 (1995).

Translated by O.E. Khadin